Dissertation
submitted to the
Combined Faculties for the Natural Sciences and for Mathematics
of the Ruperto-Carola University of Heidelberg, Germany
for the degree of
Doctor of Natural Sciences

Put forward by
Diplom-Physiker Georg Altenstein
Born in Cologne, Germany
Oral examination: 2014/10/29

A Novel Collimator Concept for Fast Rotational IMRT

Referees: Prof. Dr. Uwe Oelfke
Prof. Dr. Wolfgang Schlegel

Abstract

The 2D binary multileaf collimator (2D-bMLC) is a novel collimator concept specially dedicated to fast rotational radiotherapy treatments. The 2D-bMLC consists of individually controlled absorber channels arranged side by side to form a 2D aperture. The design, which leads to radiation fields characterized by a striped pattern, aims at very quick aperture modulations. Using a Monte Carlo (MC) method we established the dosimetric model of a theoretical flattening filter free medical linac equipped with a 2D-bMLC. We further developed a treatment planning system for rotational 2D-bMLC treatments with a new optimization method and a MC framework for exact calculation of the dose. In plan comparison studies, 2D-bMLC plans were calculated for various clinical indications and compared to clinically accepted IMRT and Helical Tomotherapy plans. The design of the 2D-bMLC might be especially sensitive to geometrical misalignments of the collimator on the one hand, and to intrafraction motion on the other hand. Both aspects have been investigated in additional MC studies. The results of the planning studies showed that the 2D-bMLC concept is in principal adequate for rotational radiotherapy treatments with potential delivery times considerably below those of IMRT techniques applied in the clinics today. Clinically acceptable 2D-bMLC plans with delivery times below 30 seconds were calculated for all investigated tumour sites. Dosimetric parameters were comparable to those of the reference plans. Already very small geometrical misalignment of the 2D-bMLC can cause severe under-dosage, and especially high demands on manufacture tolerances as well as on quality assurance will be necessary, if a 2D-bMLC should be produced for clinical use. Consideration of intrafraction motion, however, did not lead to significant changes in the accumulated doses calculated for prostate plans with standard fractionation.

Zusammenfassung

Ein neuartiges Kollimatorkonzept für die Strahlentherapie mit hochenergetischen Photonen wurde im Rahmen dieser Arbeit ausgearbeitet. Das Konzept des *2D binary multileaf collimator* (2D-bMLC) soll 2-dimensionale Anpassungen des Bestrahlungsfeldes in sehr kurzer Zeit erlauben und wurde speziell für schnelle intensitätsmodulierte Rotationstherapie entworfen. Der 2D-bMLC besteht aus Absorberkanälen, die nebeneinander in einer 2D-Matrix angeordnet sind. Jeder Kanal wird einzeln angesteuert, um geöffnet oder geschlossen zu werden. Mit der Monte-Carlo-Methode (MC) wurde erfolgreich das dosimetrische Modell eines theoretischen Bestrahlungsgerätes etabliert. Zudem wurde ein Bestrahlungsplanungssystem entwickelt, das sich aus einem Tool für die inverse Optimierung von Behandlungsplänen und einem MC-Tool für exakte zeitaufgelöste Dosisberechnung zusammensetzt. In Planungsstudien wurden 2D-bMLC-Pläne für verschiedene klinische Indikationen berechnet und mit klinisch akzeptierten IMRT- und Tomotherapy-Plänen verglichen. Zusätzliche MC-Studien wurden durchgeführt, um den Einfluss von geometrischen Toleranzen bei Herstellung und Installation des Kollimators und von Bewegungen des Patienten während der Bestrahlung (intrafraktionellen Bewegungen) abzuschätzen. In den Planungsstudien konnten für alle behandelten Fälle klinisch akzeptable 2D-bMLC-Pläne mit Behandlungszeiten unter 30 Sekunden berechnet werden. Im visuellen Vergleich und in Bezug auf die ausgewerteten dosimetrischen Parameter waren die Dosisverteilungen vergleichbar mit denen der Referenzpläne. Bereits relativ kleine geometrische Ungenauigkeiten bei der Aufhängung des Kollimators können schwerwiegende Unterdosierungen verursachen. Bei einer technischen Realisierung des Konzeptes müssten deshalb besonders hohe Anforderungen an Herstellung, Installation und Qualitätssicherung des Bestrahlungsgerätes gestellt werden. Berücksichtigung von intrafraktionellen Bewegungen bei Prostatabestrahlungen führte hingegen bei konventioneller Fraktionierung nicht zu signifikanten Veränderungen der geplanten Dosisverteilungen.

Contents

Outline

In this thesis, we present a novel collimator concept which is specially dedicated to fast rotational radiotherapy treatments and to which we have given the name: *2D binary multileaf collimator* or *2D-bMLC* in short. The goal of the presented work was to explore the potential capabilities of the concept in modelling the physics of the dose delivery and in applying this for patient planning studies.

In chapter 1 we give a short introduction to the basics of radiation oncology and to modern radiotherapy techniques. In chapter 2 the 2D-bMLC concept is presented in depth, as well as its dosimetric model that was established with a Monte Carlo method. The newly developed treatment planning framework for fast rotational 2D-bMLC treatments is described in chapter 3, together with a first plan comparison study. Additional planning studies, that were performed to investigate the influence of certain treatment parameters on the final dose distributions, are grouped together in chapter 4. The design of the 2D-bMLC might be especially sensitive to geometrical misalignments of the collimator on the one hand, and to patient motion occurring during treatment delivery (intrafraction motion) on the other hand. Both aspects have been investigated in the Monte Carlo studies presented in chapter 5.

Parts of this work have been published - in accordance with the regulations of the Combined Faculties for the Natural Sciences and for Mathematics at the University of Heidelberg - in a peer-reviewed journal article (Altenstein et al., 2012b) and have been presented on international conferences (Altenstein et al., 2012a,c, 2013a,b, 2014).

Chapter 1

General Introduction

1.1 Basics of Radiotherapy

1.1.1 The aim of radiotherapy

Radiotherapy is one of the most common treatments for cancer. It uses ionizing radiation to kill the cancer cells. This can be achieved, if the DNA of the cancer cell is damaged by ionizations. On the one hand, the primary radiation particles or rather their secondary electrons can ionise the DNA molecule directly. On the other hand, ionisation and scattering events at water molecules lead to the production of free radicals, which diffuse within the cell and may undergo chemical reactions with the DNA molecule. Finally, a variety of types of damage in DNA can be produced. If the mechanisms of DNA repair fail, the damages may be lethal to a cell. Of course, ionizing radiation can kill both malignant and healthy cells.

In radiation physics the term dose, or absorbed dose is defined as the energy absorbed per unit mass of medium ($D = \frac{dE}{dM}$). Its SI unit is gray (Gy), which is defined as 1 Joule of energy per kilogram of medium. The aim of radiotherapy is to deliver a dose to the tumour, which is high enough to kill all the tumour cells (or as much as possible in the case of a palliative radiotherapy), and to spare the surrounding healthy tissue as much as possible from dose. Technically this can be a very difficult task, even if we ignore outstanding biological issues and if we assume that we know where the cancer cells are located and which dose has to be applied. In the history of radiotherapy again and again, technological efforts have been made to better conform the doses to the tumour.

1.1.2 A clinical treatment plan

A typical clinical treatment plan for a radiotherapy comprises, besides the diagnosis and the aim of the treatment, the definition of one or several target volumes as well as the dose prescription and the fractionation scheme. Target volume definitions are covered in the next section. The fractionation scheme specifies the number of fractions in which the treatment is subdivided, the fraction size and the time schedule for delivery of the fractions. Primarily, the total dose is fractionated for biological reasons. Fractionation allows the irradiated tissue time to recover. Typically, the cell repair mechanisms work better in healthy than in malignant cells, and thus, the tissue recovery is much more efficient. In simple terms, fractionation can introduce a differential biological effect of the treatment for the tumour and for the surrounding normal tissue.

Typically, the limiting factor of a treatment is the toxicity induced in the organs at risk (OARs).

Dose constraints for the OARs have to be respected in order to avoid or limit the risk of critical radiation induced damage. Dose constraints can be introduced in the treatment plan as maximum constraints (such as: “At any point the spinal cord should not receive a dose superior to X Gy”) or more general dose-volume constraints (such as: “Not more than 20% of the lung should receive doses above X Gy”).

1.1.3 Target volume definitions

Generally, in clinical practice the following volume concepts, recommended by the *International commission on Radiation Units and Measurements* (ICRU) for treatment planning in external beam radiotherapy, are used today. We quote the definitions from ICRU Report 83 (ICRU, 2010):

- The **Gross Tumour Volume** (GTV) is the gross demonstrable extent and location of the tumour. The GTV may consist of a primary tumour, metastatic regional node(s), or distant metastasis.
- The **Clinical Target Volume** (CTV) is a volume of tissue that contains a demonstrable GTV and/or sub-clinical malignant disease with a certain probability of occurrence considered relevant for therapy. [..] The notion of sub-clinical malignant disease includes the microscopic tumour spread at the boundary of the primary-tumour GTV [..], the possible regional infiltration into lymph nodes, and the potential metastatic involvement of other organs (e.g., brain), despite their normal appearance on clinical and radiological examinations.
- The **Planning Target Volume** (PTV) is a geometrical concept introduced for treatment planning and evaluation. It is the recommended tool to shape absorbed-dose distributions to ensure that the prescribed absorbed dose will actually be delivered to all parts of the CTV with a clinically acceptable probability, despite geometrical uncertainties such as organ motion and setup variations. It is also used for absorbed-dose prescription and reporting. It includes the CTV and margins which are added around the ladder to compensate for the effects of organ and patient movements and inaccuracies in beam and patient set up.

Furthermore, depending on the clinical situation, it might be useful to determine separately an internal and an external margin. The internal margin accounts for organ motion or more precisely for uncertainties in size, shape, and position of the CTV within the patient. The external margin accounts for possible variations in patient and beam position. Both margins should be added quadratically to result in the final CTV-to-PTV margin. More details about volume and margin definitions can be found in the ICRU Reports 50, 62 and 83. (ICRU, 1993, 1999, 2010).

1.2 External Beam Radiotherapy with X-Rays

Both high-energetic photons and accelerated charged particles, such as electrons, protons and ions, are used in the treatment of cancer. Since several decades, the most commonly applied form of radiotherapy is external beam radiotherapy with mega-voltage X-rays. The treatments are performed with so called medical linear accelerators (linacs).

1.2.1 Medical Linacs

In medical linacs, electrons are accelerated to kinetic energies from 4 to 25 MeV. The accelerated electrons are guided to the treatment head and directed onto a target to produce bremsstrahlung X-rays. Compared to the linacs used for high-energy physics research, medical linacs are compact machines. Typically they are mounted isocentrically, which means that the treatment head can move around in order to aim the radiation beam toward the patient from various directions. In figure 1.1, we show a common design configuration for an isocentrically mounted medical linac.

A special case of a medical linac is the tomotherapy unit, the design of which is shown in figure 1.2. The linac is installed in a ring-like gantry, similar to that of a CT scanner. During a tomotherapy treatment, fan-beams are delivered to the patient meanwhile the gantry rotates. The gantry rotation is synchronised with a longitudinal translation of the couch, which ensures that the patient is transported trough the gantry bore. The result is a helical dose delivery. (Jeraj et al., 2004; Mackie et al., 1999; Welsh et al., 2002)

Here, we are not going into the technical details of medical linacs. More information can be found in textbooks such as (Podgorsak, 2010) or (Metcalfe et al., 2007). These books also cover the physical basics of radiotherapy including the interaction properties of photons and electrons.

1.2.2 Flattening filter free beams

In the MeV energy range the bremsstrahlung distribution from photon is strongly forward peaked. To compensate for this effect conventional medical linacs were to date equipped with a flattening filter (FF). The FFs are placed in the treatment head downstream the target to produce flat dose profiles. Flat dose profiles substantially facilitated dose calculation and treatment planning when computers where not yet used for these purposes.

A FF is usually made of medium or high Z material. It has a conical shape with a thickness of several centimetres at its center (Izewska, 1993). Consequently, the FF affects the dose rate of the medical linac. Furthermore, FF scatter photons are one of the major sources of treatment head scatter. If non-uniformity of the photon fluence is not required, the removal of the FF can therefore be advantageous by means of reducing head scatter and by allowing higher dose rates. Modern intensity modulated treatment techniques (see section 1.3.2) in principle do not require flattened beams. These techniques have stimulated the increasing interest in unflattened beams, and today several treatment units are already on the market, which can be operated clinically in a flattening filter free (FFF) mode. (Cashmore, 2008; Dzierma et al., 2012; Georg et al., 2011; Kragl et al., 2009; Pönisch et al., 2006; Vassiliev et al., 2006)

In figure 1.3, we show lateral fluence profiles measured for the FF and the FFF mode of a modern medical linac.

1.2.3 Multileaf collimator

In the history of radiotherapy, several collimation systems have been proposed for shaping the radiation fields of medical linacs. Today the by far most widely used device is the multileaf collimator (MLC) that was first commercially introduced in the late 1980s. Since then, the MLC techniques have been refined and developed further, but essentially the principle is the same. An MLC consists of two opposing banks of thin leafs of a high atomic numbered material, usually tungsten. Each leaf is controlled by a motor and can be moved independently in and out

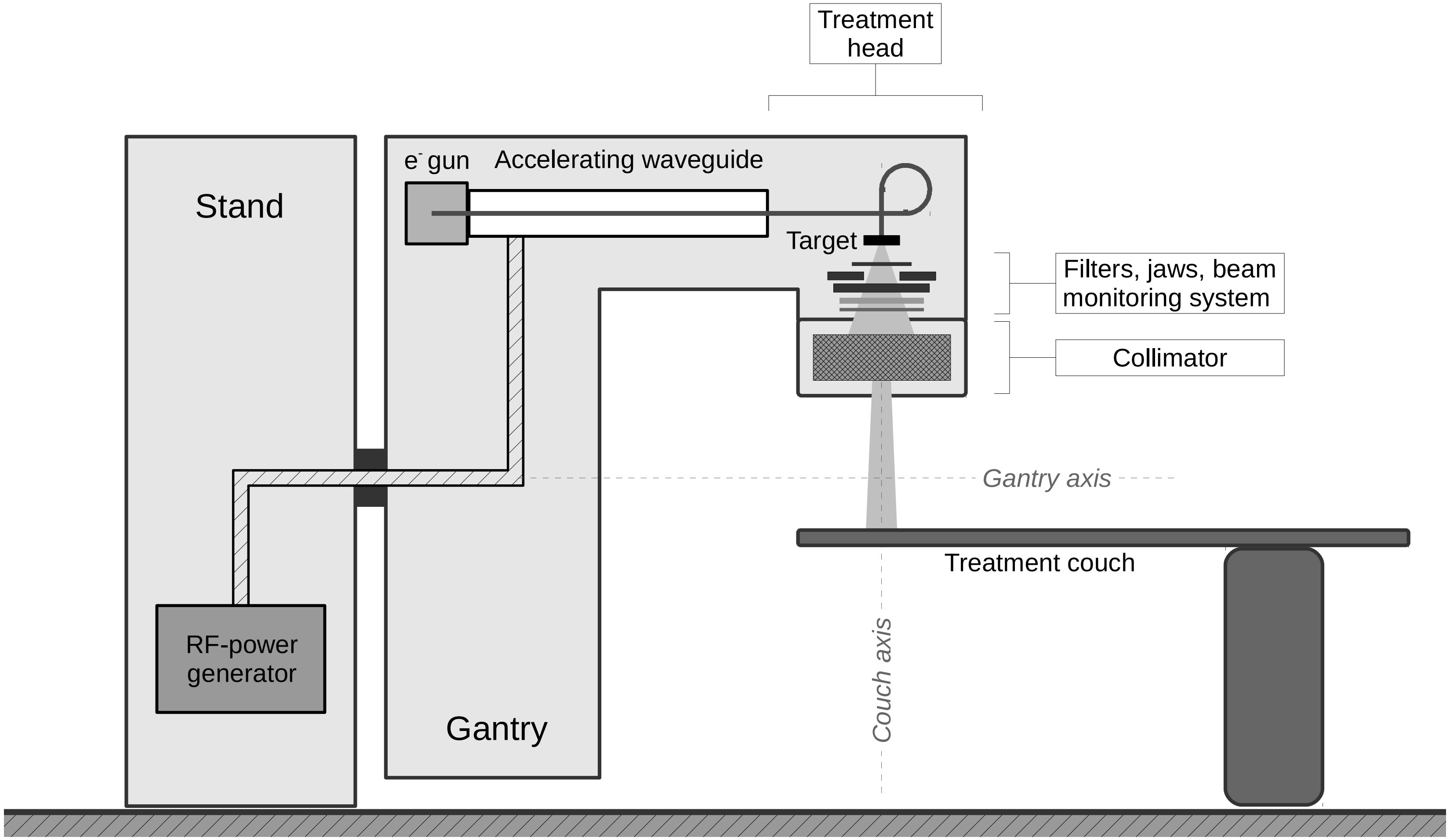

Figure 1.1: Possible design configuration for an isocentric medical linac based on (Podgorsak, 2010). For a treatment, the patient is first positioned and immobilised on the treatment couch. Then, the treatment couch is moved so that the target (the tumour) is at its planned position, typically at the isocenter of the linac. The isocenter coincides with the intersection point of the gantry axis and the couch axis. The gantry can be rotated around the gantry axis in order to aim the radiation beam toward the patient from different directions (see also figure 1.6). A medical linac can also be used for electron therapy, if the target is removed and an electron beam collimation system is installed.

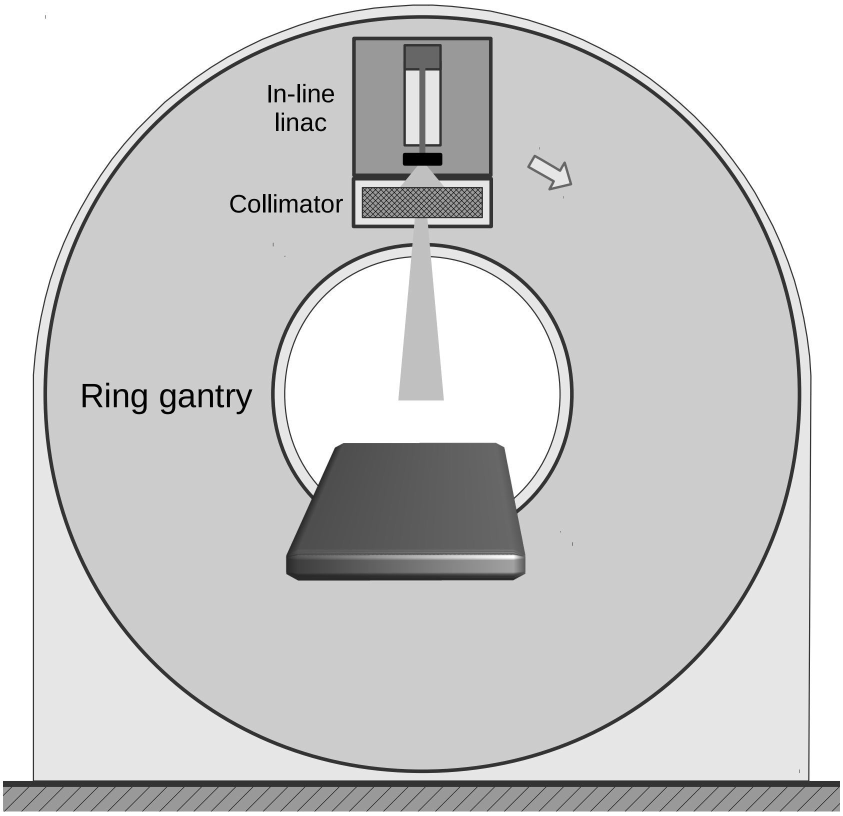

Figure 1.2: The tomotherapy unit is a special case of a medical linac which delivers radiation to the patient in a helical way. This is obtained by concurrent gantry rotation and couch/patient travel. The radiation field is fan-shaped with a variable lateral width (slice thickness) of up to 5 cm. A very fast pneumatically driven collimator with leafs arranged in a row is used to modulate the fan beam.

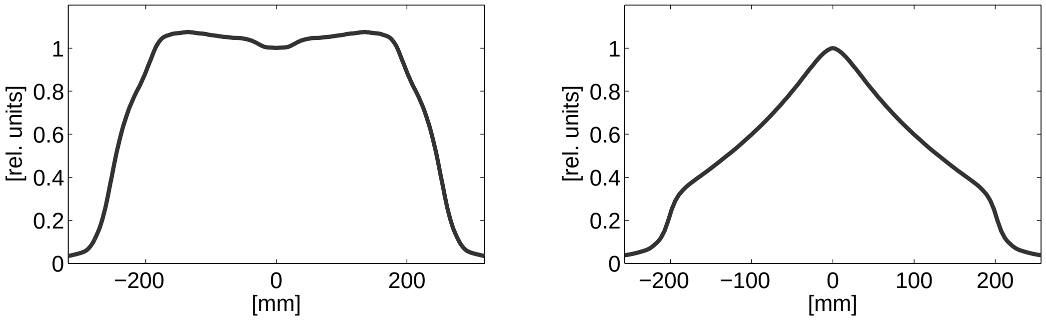

(a) Flattening filter mode (FF)

(b) Flattening filter free mode (FFF)

Figure 1.3: Relative lateral profiles of the primary energy fluence measured for the Siemens ARTISTE 160 MLC$^{\text{TM}}$ with flattening filter and with the flattening filter removed. The acceleration voltage was 6MV in both cases. The profiles were measured in the isocentric plane of the treatment machine and were normalized to the central axis respectively. The dose rate is up to almost nine times higher in FFF mode than in FF mode.

of the path of the radiation field. Originally proposed to replace casting blocks as beam shaping devices, the computerised MLC can generate arbitrary field shapes very efficiently. However, as shown in figure 1.4(a) the finite width of the leafs yields a stair-stepping effect in the field shapes.

In general, in the treatment head of a medical linac the radiation field is pre-collimated by primary jaw pairs before the MLC defines the final aperture. MLCs are characterised by mechanical and geometrical parameters such as the maximum field size and the leaf resolution. Common values for the leaf resolution are 2-10 mm. The total number of leafs is often above 100. For a more detailed description we refer to the literature, e.g. to (Webb, 1997).

1.3 Delivery Techniques

1.3.1 Conformal radiation therapy

In the following we will shortly introduce conformal radiation therapy (CRT) and intensity modulated radiation therapy (IMRT). As illustrated in figure 1.4, the idea of CRT is to conform the radiation field to the planning target (PTV) volume and to block out critical organs at risk (OAR) at the same time. In order to optimize the dose coverage of the PTV and minimize the dose to the OARs treatment fields can be applied from different directions.

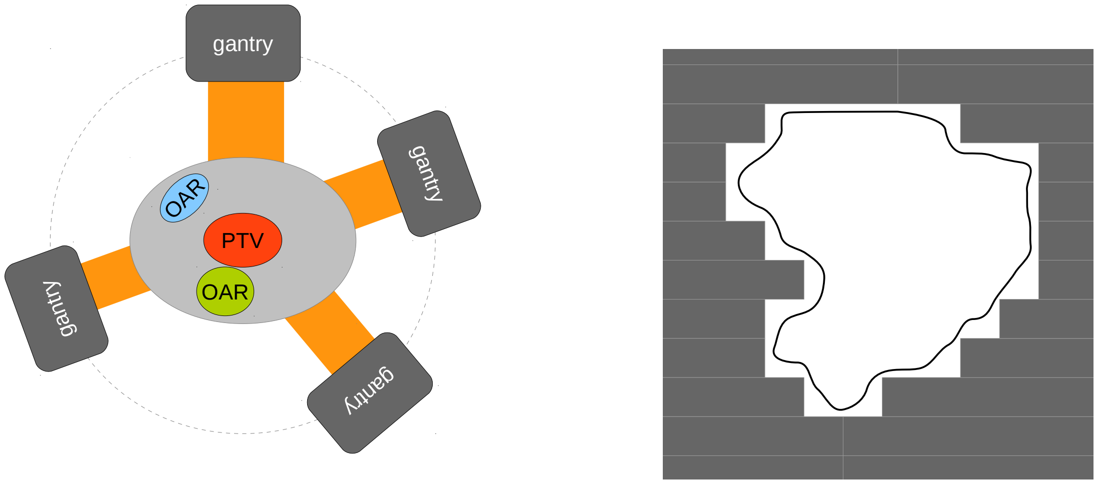

(a) Radiation fields are delivered subsequently from different gantry angles.

(b) Hypothetical MLC aperture (beams eye view). The MLC shape is adapted to the PTV outline.

Figure 1.4: Conformal radiation therapy (CRT). The idea is to conform the radiation fields to the PTV and to block out critical structures. Several beams can be delivered with varying treatment parameters such as the gantry angle and the MLC shape.

In the sketch in figure 1.4(a) fields are applied from different gantry angles. The fields would be delivered subsequently. Radiation is switched off meanwhile the gantry is moved from one treatment position to the next and meanwhile the MLC is adapted. In principal, not only the gantry rotation but all geometrical degrees of freedom of a medical linac can be exploited (see figure 1.1). Furthermore, wedge filters can be used in order to produce a gradient of intensity within a field. Some linacs also provide several acceleration voltages. All treatment parameters are set out in the physical treatment plan, generally established with aid of computer programs.

1.3.2 Intensity modulated radiation therapy

If we disregard the intensity differences of the X-ray beam produced in the treatment head of a linac, one individual collimator aperture produces a binary intensity distribution. The MLC aperture shown in figure 1.4(b) would e.g. produce the intensity map illustrated in figure 1.5(a). As the name suggests, the idea of intensity modulated radiation therapy (IMRT) is to modulate the fluence of the incoming beams. The added flexibility can be utilized to better conform the resulting dose distribution to the target volume. The modulation is thereby not limited to the one-dimensional gradients produced by wedges that were mentioned above. In principal, any deliverable two-dimensional modulation might be allowed. In figure 1.5(b), we show a potential intensity map that could be realised with a MLC. To achieve this kind of modulation, several beams from the same direction but with different MLC apertures are superimposed, that means applied one after another. (Bortfeld, 2006)

1.3.3 Inverse planning

IMRT as it is practised today became possible with the concept of inverse planning that was first introduced by Brahme (1988). The following quote from Brahmes paper summarises the goal of inverse planning and the conceptual difference to conventional forward planning:

> Current treatment planning procedures generally employ a trial and error type of approach in testing various beam combinations in order to find the best irradiation technique for a given target volume. In this investigation the reverse approach has been taken, that is: Given the desired dose distribution [...], how should the incident beams best be shaped in order to generate this distribution? (Brahme, 1988)

Generally, the problem is solved with computers with planning software specially dedicated to IMRT planning. A typical inverse planning procedure performed with a treatment planning system (TPS) for IMRT is outlined briefly in the following. The TPS requires the user to pre-define certain treatment parameters, such as e.g. the linac energy or the beam directions (which parameters have to be set finally depends on the TPS and the delivery technique). For each beam direction, the TPS assesses automatically a MLC aperture which encloses the complete target volume, such as the aperture shown in figure 1.4(b). The resulting apertures are subdivided into beam elements or ‘bixels’. The weights of the bixels are the free variables which have to be determined in an inverse optimization.

Typically, the optimization algorithms used for this purpose rely on a pre-calculated so called ‘dose influence matrix’. The elements of the dose influence matrix are the dose contributions from each bixel to each volume element (voxel) of the patient geometry. The dose calculation engine of the TPS is used to assessed the dose influence matrix. Finally, before the optimization of the bixel weights can be performed, the optimization goals have to be specified by the user. A common approach is to define a number of constraints, expressed as lower and upper dose limits for the target volume and relevant organs. Additionally, the user specifies priority values associated to each constraint.

The result of the optimization is a fluence map (or fluence weight map) for each beam direction. The maps could e.g. be similar to the one shown in figure 1.5(b). Once the optimization is completed, the fluence maps have to be translated into sets of deliverable MLC fields. This non-trivial terminal step of the planning procedure, referred to as the sequencing step, is also handled by the TPS. The superposition of the proposed field segments should be as close as

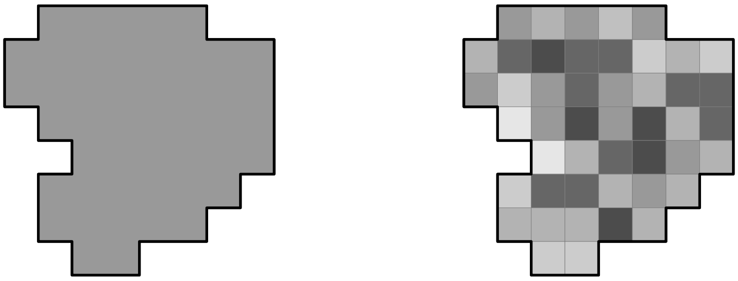

(a) Binary intensity map (b) Modulated intensity map

Figure 1.5: (a) In 3D conformal radiation therapy (CRT), field shaping is used alone and the field intensities across the shape are constant. The corresponding MLC aperture is shown in figure 1.4(b). (b) In intensity modulated radiation therapy (IMRT) the intensities across the field shape are modulated.

possible to the optimal fluence maps. However, generally the number of final segments is limited by the TPS or its user in order to assure reasonable delivery times and to respect the practical limits and tolerances of the treatment machines. Therefore, the sequencing can lead to degradations in plan quality compared to the plan associated to the actual optimization result.

Of course, the methods for treatment planning were described here very briefly. Also we did not introduce other planning strategies such as e.g. direct aperture optimization (Shepard et al., 2002). More details about treatment planning and the different algorithms can be found in the literature, e.g. in (Webb, 2003, 2005). The inverse planning method developed as part of this thesis is described in detail in chapter 3.

1.3.4 Rotational IMRT

In ‘conventional’ IMRT, as it is practised in the clinics since the late 1990s, the gantry stops at fixed angles before beams are applied. At each stop several MLC segments are delivered as discussed before. This delivery techniques is also referred to as fixed-field IMRT (figure 1.6(a)). In newer techniques, that can be summarised under the term of rotational IMRT or Volumetric Modulated Arc Therapy (VMAT), the gantry is rotating and MLC-shaped beams are delivered at the same time (figure 1.6(b)). Intensity modulation is achieved by varying beam shape, dose rate and/or gantry speed meanwhile the gantry rotates. A treatment can be performed in one or several gantry rotations.

Several VMAT techniques that can be performed with a MLC equipped medical linac have been proposed (Otto, 2008a; Ulrich et al., 2007a; Wang et al., 2008; Yu, 1995). Large-scale clinical implementations did start in 2008, when the two linac vendors Varian and Elekta introduced their solutions, which are marketed under the names RapidArc$^{\text{TM}}$ (Varian) and VMAT$^{\text{TM}}$ (Elekta). A historical introduction and a current overview over VMAT techniques can be found in Yu and Tang (2011).

In section 1.2, the tomotherapy unit was shortly presented as a special case of a medical linac. Actually, helical tomotherapy is also a rotational IMRT techniques. Helical tomotherapy is applied in the clinics since 2003 and is often stated as the current ’Gold Standard’ in IMRT delivery concerning target dose conformity. Of course the technique is conceptually very different to the VMAT techniques (see also section 1.2 and figure 1.2).

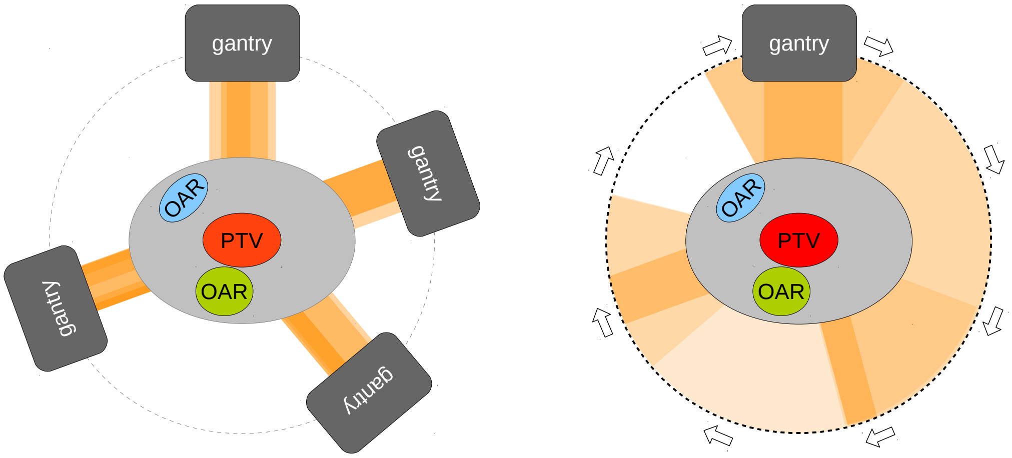

(a) Fixed-gantry IMRT

(b) Rotational IMRT

Figure 1.6: In fixed-field IMRT, the gantry stops at fixed angles before beams are applied. In contrast, in rotational IMRT beams are delivered meanwhile the gantry rotates.

Chapter 2

The 2D-bMLC Concept and Its Dosimetric Characterisation Using Monte Carlo Simulations

2.1 Overview

In this chapter, we present the novel technical concept of a 2D binary multileaf collimator (2D-bMLC). The 2D-bMLC consists of individually controlled absorber channels, which are arranged side by side forming a 2D collimator aperture. The design should allow for very quick aperture changes and is specially designed for fast dose delivery in rotational IMRT. The 2D-bMLC concept is introduced in section 2.3.1, and more technical details as well as possible design variations are given in appendix 2.B.

To determine the dosimetric properties of the 2D-bMLC, we designed a Monte Carlo model of a treatment machine equipped with an exemplary 2D-bMLC consisting of 30 by 30 channels (section 2.3.3). A virtual source model of a flattening filter free 7MV linac was used was used to characterise the linac phase space (appendix 2.A). The dosimetric evaluation included the primary radiation efficiency and the leakage dose of the collimator as well as the characterisation of individual channel beams. Possible tongue-and-groove effects of abutting channel beams were also investigated. The results are presented in section 2.4.

The successfully established dosimetric model of the 2D-bMLC was the basis for the development of a planning framework for rotational 2D-bMLC therapy, which we present in chapter 3.

Publication

Sections 2.2 to 2.6 have been published in Altenstein et al. (2012b). Results from this chapter have been presented at the international *ESTRO 31 Conference* in Barcelona, Spain, May 2012 (Altenstein et al., 2012a).

2.2 Introduction

Intensity-modulated radiation therapy (IMRT) is a widely accepted treatment technique, and its adoption into clinical practise has advanced far in the last decade. Most photon IMRT treatments are realised with standard medical accelerators (linac) equipped with a multileaf collimator (MLC). In general, a large number of independent MLC-shaped 2D-beams is delivered in succession. In conventional IMRT, the gantry stops at fixed angles before beams are applied (Bortfeld, 2006). Whereas in newer techniques, summarised under the term rotational IMRT or Volumetric Modulated Arc Therapy (VMAT), the gantry is rotating and cone beams are delivered at the same time. In doing so, intensity modulation is achieved by varying beam shape, dose rate and/or gantry speed during one or more rotations. (Otto, 2008a; Ulrich et al., 2007a; Wang et al., 2008; Yu, 1995)

Even if the conventional field-shaping MLC was originally not designed for IMRT (Webb, 2001), its advantages for both static beam and rotational IMRT are obvious. MLCs make use of two opposing banks of attenuating leafs, which can be positioned independently to realise a desired field opening. The concept allows a large variety of field shapes and, with motor driven leafs, it gives the ability to change the aperture automatically (Bortfeld, 2006). However, the time required for these aperture changes depends on the leaf speed, and, despite many technical advances in the past, the maximum leaf speed of modern MLCs is still limited. In IMRT treatments, where several fields of different shape has to be applied in order to achieve the intensity modulation, this mechanical restriction can also affect the overall delivery time of a treatment. Typical delivery times for IMRT fractions are today in the range of several minutes.

In this chapter we present a novel IMRT collimator concept, which aims at ultra-fast aperture modulation: A two-dimensional binary multileaf collimator (2D-bMLC). The concept is based on the principles published in (Heid, 2010). Absorber channels, arranged side by side in a tessellated pattern, form a 2D matrix collimator. The design allows individual independent control of each channel. An open channel results in a divergent quasi-rectangular beam. Whereas in one direction beams of adjacent channels abut, in the other direction they are separated because half of each channel always blocks the radiation. The 2D-bMLC does not shape open fields, like conventional MLCs do, but each element of its chequerboard like aperture can either be closed or half open. Therefore, the design allows in principal very quick aperture changes, and a possible application of the 2D-bMLC could be the dose delivery via fast rotational IMRT.

To evaluate the concept, we designed a Monte Carlo (MC) model of an exemplary 2D-bMLC with 30 by 30 channels. Each channel beam had a cross-section of approximately 5 mm by 10 mm in the isocentric plane. The research question, we wanted to answer in the study presented in this chapter, is whether the 2D-bMLC model fulfils in general the dosimetric requirements for the use in radiotherapy treatments. The dosimetric characterisation of the model, assessed in MC simulations with Geant4, includes the study of width and penumbra of the channel beams, the leakage and the dose delivery efficiency of the collimator as well as tongue-and-groove effects.

2.3 Methods

2.3.1 2D-bMLC design and mode of operation

The developed 2D-bMLC model consists of 30 by 30 absorber channels, which are arranged side by side on a spherical shell segment. In general, the collimator concept may consist of M by N channels, whereas the numbers M and N are only restricted by geometrical limits: For practical reasons, which will be outlined later, the covered segment of the spherical shell cannot be extended arbitrarily. The presented model is designed for a treatment machine with a source-to-axis distance (SAD) of 800 mm. The coordinate system used for all descriptions of the 2D-bMLC is shown in figure 2.5(b). It corresponds to the GANTRY system defined in (IEC 61217).

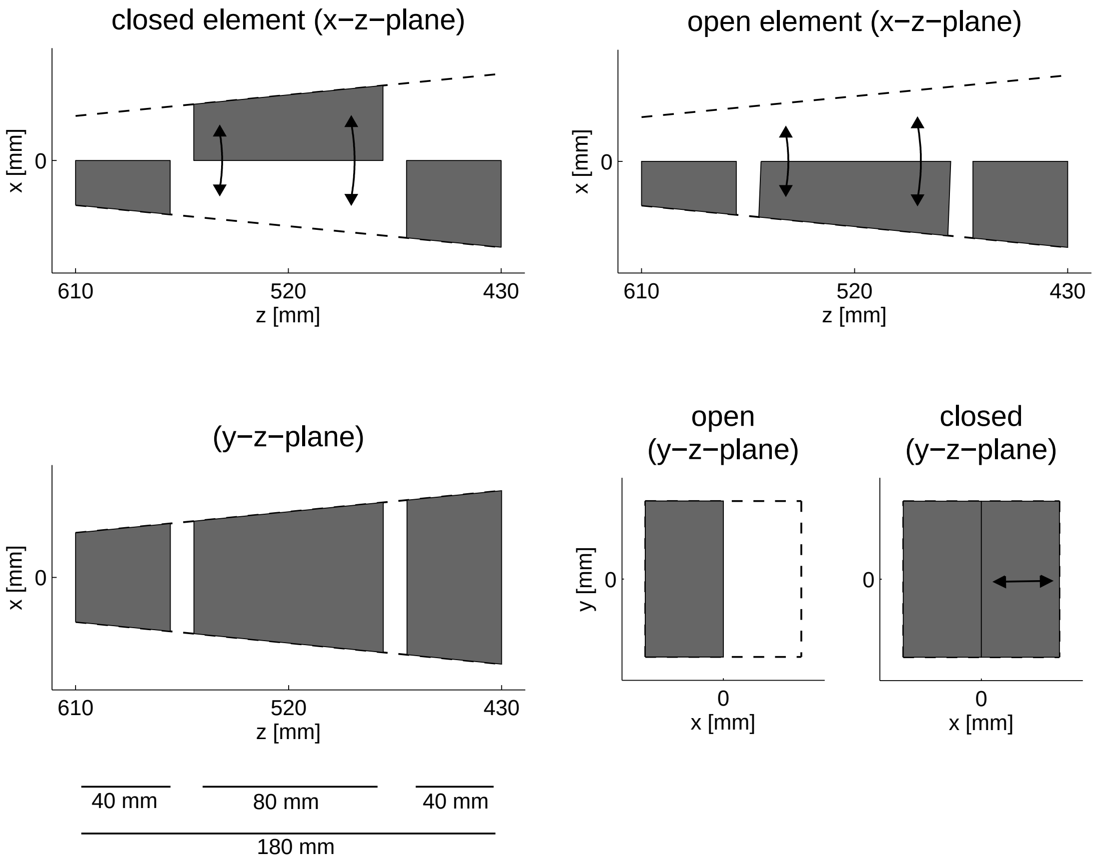

Figure 2.1: Principle design of a 2D-bMLC channel. Here, the central channel positioned on the z-axis of the GANTRY system is shown. The channel is focused on the source whose center has the coordinates $x = y = 0$ mm and $z = 800$ mm. To assure correct convergence of the channel in both states, open and closed, the central block has to be moved on a curved path. (not to scale)

The principle design of an absorber channel is shown in figure 2.1. Every channel consists of three blocks made of tungsten. Two blocks are fixed one behind another with a gap in between. The third block, denoted as the central block, can be moved between two positions: It can be placed in the gap between the two other blocks or it can be shifted laterally out of the gap. If all three blocks are in line (see figure 2.1 top-right), the channel is open. If the central module is shifted in respect to the fixed ones (figure 2.1 top-left) the channel is closed. The z-lengths of the three tungsten blocks, 40 mm, 80 mm, and 40 mm respectively, are the same for all channels. The x- and y-lengths depend on the distance source-collimator and on the channel's position on the spherical shell segment. (Equations for the exact dimensions of all absorbers are given in section 2.B.1.)

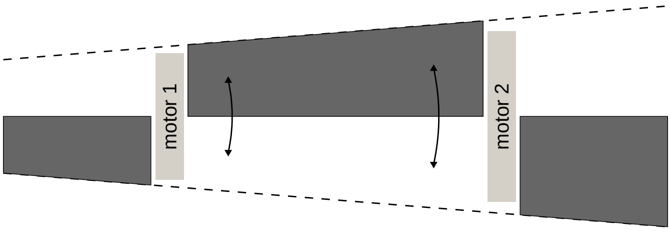

Figure 2.2: Motors could be placed in the gaps between the absorber blocks, on both sides of the central block.

For two main reasons, we present the configuration of the channel with three absorber blocks and not an alternative configuration with two blocks, one fixed and one movable. First, the configuration should minimise possible cross leakage through the blocks of a channel or across adjacent channels. Second, the configuration allows the installation of motors on both side of the movable central block, as it is shown in figure 2.2. The motors could be attached to the surrounding fixed elements. Of course, the configuration entails certain requirements concerning the size of the motors as well as the materials of their components. These engineering questions are not part of this work, but should be addressed in further studies.

All channels are focusing on the photon source, or rather on the target of the linear accelerator (linac). That is why we arranged the collimator channels on a spherical shell, with the linac target in its center. If a channel is open, a divergent photon beam can directly traverse one side of the channel. Figure 2.3 schematically shows the arrangement of the 900 channels on the spherical shell. Each channel is represented by two adjacent trapezoids, a light grey one and a dark grey one. If a channel is open, X-rays can traverse the channel through the light grey side.

The collimator is designed so that the beams of the most central channels have rectangular cross-sections with the dimensions 5×10 mm^2 in the isocentric plane. To realise exactly the same dimensions for all beams, the channels on the spherical shell would have to be narrowed in both directions, x and y. This would necessitate 900 individual channel geometries. If all channels are open, we would then obtain a quadratic radiation field of parallel stripes in the isocentric plane with the dimensions $300 \times 300\,\mathrm{mm}^2$. In contrast, in our implementation, the channels are narrowed only in y-direction. The pattern depicted in figure 2.3 is similar to that of latitude and longitudinal lines on a globe. As a consequence, the channels with same y-index are identical, and the number of different geometries is reduced to 30. Therefore, due to the selected design, the dimensions of the emerging channel beams vary slightly depending on their position. This can be seen in the geometrical projection of the beam cross sections onto the isocentric plane, which is shown on the right side of the figure. The resulting pattern looks like the slightly deformed pattern of parallel stripes described above. We calculated quantitative deviation maps from the geometrical projection. They can be found in 2.4.1. (Equations for the geometrical projections are given in 2.B.2.)

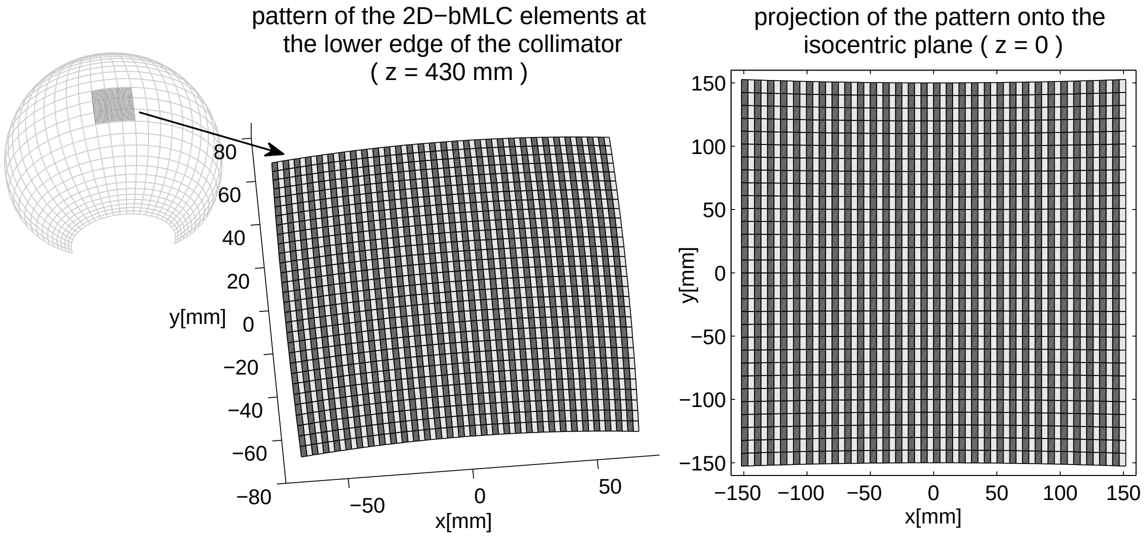

Figure 2.3: The channels of the 2D-bMLC are arranged side by side on a spherical shell around the photon source (left and middle). Each channel is represented by two adjacent trapezoids - a dark grey one and a light grey one. The channels are narrowed in y-direction and the pattern depicted is similar to that of latitude and longitudinal lines on a globe. The geometrical projection of the beam cross sections onto the isocentric plane is shown on the right side.

Now it becomes clear, why the number of collimator channels M and N cannot not be extended arbitrarily. The farther the channels are positioned from the center of the shell segment, the thinner they have to be designed. At a certain point, they become too thin to allow a proper production and operation (mechanical opening and closing). Also, at least in our implementation, the “deformation” of the 2D-bMLC field (see above) becomes larger with the distance to the center. By limiting the collimator to 30 by 30 channels, we assure that both, channel dimensions and the non-uniformity of the field, are in a reasonable range.

2.3.2 Indexing of 2D-bMLC channels

Figure 2.4 shows how we index the channels and the corresponding beams (bixel) of the 2D-bMLC. Two indices are assigned to each channel. The indices correspond to the columns and rows of the 2D-bMLC matrix, whose projection to the isocentric plane is shown schematically in the figure. Here, we omit the pattern deviations discussed in 2.3.1. The indices go both from 1 to 30, starting in the lower left corner. The first two digits of the labels represent the column index; the second two digits represent the row index.

2.3.3 Monte Carlo evaluation of the 2D-bMLC

2.3.3.1 Monte Carlo setup

The MC setup we used to evaluate the 2D-bMLC concept is shown in figure 2.5(a). As already mentioned the SAD is set to 800 mm. The collimator model is described in detail in 2.3.1. Additional tungsten modules surrounding the 30 by 30 collimator channels are added to the setup to block radiation passing the collimator on its sides. Each channel can be opened or

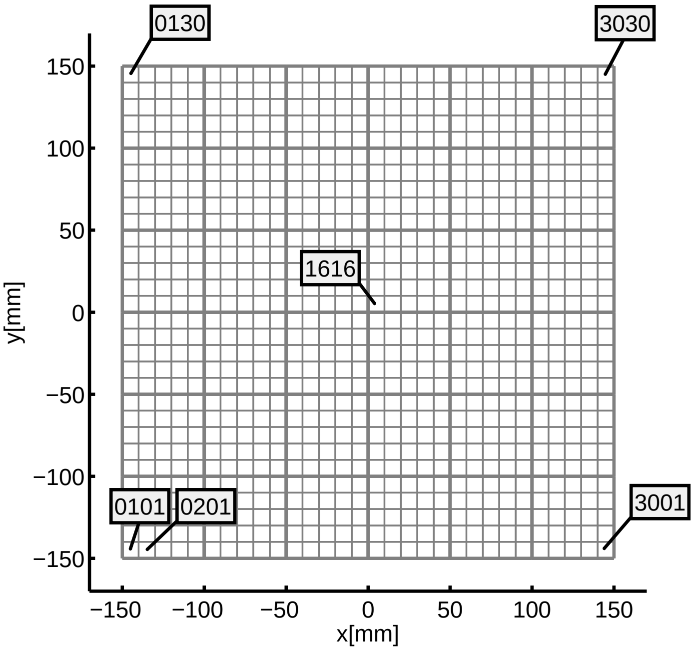

Figure 2.4: Principle of indexing of the 2D-bMLC channels. Matrix of 30 by 30 channels projected to the isocentric plane (here a regular pattern is shown without the deviations due to the specific design of the channels).

closed individually, so that any arbitrary pattern of open and closed channels can be modelled.

A simplified virtual source model of a flattening filter free (FFF) Siemens ARTISTE 7MV 160 MLC$^{\mathrm{TM}}$ was developed and used as surrogate for MC simulations of the linac phase space. The model consists of a planar photon source located close to the bremsstrahlung target of the linac. It represents a source of primary photons generated within the target. Since we want to model an unflat beam, a second virtual source, normally used to model the flattening filter, is not necessary. The standard deviation of the two-dimensional Gaussian shaped source is 0.45 mm. A profile of the primary photon fluence and the energy spectrum of the source photons are shown in figure 2.6. A detailed description of our source model, how it was fitted to experimental data, and of its validation can be found in 2.A.

Upstream the collimator, the source photons can be pre-collimated by a so called cookie cutter: All particles that do not pass a well defined aperture are not further simulated. In the current implementation the aperture is quadratic with variable side length. The phase space downstream the 2D-bMLC can be recorded in the optional phase space plane.

The phantom, a rectangular water tank, has the dimensions $500\times500\times400\,\mathrm{mm}^3$. In all simulations, its center is positioned on the z-axis. The source-surface distance (SSD) can be set to a desired value. The energy dose deposit is scored within the phantom in 3-dimensional Cartesian scoring meshes with 0.5 mm x- and y-resolution and variable z-resolution.

Statistical uncertainties

Statistical analysis was performed following the batch method. Each simulation was divided in N batches and in every batch k the dose d_i^k to a voxel i was calculated. After completion of all batches, the mean dose d_i to a voxel and the corresponding uncertainty s_{d_i} was calculated as

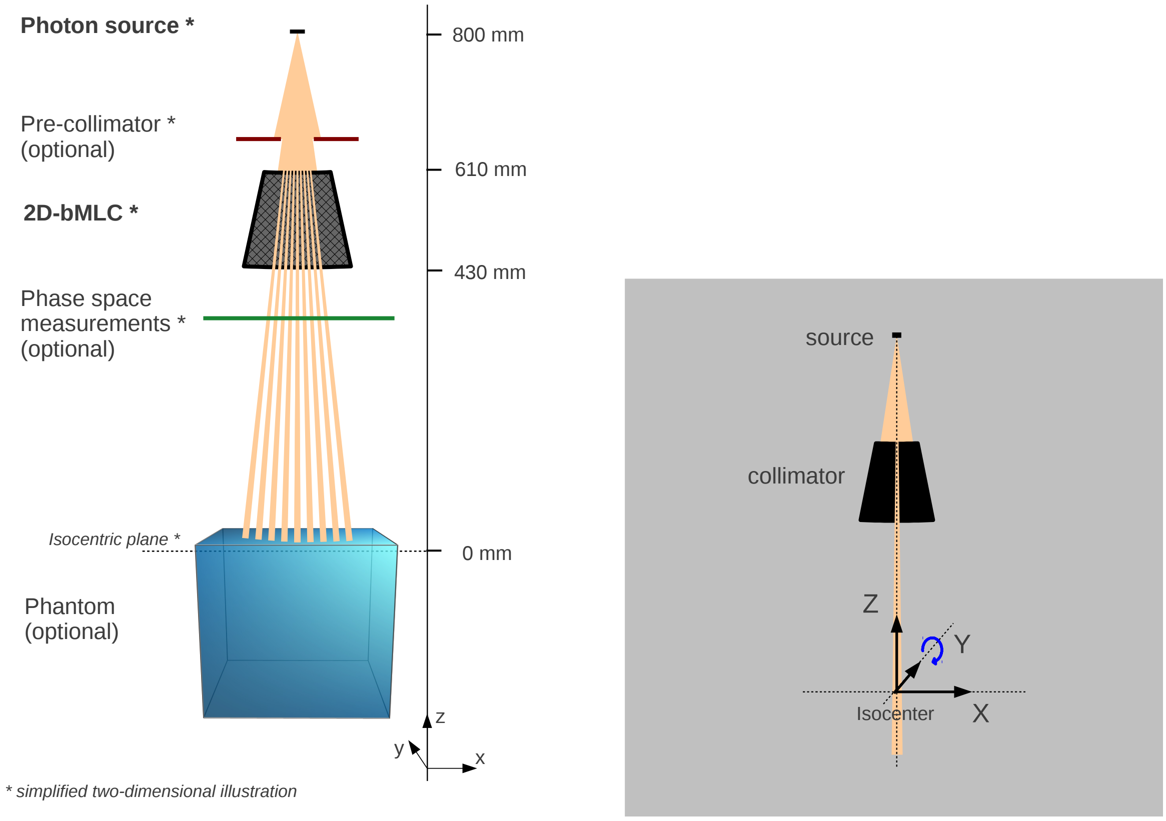

(a) MC setup

(b) GANTRY coordinate system

Figure 2.5: Schemes of the MC setup used for the evaluation of the 2D-bMLC (a) and of the GANTRY coordinate system (b), which was used for all descriptions in this work.

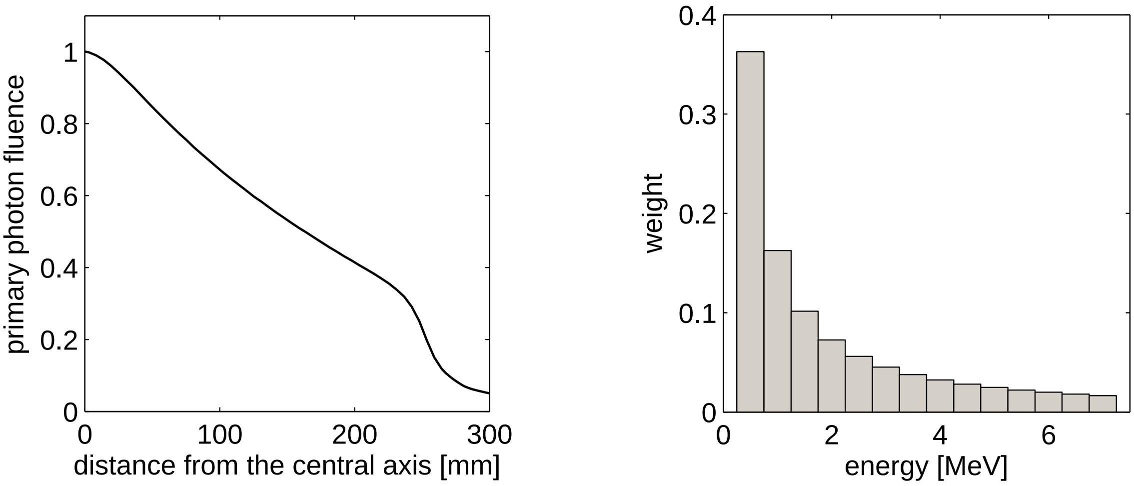

(a) primary photon fluence

(b) energy spectrum

Figure 2.6: Virtual source model of a FFF Siemens ARTISTE 7MV 160 MLC$^{\text{TM}}$: The primary photon fluence was directly calculated from a diagonal dose profile measured in 15 mm depth in water at 1000 mm SAD (a). The energy spectrum (b) as well as the source size were assessed by fitting Monte Carlo results to other experimental data. (See appendix for more details)

the standard error of the mean:

$$d_i = \sum_{k=1}^{N} \frac{d_i^k}{N} \qquad , \qquad s_{d_i} = \sqrt{\frac{\sum\limits_{k=1}^{N} \left(d_i^k - d_i\right)^2}{N(N-1)}} \tag{2.1}$$

The fractional uncertainty in dose for voxel i was defined as

$$F_{d_i} = \frac{s_{d_i}}{d_i} \quad . \tag{2.2}$$

In this study most evaluations were performed in 15 mm depth in water. As a measure of statistical uncertainty of a simulation, a mean fractional uncertainty for 15 mm depth in water was calculated as follows: F_{d_i} was averaged over all voxels at 15 mm depth and with a local dose deposit greater than 25% of the maximum dose at the same depth. The total number of primary particles was set for each simulation to ensure the following maximum mean fractional uncertainties in 15 mm depth in water: 2% for the simulations described in 2.3.3.4 and 2.3.3.5 and 5% for the simulations described in 2.3.3.3. For final evaluation the dose distributions were generally averaged over several voxel in one or more directions, so that relative uncertainties were further decreased. The same is true for dose distributions and dose profiles shown in the results section.

The simulations described in 2.3.3.4 and 2.3.3.5 were subdivided in two separate parts. In a first part the transport of the source photons through the tungsten elements of the collimator were simulated, and the phase space was scored in the phase space plane. In a second simulation the particle transport through the water phantom was simulated and the spatial dose deposition was scored. Here, a common variance reduction method was applied: Each phase space particle was reused 20 times, but each time with different random numbers.

All MC simulations were implemented with Geant4 version 9.4p02 (Agostinelli et al., 2003). A Geant4 standard electromagnetic physics list with best advanced electromagnetic options was used[1].

2.3.3.2 Reference field

To model an open reference field, the 2D-bMLC was removed from the setup shown in figure 2.5(a), and collimation was performed only by the pre-collimator. The SAD of 800 mm was not changed. The side length of the reference field in the isocentric plane was 100 mm. Dose was scored in the water phantom with 785 mm SSD. Unless otherwise noted, dose values presented in this work were scaled to 1 million primary particles and are given relative to the dose D_{ref}. D_{ref} is the dose scored in the center of the reference field in 15 mm depth in water and likewise scaled to 1 million primaries.

2.3.3.3 Efficiency and leakage

To estimate the efficiency of the 2D-bMLC, we performed a simulation, in which the 10 by 10 central channels of the collimator were opened. The corresponding bixel pattern is shown in figure 2.7(a). The pre-collimator was set as in the simulation for the reference field (see 2.3.3.2).

---

[1] The physics list was similar to that which is loaded with the physics list constructor emstandard_opt3. The physics list constructors are developed and maintained by the electromagnetic working group of the Geant4 collaboration. Further information can be found on `http://geant4.web.cern.ch/geant4/collaboration/working_groups/electromagnetic/physlist.shtml`.

To quantify the influence of electron contamination to the 2D-bMLC field, we scored the integral energy fluence for different particle types downstream the collimator in the phase space plane (see figure 2.5(a)). The relative contribution of electron contamination was estimated by dividing the energy fluence scored for electrons (and positrons) by the energy fluence scored for all particles.

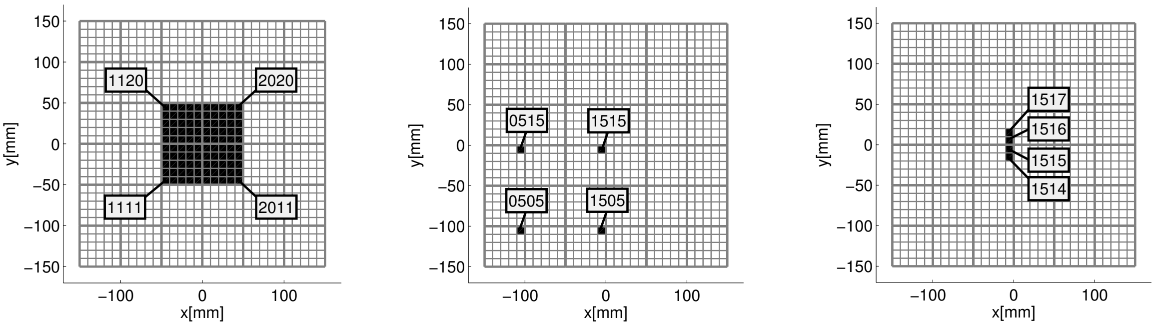

(a) pattern 1 (b) pattern 2 (c) pattern 3

Figure 2.7: Matrix of 30 by 30 channels projected to the isocentric plane. Open channels are labelled in black for the simulations described in 2.3.3.3 (a), 2.3.3.4 (b) and 2.3.3.5 (c).

A second simulation was performed in order to quantify the leakage of the 2D-bMLC. In this simulation all collimator channels were closed. In both simulations the SSD was set to 785 mm. Quantitative evaluations were made for the dose $D(x, y)$ scored in the isocentric plane, respectively in a water slab at 15 mm depth.

A relative efficiency factor was calculated using

$$EF = \frac{Integral\ Dose_{10\times 10 channels}}{Integral\ Dose_{reference}} \ . \tag{2.3}$$

The integral dose is the dose scored in the entire slab. $Integral\ Dose_{10\times 10 channels}$ refers to the simulation, in which the the central 10 by 10 collimator channels were open (figure 2.7(a)). $Integral\ Dose_{reference}$ is the integral dose calculated for the same slab in the simulation of the reference field.

A leakage map was calculated by dividing the dose scored for the closed 2D-bMLC by D_{ref}.

2.3.3.4 Width and penumbra of individual channel beams (bixels)

We calculated the spatial dose deposited in the water phantom by four different bixels, originating from the channels 0505, 0515, 1505, and 1515. The corresponding bixel pattern is shown in figure 2.7(b). The limitation to bixels from one quadrant of the 2D-bMLC is justified by the rotational symmetry of the photon source and the 2D-bMLC pattern. Again, the SSD was set to 785 mm. The following values were estimated for every bixel from dose profiles in 15 mm depth in water: Maximum dose, full width at half maximum (FWHM), 20%-80%-penumbra. For this, dose profiles in x- and y-direction, going through the maximum dose deposited by the respective bixel, were evaluated. Furthermore, the coordinates of each bixel's center was assessed by calculating the center between the points at half maximum of the x- and y-profiles.

2.3.3.5 Butting channel beams

To evaluate tongue-and-groove effects, the spatial dose deposited by four adjacent bixels, number 1514, 1515, 1516, and 1517 (see figure 2.7(c)), was calculated in two different ways. In a first MC simulation, the channels were opened simultaneously, whereas in a second simulation, they were opened one after another. Again, the SSD was set to 785 mm. Tongue-and-groove effects are expected because of the finite size of the photon source. To prove this, we repeated the second simulation with an infinite small source (point source). All other parameters of the source model were maintained.

2.4 Results

2.4.1 Deviation maps

The maps shown in figure 2.8 visualise the deviations of the geometric bixel cross sections in the isocentric plane from a perfect regular pattern. The regular pattern is characterised by constant bixel side lengths, 5 mm in x and 10 mm in y, and by a regular spacing of 10 mm in both directions. The coordinates of the bixel centres would match the following grids:

$$x \in \{\, -142.5mm\,,\ -132.5mm\,,\ -122.5mm\,,\ \ldots\,,\ 147.5mm\,\} \tag{2.4}$$

$$y \in \{\, -145.0mm\,,\ -135.0mm\,,\ -125.0mm\,,\ \ldots\,,\ 145.0mm\,\} \tag{2.5}$$

In the two upper maps of the figure, the deviations of our bixel centres from the respective coordinates given in (2.4) and (2.5) are color-coded. In the two lower maps, the side lengths of the geometric bixel cross sections are color-coded.

In the center of our 2D-bMLC pattern, deviations to the regular pattern disappear. Here, the bixel side lengths are very close to 5 mm respectively 10 mm, and the bixel position match in approximation the coordinates of the regular grid. At the pattern edges the maximum side lengths are about 5.17 mm in x and 10.17 mm in y. The maximal position deviations at the pattern edges are about ±2 mm in x-direction and about ±3 mm in y-direction.

2.4.2 Simulation design of the 2D-bMLC

In figure 2.9, we show images of the core of our 2D-bMLC Monte Carlo model. 30 trisected fan-like layers can be seen. They correspond to the x-indices. Each layer is composed of 30 collimator channels, placed side by side in y-direction and corresponding to the y-indices respectively. The division of the layers is due to the design of the channels, described above and shown in figure 2.1. Every collimator channel is made of three tungsten blocks, two fixed blocks and one central block which can be shifted between two positions. In both images shown in figure 2.9 all 2D-bMLC channels are open.

2.4.3 Monte Carlo evaluation of the 2D-bMLC

2.4.3.1 Efficiency and leakage

Figure 2.10 shows color maps of the dose distribution scored in 15 mm depth in water for the reference field and for the simulation performed to assess the efficiency of the collimator. In addition, averaged lateral profiles in x-direction are shown. The dashed rectangles in the maps indicate over which y-range the profiles were averaged. As outlined in 2.3.3.3, the dose

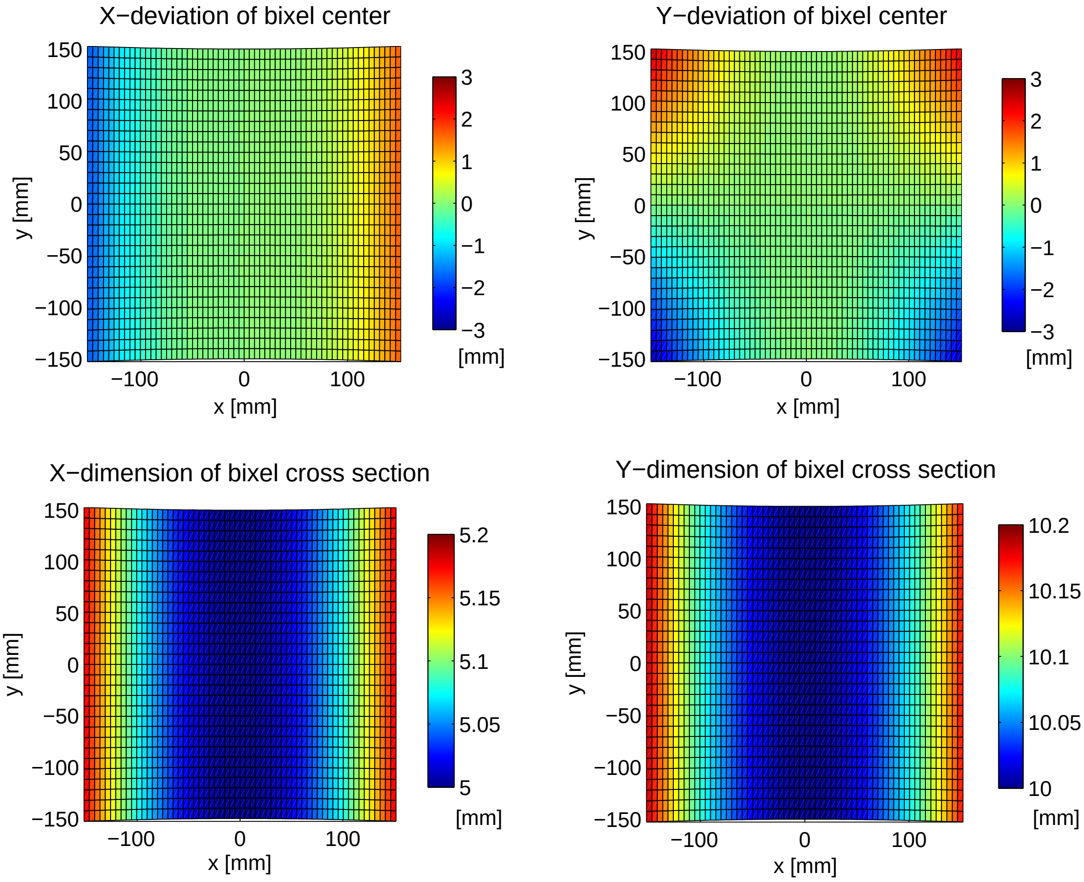

Figure 2.8: Geometrical projection of the 2D-bMLC pattern onto the isocentric plane. In x-direction every second trapezoid corresponds to one bixel cross section in the isocentric plane. Above: Deviations in x- and y-direction of the bixel center from the coordinates given in (2.4) and (2.5) are color-coded. Below: The dimensions of the geometrical bixel cross sections are color-coded.

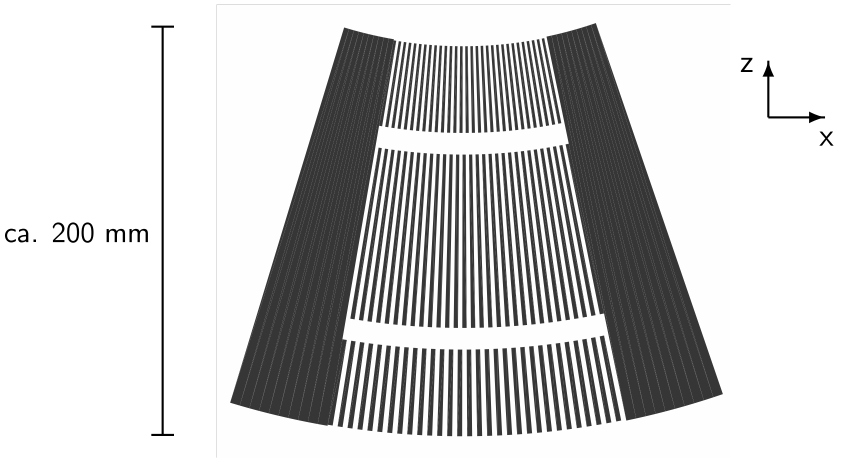

Figure 2.9: Cross section of the 2D-bMLC Monte Carlo model (to scale). See figure 2.5(a) and 2.1 for more dimensions.

distributions were scaled to the same number of primary particles and are shown relative to D_{ref}, whereas D_{ref} is the dose at the center of the reference field map[2]. The last stripe of the 2D-bMLC fileld in the positive x-direction seems to be diminished compared to the others. This is due to the fact that the same pre-collimation upstream the collimator was applied as in the simulation of the reference field. We calculated a relative efficiency factor (equation 2.3) as

$$EF = 0.43 \ .$$

The relative contribution of the electron contamination to the 2D-bMLC field was approximately 0.12%.

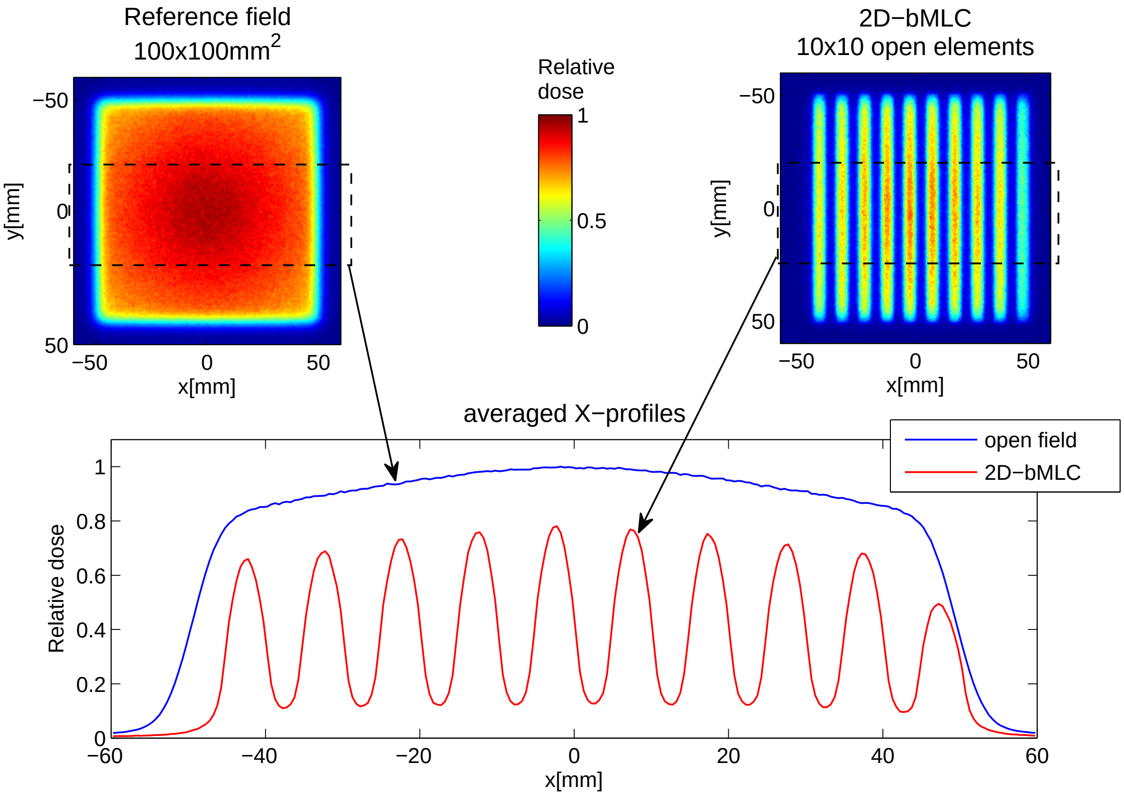

Figure 2.10: Dose maps of an open $100 \times 100\,mm^2$ reference field (above left) and a 2D-bMLC field (above right). In the simulation of the 2D-bMLC the central 10 by 10 channels were opened. The dose was scored in 15 mm depth in water (SSD 785 mm) and scaled relative to the maximum dose scored for the reference field. For the lateral profiles below, the dose distributions are averaged over 50 mm in y-direction (the profiles correspond to the rectangles in the dose maps).

In figure 2.11(a) the calculated leakage map is shown. For the figure the map was averaged over 20 by 20 neighbouring voxels to improve SNR. Because relatively few particles pass the completely closed 2D-bMLC, the SNR of the original leakage map with a lateral resolution of 0.5 mm was too low. The relative leakage ranges from about 0.1-0.2% at the field borders to about 0.4% in its center. The mean leakage, averaged from $-150\,\text{mm}$ to $150\,\text{mm}$ in x- and y-direction, is 0.25%. For Figure 2.11(b) we calculated lateral leakage profiles by respectively averaging the original map in one direction, whereas the resolution in the other direction was not changed.

---

[2] To assess D_{ref} with satisfying statistical accuracy, the dose was averaged over several voxel in x-, y-direction.

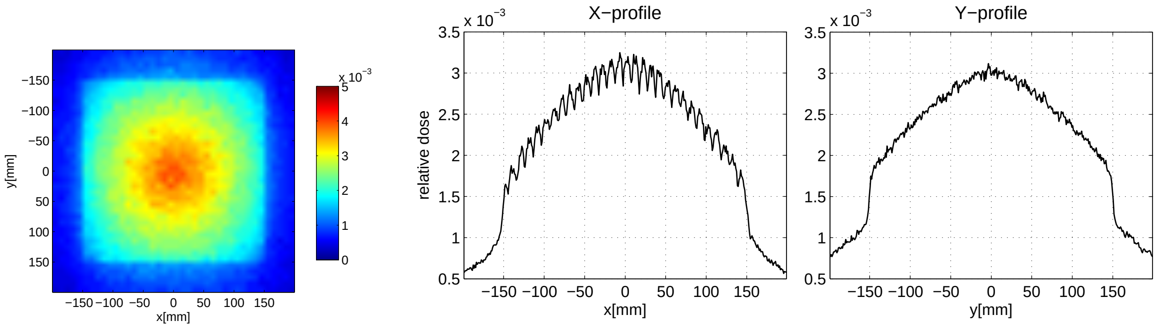

(a) Leakage map (in relative units)

(b) Averaged lateral profiles

Figure 2.11: (a) Leakage map calculated for the closed 2D-bMLC in the isocentric plane. (b) Lateral profiles of the leakage map. For the profiles the map was averaged over the whole 2D-bMLC field in y- and respectively in x-direction.

2.4.3.2 Width and penumbra of individual channel beams (bixel)

Figure 2.12 shows the lateral profiles of the dose deposited in 15 mm depth in water by bixel 0505, 0515, 1505, and 1515 respectively. The values presented in table 2.1 were assessed from these profiles. The center position and the FWHM of the profiles are in agreement with the values calculated from the geometric projection and discussed in 2.4.1. The profile's maxima, which are again given relative to D_{ref}, decreases with the distance of the respective element from the central axis of the treatment machine. The decrease follows the primary photon fluence distribution of the source model.The 20%-80%-penumbra of all bixel profiles is $1.7-1.8$ mm.

Table 2.1: Maximum, Central position (Center), full width half maximum (FWHM), and 20%-80%-penumbra of bixel profiles in the isocentric plane in 15 mm depth in water. Values were assessed by evaluating the X- and Y-profiles shown in figure 2.12. The maximum is given relative to the D_{ref} defined in 2.3.3.2 .

		X-profile			Y-profile		
Bixel	Maximum	Center	FWHM	Penumbra	Center	FWHM	Penumbra
1515	0.76	-2.5	5.1	1.7	-5.0	10.0	1.7
1505	0.45	-2.5	5.1	1.8	-105.0	9.9	1.8
0515	0.46	-103.1	5.2	1.7	-5.0	10.1	1.8
0505	0.34	-103.1	5.2	1.7	-105.9	10.1	1.7
	[a.u.]	[mm]	[mm]	[mm]	[mm]	[mm]	[mm]

2.4.3.3 Butting channel beams

To investigate tongue-and-groove effects, four adjacent bixel were opened simultaneously in a first simulation and one after another in a second simulation. We compare the dose distributions calculated in 15 mm depth in water. Lateral dose profiles in y-direction, going through the distributions maxima at $x = -5$ mm, are shown in figure 2.13. The bixel do not adapt perfectly if opened consecutively, but small minima can be observed where they abut. The dose is reduced in these regions by up to 5% in approximation. This effect is not present if the bixels are all open simultaneously.

In figure 2.13 on the right we also show the profile calculated for an infinite small point source. No tongue-and-groove effect is apparent. Moreover, in all the profile is about several percent

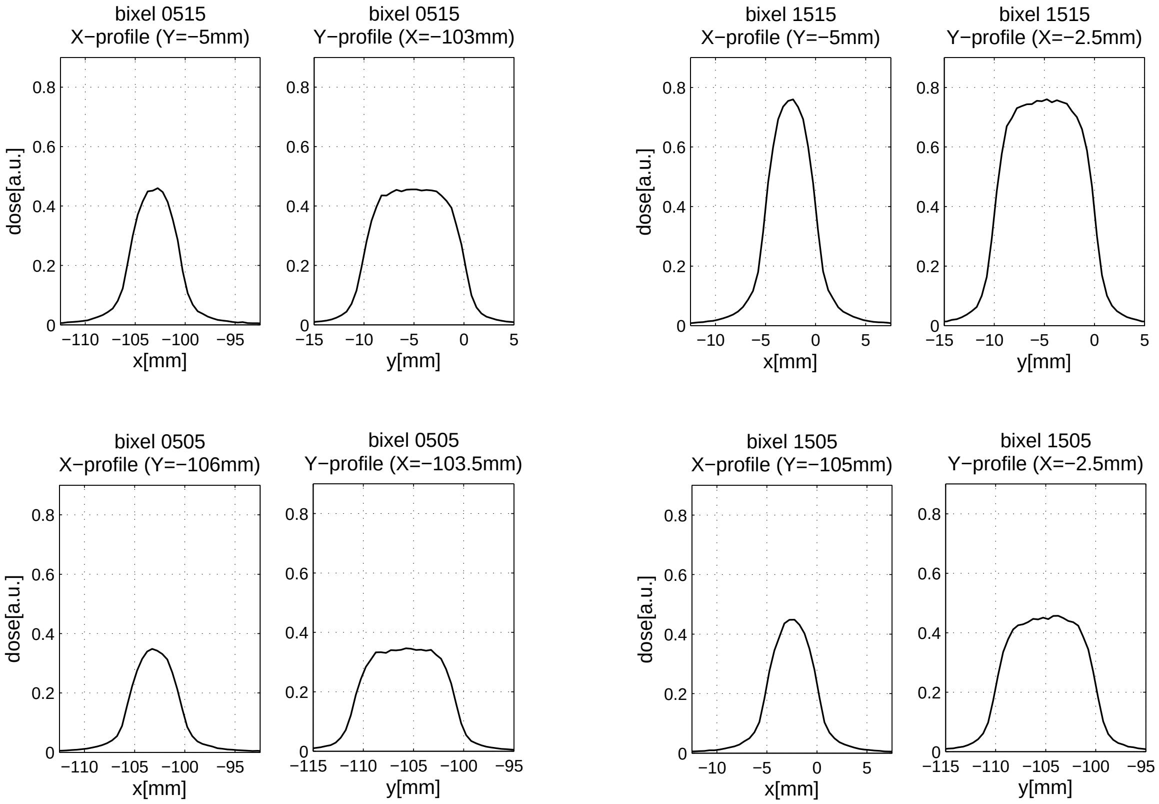

Figure 2.12: Lateral dose profiles of bixels 0505, 0515, 1505, and 1515 in 15 mm depth in water. The bixel pattern corresponding to the MC simulation is shown in figure 2.7(b).

higher then the one obtained for the finite source because of an increased primary radiation efficiency.

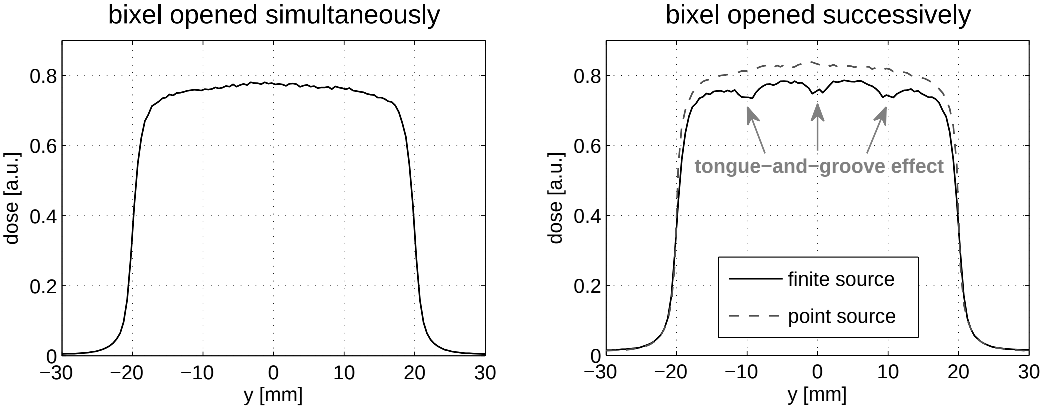

Figure 2.13: Dose profiles calculated in 15 mm depth in water for four adjacent bixel, which were opened simultaneously or in succession. The corresponding bixels are labelled in figure 2.7(c). The lateral profiles in y-direction go through the maxima of the dose distributions ($x = -2.5$ mm). On the right side in addition to the result for the Gaussian shaped finite source, a profile calculated for a point source is shown.

2.5 Discussion

The relative intensities of the channel beams follow the primary photon fluence distribution of the source model. The geometric widths of the most central bixel in the isocentric plane are approximately 5 mm in one and 10 mm in the other direction. Towards the borders of the 2D-bMLC field, the widths increase in a symmetric manner by up to 4%. The central axes of the bixels as well as the change of their widths can be approximated by geometric calculations. These calculations could be affirmed by the MC results. In addition, the simulation of the individual bixels showed that the beam penumbra does not change considerably between different bixels.

We arranged the collimator channels on a spherical shell; each channel focus on the linac source. Compared to a collimator composed of parallel rectangular channels, our design should result in a higher primary radiation efficiency. Certainly, because in one half of each channel the radiation is always blocked, the efficiency cannot exceed 50%. Moreover, this value would only be attainable for a point source, and the efficiency further decreases with the source size. Geometric consideration suggest that the source size together with the distance source-collimator and the dimensions of the absorber channels determine the geometric penumbra of a bixel, and, more generally, how many particles can pass through the openings. For a two-dimensional Gaussian shaped source with a standard deviation of 0.45 mm ($\mathrm{FWHM} = 1.06$ mm), we calculated a primary radiation efficiency of approximately 43% for the 2D-bMLC. According to the consideration mentioned above, one could potentially increase the efficiency, if the source size could somehow be reduced. Given a fixed source size, the efficiency could slightly be improved by shortening the 2D-bMLC channels or by increasing the distance between the source and the collimator. However, the shortening of the absorber channels would result in higher leakage, whereas a considerable increase of the distance source-collimator would implicate an increase of the SAD of the treatment machine.

A slight tongue-and groove under-dosage was observed, if adjacent beams were opened subsequently and not at the same time (see figure 2.13). Just as the reduced efficiency, also the tongue-and-groove effect, is explained by the finite source size and would diminish, if all photons would originate from one point. The under-dosage is restricted to about 2 mm in the regions where the beams abut. The maximum relative under-dosage is approximately 5%. The effect should be considered in a treatment planning algorithm to avoid uncertainties, even though, the effect is less pronounced than similar tongue-and-groove effects exhibited by conventional MLCs. If two adjacent irradiation fields of these collimators are combined, relative under-dosage of 10-40% can be observed at the boundary line.(Huq et al., 2002; Tacke et al., 2008)

The average leakage calculated for the 2D-bMLC is 0.25%. It is mainly affected by intra-leaf leakage, thus by the transmission through the tungsten absorbers of the collimator channels. Only relatively weak additional inter-leaf leakage is present. The latter leads to the wiggly character of the x-profile, shown in figure 2.11(b). The maximum of the leakage can be estimated to about 0.4% in the center of the collimator. As the primary photon fluence distribution, the leakage decreases with the distance to the central axis of the treatment machine. The calculated leakage of the 2D-bMLC is in the same range of the leaf transmission measured for the ARTISTE 6MV 160 MLC$^{\text{TM}}$ with flattening filter (Tacke et al., 2008). Of course, additional leakage could be caused by possible mechanical imperfections, which are not considered in the current model.

General discussion of the 2D-bMLC concept

Referring to the ideas described in (Heid, 2010), the 2D-bMLC consists of individually controlled absorber channels, which form a two-dimensional collimator aperture in the form of a matrix. The design aims for an easy and rapid modulation of the aperture. Arbitrary modulation patterns could be realised with relatively short time delays, affected by the time needed to open and close the channels. This could be an advantage of the 2D-bMLC over conventional MLC techniques. Due to mechanical limitations of the leaf speed, subsequent modulation patterns delivered with conventional MLC techniques are strongly correlated or considerable dead times in between the delivery have to be accepted.

A disadvantage of the concept could be the fragmentation of the radiation field and the related reduction in beam utilisation efficiency. Moreover, because aperture modulations are limited to open and closed bixels, their resolution is determined by the widths of the bixels. As discussed above the geometrical widths are approximately 5×10 mm in the isocentric plane. In contrast, fields of modern conventional MLCs can generally be shaped with higher precision. The leafs of the ARTISTE 6MV 160 MLC$^{\text{TM}}$ have for example a projected width of 5 mm (Tacke et al., 2008). This parameter corresponds to the y-resolution in the GANTRY system. In the the x-direction, the leaf-travel direction, the resolution is only limited by the precision of the leaf-driving motors.

The dosimetric characterisation of the 2D-bMLC model shows that the concept can be used for radiotherapy treatments. The 2D-bMLC fields are well defined with a maximum extent of approximately 300 by 300 mm^2 in the isocentric plane. Compared to open fields, the beam utilisation efficiency is reduced by approximately 57%. The leakage is comparable to that of conventional collimators, tongue-and-groove effects are of minor importance. Because of the field fragmentation, the 2D-bMLC concept is certainly not well suited for static IMRT treatments with only a few beam directions. However the 2D-bMLC may be used in rotational IMRT treatments, in which beams from the continuously rotating gantry are superimposed in the patient.

As we mentioned in the introduction, a possible application of the 2D-bMLC could be in fast rotational IMRT. To speed up considerably rotational IMRT treatments, in a first instance, the dose rates of medical linacs has to be increased, as it has been done in recent developments by removal of the flattening filter (Georg et al., 2011; Salter et al., 2011). If delivery times of rotational IMRT treatments could even be reduced to times below those of anticipated organ movements, the motion could be ‘frozen’ during the dose delivery. This could be advantageous in cases in which intrafraction organ or tumour motion becomes a limitation of the geometrical accuracy of the treatment. Such a strategy could potentially be realised with a 2D-bMLC.

From the figures 2.1, 2.3 and 2.9 it is apparent that the 2D-bMLC model makes high demands on the geometrical and mechanical precision of the collimator. Slight geometrical misalignment of the collimator on the whole or of its components would lead to a shift of the radiation field and eventually reduce the primary radiation efficiency. A detailed study of the influence of geometrical and mechanical misalignment, e.g. caused by manufacturer tolerances, is one of our next steps.

2.6 Conclusion

A novel technical concept of a two-dimensional binary collimator (2D-bMLC), specially designed for fast dose delivery in rotational IMRT, was presented. We successfully established and evaluated a dosimetric model of the 2D-bMLC. The results were promising and allowed us to integrate the 2D-bMLC into the treatment planning tool that is presented in chapter 3.

2.A Details: Source Model of Siemens ARTISTE 7MV 160 MLC$^{\text{TM}}$

A simplified virtual source model of a flattening filter free (FFF) Siemens ARTISTE 7MV 160 MLC$^{\text{TM}}$ was developed for the use as surrogate in Monte Carlo simulations.

2.A.1 Methods

2.A.1.1 Source model

The model consists of a planar photon source located close to the bremsstrahlung target. It represents a source of primary photons generated within the linac target. Since we want to model an unflat beam, a second virtual source, normally used to model the flattening filter is not necessary. The influence of other extra-focal photons and of contamination electrons is supposed to be of minor importance and not considered.

The source is described by three independent distributions:

- A Gaussian-shaped planar source distribution $d_{planar}\left(x,y\right)$
- A circular angular distribution $d_{angular}\left(\theta\right)$ for the direction of the source photons
- An energy distribution of the source photons $d_{energy}\left(E\right)$

x and y are coordinates of the GANTRY system (figure 2.5(b)) and θ is the angle between the photon direction vector and the central axis of the treatment machine, respectively the negative z-axis of the GANTRY system. In reality, the energy distribution may depend on the angle θ. This dependence is way more important for machines with flattening filter where the occurring beam hardening depends on the angle θ. Without flattening filter the influence is of minor importance (Dalaryd et al., 2010) and is neglected in the presented model.

To adjust the model to the FFF Siemens ARTISTE 7MV 160 MLC$^{\text{TM}}$, the following procedure was applied: First, the angular distribution $d_{angular}\left(\theta\right)$ was assessed directly by primary fluence measurements (see 2.A.1.3). The energy distribution and the planar distribution of the source position were then calculated by fitting Monte Carlo (MC) results to other experimental data (see 2.A.1.4 and 2.A.1.5).

2.A.1.2 Experimental data and MC setup

Dose measurements were carried out at the German Cancer Research Center with an experimental Siemens ARTISTE 7MV 160MLC$^{\text{TM}}$, the PTW MP3 water tank with the dimensions $500\times500\times400\,\text{mm}^3$ and the PTW 60008 Diode P. The source-axis distance (SAD) was 1000 mm the source-surface distance (SSD) either 950 mm or 985 mm. Measurements were performed with quadratic fields of various side length. The experimental data includes percentage depth dose curves (PDD) and central lateral dose profiles measured in different depths in water.

The MC setup is shown schematically in figure 2.14. As (Fippel et al., 2003) suggested, a simplified model of the collimating system was used: Two tungsten jaw pairs, denoted X-MLC and Y-jaws, modify the x- and y-dimensions of the beam. The Y-jaws have planar inner faces focusing the center of the photon source. The form of the X-MLC is based on a realistic description of the multileaf collimator (Tacke et al., 2006). Adapting the jaw openings, any rectangular field can be collimated (up to a $400\times400\text{mm}^2$-field in the isocenter plane). The water tank was modelled by a block of water with the respective side lengths. The dose was calculated within the phantom in Cartesian scoring meshes. The MC simulations were implemented with

Geant4 version 9.4 (Agostinelli et al., 2003). A Geant4 standard electromagnetic physics list with best advanced electromagnetic options was used[3].

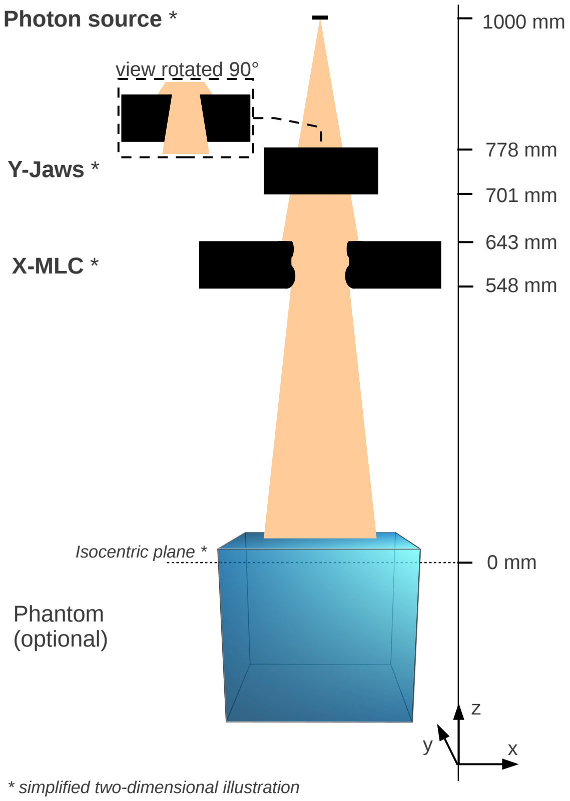

Figure 2.14: Schemes of MC setup used for the assessment of source model parameter. The collimating system consists of two jaw pairs with variable opening: The Y-jaws with planar inner faces focusing the center of the photon source and the X-MLC whose form is based on a realistic description of the MLC.

2.A.1.3 Angular distribution

The relative angular distribution was directly calculated from a dose profile measured at the phantom surface at 15 mm depth (SSD 985 mm). At this depth, the measured dose is assumed to be proportional to the primary photon fluence distribution. A diagonal dose profile from the center of a $400{\times}400\text{mm}^2$-field to one of its corners was assessed. d_i is the dose measured at the distance r_i to the center of the field. The discrete profile was converted into a discrete angular distribution using

$$d_{angular}\left(\theta_i\right) = N_{angular}\, d_i\, \frac{sin\theta_i}{cos^2\theta_i} \tag{2.6}$$

with

$$\theta_i = atan\left(\frac{r_i}{1000\,mm}\right) . \tag{2.7}$$

---

[3] The physics list was similar to that which is loaded with the physics list constructor emstandard_opt3. The physics list constructors are developed and maintained by the electromagnetic working group of the Geant4 collaboration. Further information can be found on `http://geant4.web.cern.ch/geant4/collaboration/working_groups/electromagnetic/physlist.shtml`.

$N_{angular}$ is a normalisation factor. Finally, the angular distribution was interpolated to a finer θ-grid.

2.A.1.4 Energy distribution

(Fippel et al., 2003) proposed a relatively simple analytical function to model the energy spectrum of a medical linear accelerator:

$$d_{energy}(E) = N_{energy}\, E^{l}\, exp(-bE)\ ,\ E_{min} \leq E \leq E_{max}\ , \tag{2.8}$$

where N_{energy} is a normalisation factor. To determine the free parameters l and b, a set of monoenergetic PDD was calculated for a $100{\times}100\text{mm}^2$-field using the MC method. The calculated monoenergetic PDD were superimposed using (2.8) and fitted to a measured PDD. Monoenergetic PDDs were calculated for energies from 0.5 MeV to 7 MeV, in steps of 0.5 MeV. In the MC simulations, the source was modelled by a point source, since the real source size was not yet determined. The direction of primary photons was sampled from the measured relative angular distribution. Fitting was performed with MATLAB® lsqcurvefit method (non-linear curve-fitting in least-squares sense using a trust-region-reflective algorithm). The first 4 millimetres of the PDD were not included in the fit because measurement errors are possibly not negligible here.

2.A.1.5 Source size

At last, the source size was assessed. The planar source distribution is given by a two-dimensional Gaussian perpendicular to the forward direction (negative z-direction):

$$d_{planar}(x,y) = N_{planar}\,\exp\left(-\frac{x^2}{2\sigma_x^2} - \frac{y^2}{2\sigma_y^2}\right) \tag{2.9}$$

with a normalisation factor N_{planar} and the standard deviations σ_x and σ_y. The latter were obtained by fitting the penumbra regions of lateral dose profiles calculated in water by means of MC simulations to those of the measured profiles. The shape of the beam penumbra is mainly influenced by the size of the photon source. The standard deviations σ_x and σ_y could be restricted to a maximum of 3 mm before starting MC simulations. Values above are not expected in a medical linac. Lateral in-plane (y-directions) and cross-plane (x-direction) profiles were calculated for quadratic fields of different size (side lengths between 20 and 200 mm) and in different depths in water (15, 50, 100 and 200 mm). Profiles were assessed for various σ_x and σ_y and were compared to measured dose profiles. In this manner, the standard deviations giving the best agreement in the penumbra regions were determined.

2.A.1.6 Validation of source model

For validation, we performed MC simulations including the developed source model and compared the results to the experimental data. Simulations were performed with 950 mm SSD and with quadratic fields of side length 20 mm, 50 mm and 100 mm. Spatial dose distribution, calculated within the water phantom, was scaled relative to the dose in the field center in 50 mm depth. Lateral in-plane and cross-plane dose profiles as well as PDD were compared to measured profiles scaled in the same way.

2.A.2 Results

2.A.2.1 Source model

Figure 2.15 shows on the left the relative measured dose profile assumed to be proportional to the primary photon fluence and on the right the angular distribution deduced following (2.6) and (2.7). The angular distribution interpolated to a finer θ-grid (grey) was used in the final source model. The fitting of the calculated monoenergetic PDD to the measured PDD, using (2.8), resulted in the model parameters $l = -1.1517$ and $b = 0.0077\,\mathrm{MeV}^{-1}$. The final energy distribution of the source photons is shown in figure 2.6(b). The standard deviations of the planar position distribution 2.9 were assigned to $\sigma_x = \sigma_y = 0.45$ mm.

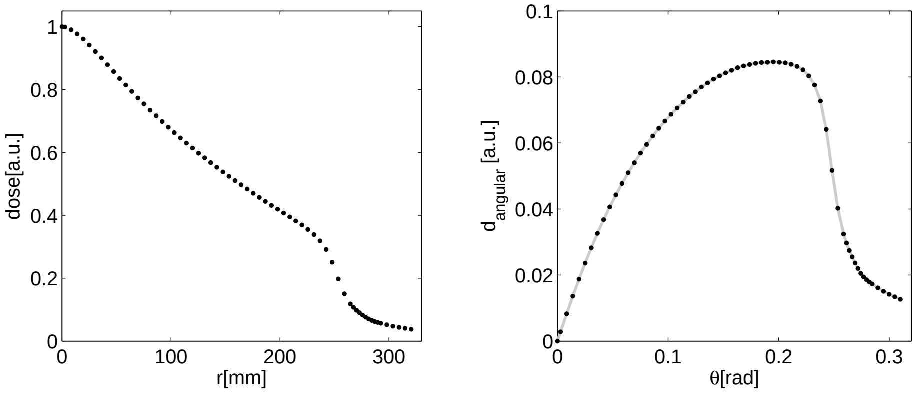

Figure 2.15: Left: measured diagonal dose profile (maximum set to one). Right: unnormalized deduced angular distribution for primary photons which is interpolated to a finer grid (grey).

2.A.2.2 Validation of source model

In figure 2.16, calculated lateral dose profiles and PDD are shown in comparison with the experimental data. Here, profiles are shown for 50 and 100 mm depth in water, but in general, agreement was similar in 15 and 200 mm depth. The relatively good agreement between calculated and measured dose profiles validates the developed source model. An improved and more complex source model could potentially reduce the small differences observed at the edges of the lateral profiles.

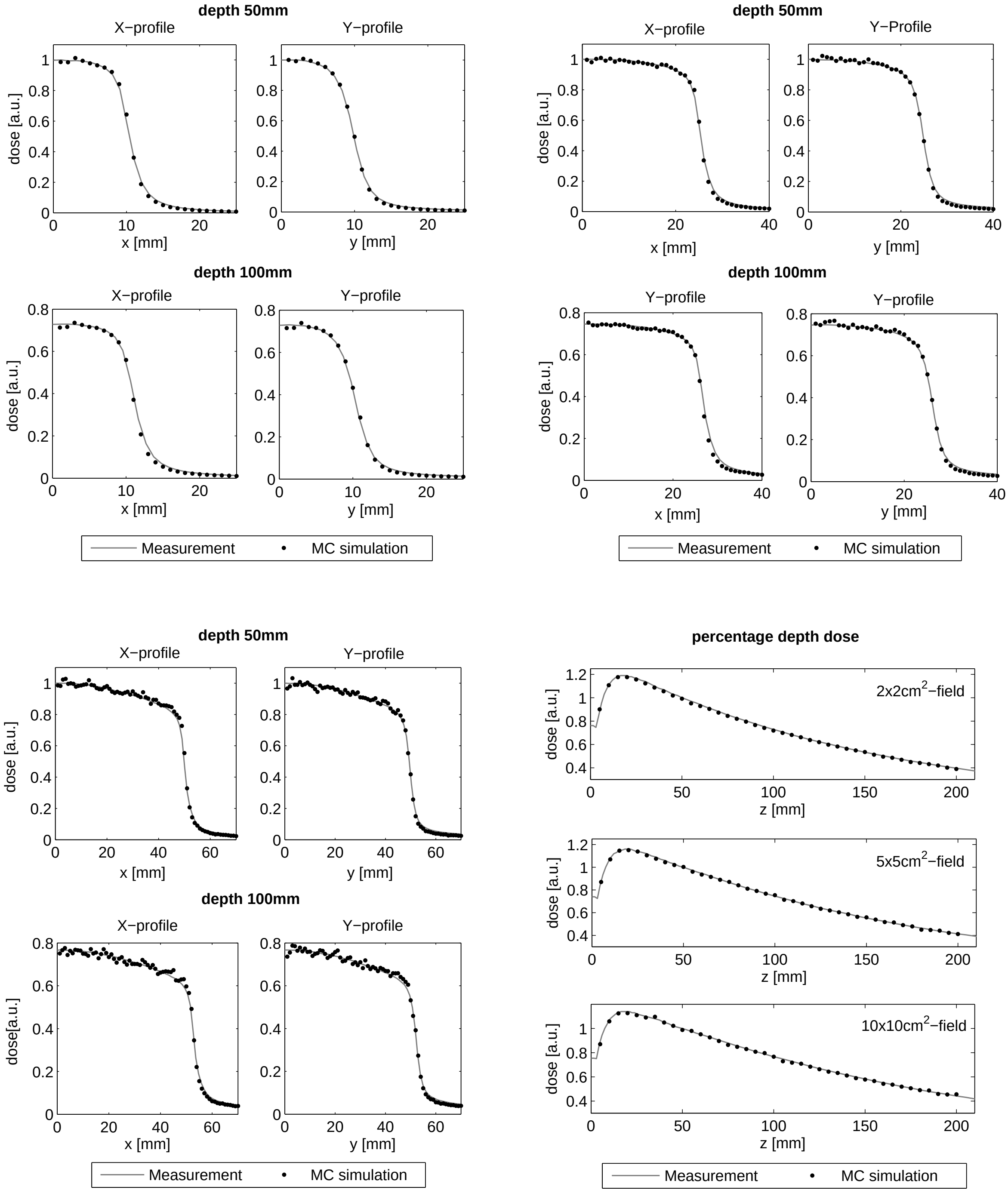

Figure 2.16: MC simulations vs. measurements: Comparison of lateral dose profiles and of PDD (below right) in water for three different field size: 2×2 cm^2, 5×5 cm^2, 10×10 cm^2. For each field size, calculated and measured dose profiles were scaled relative to the dose in the field center in 50 mm depth.

2.B Details: 2D-bMLC Design

2.B.1 Dimensions of absorber modules

The design of the 2D-bMLC is explained in 2.3.1. In figure 2.1 the principal design and functionality of an absorber channel is shown, and figure 2.3 illustrates how the 900 channels are arranged side by side in a tessellated pattern on a spherical shell segment. In this section, we explain how to exactly calculate the dimensions of the channel absorbers.

The indexing of the 2D-bMLC channels is explained in 2.3.2. Here, the two indices corresponding to the column and row indices in 2.3.2 are denoted ix and iy:

$$ix = 1, 2, 3, ..., 30 \tag{2.10}$$

$$iy = 1, 2, 3, ..., 30 \tag{2.11}$$

In figure 2.18, a closed absorber channel is shown. The three absorbers are denoted A, B and C respectively. In the following, we give the equations, which can be used to compute the vertexes of the absorbers for each channel, thus for each 2-tuple (ix, iy). The coordinate system used for the calculations is shown in figure 2.17. Its origin lies at the position of the linac source. The directions X, Y and Z' corresponds to the directions X, Y and -Z of the GANTRY system (see figure 2.5(b)).

The vertexes of the absorbers lie on spherical shells around the linac source. The radii of the spheres are given in figure 2.17(a).

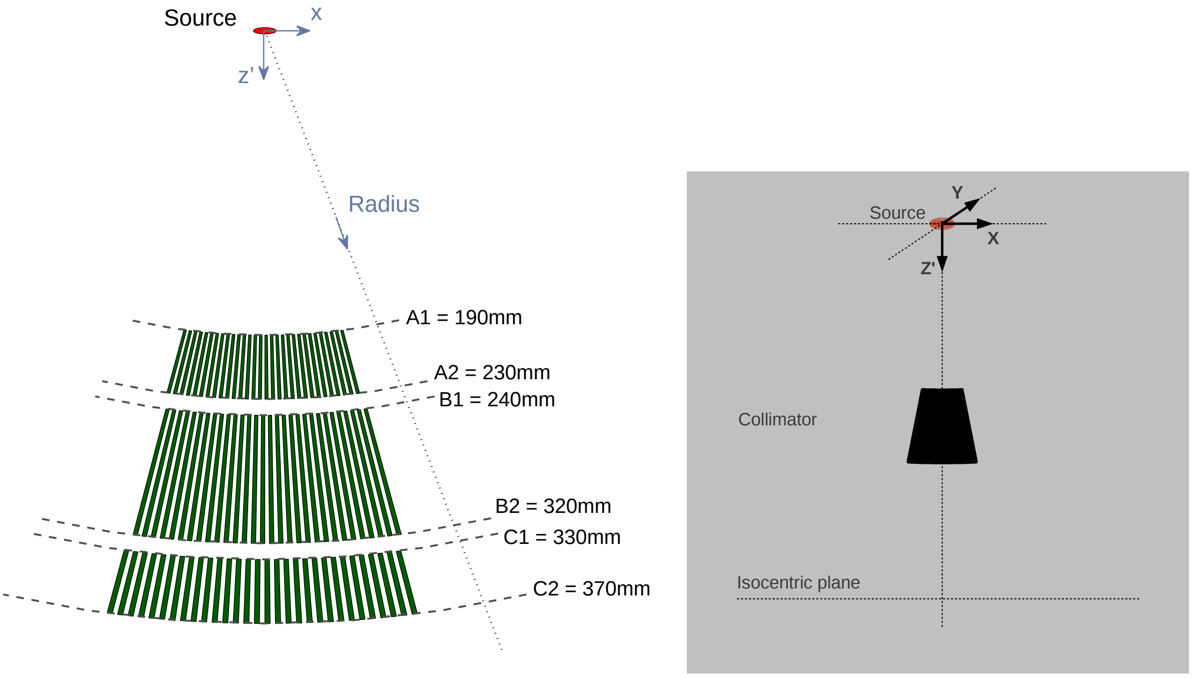

(a) The vertexes of the absorber elements lie on spherical shells around the linac source. Two radii are given for the absorber elements A, B and C respectively.

(b) Coordinate system

Figure 2.17: Radii and coordinate system used in the calculations of the absorber vertexes.

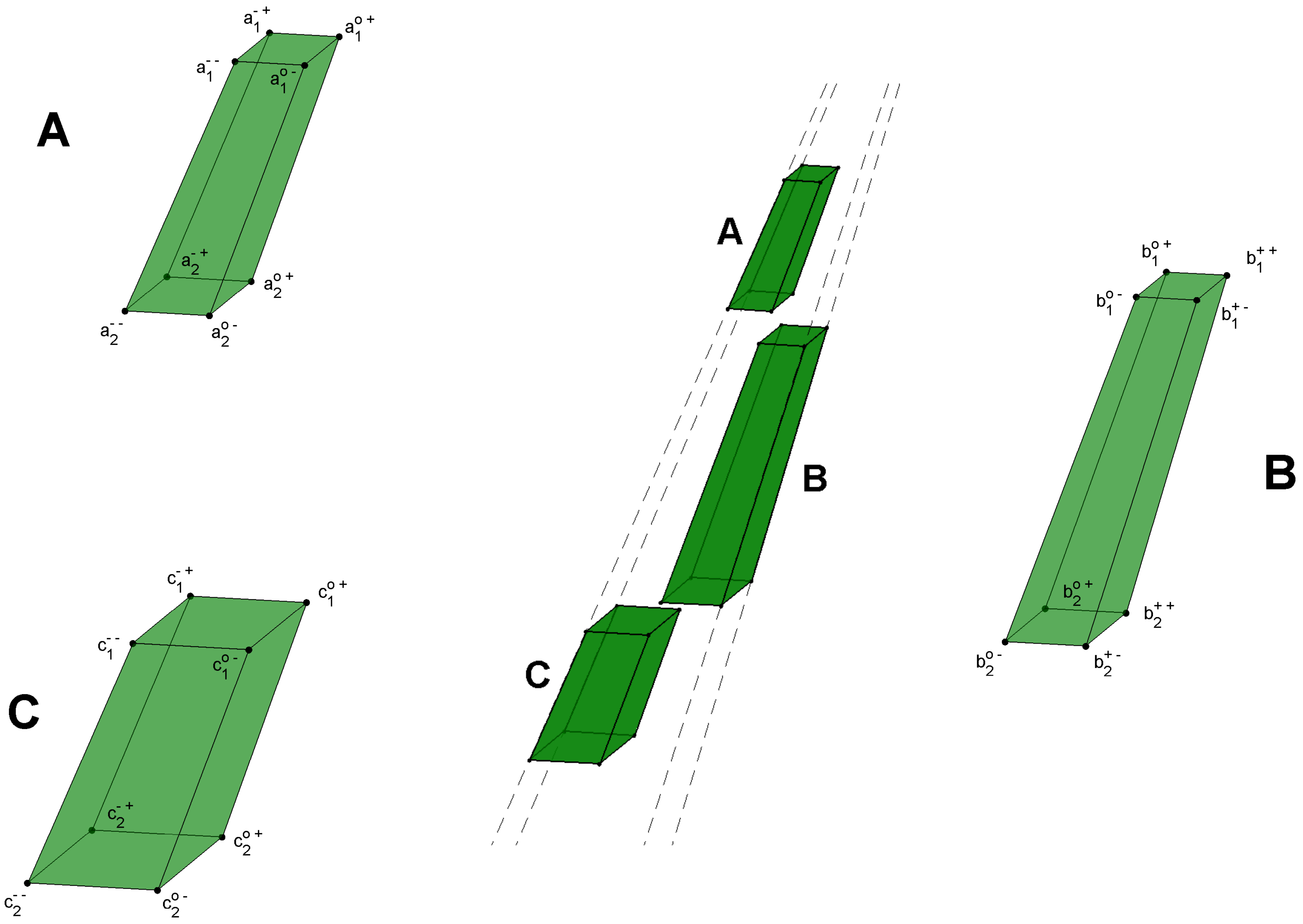

Figure 2.18: Vertexes of the absorbers A, B and C placed in a closed channel.

Further, we define the base length Δ_b and the base angle α_b:

$$\begin{aligned}\Delta_b &= 5\,\mathrm{mm} && (2.12)\\ \alpha_b &= \arctan\left(\frac{\Delta_b}{SAD}\right) && (2.13)\end{aligned}$$

with the source-axis distance SAD = 800 mm. Δ_b is half the requested side length of the projection of a channel onto the isocentric plane. We assign a set of angles to channel (ix,iy):

$$\begin{aligned}\alpha_{ix}^{-} &= (2\cdot ix-32)\,\alpha_b && (2.14)\\ \alpha_{ix}^{o} &= (2\cdot ix-31)\,\alpha_b && (2.15)\\ \alpha_{ix}^{+} &= (2\cdot ix-30)\,\alpha_b && (2.16)\end{aligned}$$

and

$$\begin{aligned}\alpha_{iy}^{-} &= \arctan\left((iy-16)\,\frac{\Delta_b}{SAD}\right) && (2.17)\\ \alpha_{iy}^{+} &= \arctan\left((iy-15)\,\frac{\Delta_b}{SAD}\right) && (2.18)\end{aligned}$$

On the following page, we give the equations for the vertexes of the absorbers placed within the closed channel (ix,iy). In principle, the equations correspond to rotations around the X- and Y-axis subsequently applied to a vector $(0, 0, R)$, where R is one of the radii given in figure 2.17(a). The angles of rotation are given by the equations 2.14 to 2.18. As an example, we give the detailed calculation of the vertex a_1^{--} for channel (ix,iy):

$$\begin{aligned}a_1^{--} &= \begin{pmatrix}\cos(\alpha_{ix}^{-}) & 0 & \sin(\alpha_{ix}^{-})\\ 0 & 1 & 0\\ -\sin(\alpha_{ix}^{-}) & 0 & \cos(\alpha_{ix}^{-})\end{pmatrix}\cdot\begin{pmatrix}1 & 0 & 0\\ 0 & \cos(\alpha_{iy}^{-}) & \sin(\alpha_{iy}^{-})\\ 0 & -\sin(\alpha_{iy}^{-}) & \cos(\alpha_{iy}^{-})\end{pmatrix}\cdot\begin{pmatrix}0\\0\\A1\end{pmatrix}\\ &= A1\cdot\begin{pmatrix}\sin(\alpha_{ix}^{-})\cos(\alpha_{iy}^{-})\\ \sin(\alpha_{iy}^{-})\\ \cos(\alpha_{ix}^{-})\cos(\alpha_{iy}^{-})\end{pmatrix} && (2.19)\end{aligned}$$

Vertexes of the absorbers A, B and C in the closed channel (ix,iy)

Absorber A:

$$a_1^{--} = A1 \begin{pmatrix} \sin(\alpha_{ix}^{-})\cos(\alpha_{iy}^{-}) \\ \sin(\alpha_{iy}^{-}) \\ \cos(\alpha_{ix}^{-})\cos(\alpha_{iy}^{-}) \end{pmatrix} \quad a_1^{o-} = A1 \begin{pmatrix} \sin(\alpha_{ix}^{o})\cos(\alpha_{iy}^{-}) \\ \sin(\alpha_{iy}^{-}) \\ \cos(\alpha_{ix}^{o})\cos(\alpha_{iy}^{-}) \end{pmatrix} \quad a_1^{-+} = A1 \begin{pmatrix} \sin(\alpha_{ix}^{-})\cos(\alpha_{iy}^{+}) \\ \sin(\alpha_{iy}^{+}) \\ \cos(\alpha_{ix}^{-})\cos(\alpha_{iy}^{+}) \end{pmatrix} \quad a_1^{o+} = A1 \begin{pmatrix} \sin(\alpha_{ix}^{o})\cos(\alpha_{iy}^{+}) \\ \sin(\alpha_{iy}^{+}) \\ \cos(\alpha_{ix}^{o})\cos(\alpha_{iy}^{+}) \end{pmatrix} \tag{2.20}$$

$$a_2^{--} = A2 \begin{pmatrix} \sin(\alpha_{ix}^{-})\cos(\alpha_{iy}^{-}) \\ \sin(\alpha_{iy}^{-}) \\ \cos(\alpha_{ix}^{-})\cos(\alpha_{iy}^{-}) \end{pmatrix} \quad a_2^{o-} = A2 \begin{pmatrix} \sin(\alpha_{ix}^{o})\cos(\alpha_{iy}^{-}) \\ \sin(\alpha_{iy}^{-}) \\ \cos(\alpha_{ix}^{o})\cos(\alpha_{iy}^{-}) \end{pmatrix} \quad a_2^{-+} = A2 \begin{pmatrix} \sin(\alpha_{ix}^{-})\cos(\alpha_{iy}^{+}) \\ \sin(\alpha_{iy}^{+}) \\ \cos(\alpha_{ix}^{-})\cos(\alpha_{iy}^{+}) \end{pmatrix} \quad a_2^{o+} = A2 \begin{pmatrix} \sin(\alpha_{ix}^{o})\cos(\alpha_{iy}^{+}) \\ \sin(\alpha_{iy}^{+}) \\ \cos(\alpha_{ix}^{o})\cos(\alpha_{iy}^{+}) \end{pmatrix} \tag{2.21}$$

Absorber B:

$$b_1^{o-} = B1 \begin{pmatrix} \sin(\alpha_{ix}^{o})\cos(\alpha_{iy}^{-}) \\ \sin(\alpha_{iy}^{-}) \\ \cos(\alpha_{ix}^{o})\cos(\alpha_{iy}^{-}) \end{pmatrix} \quad b_1^{+-} = B1 \begin{pmatrix} \sin(\alpha_{ix}^{+})\cos(\alpha_{iy}^{-}) \\ \sin(\alpha_{iy}^{-}) \\ \cos(\alpha_{ix}^{+})\cos(\alpha_{iy}^{-}) \end{pmatrix} \quad b_1^{o+} = B1 \begin{pmatrix} \sin(\alpha_{ix}^{o})\cos(\alpha_{iy}^{+}) \\ \sin(\alpha_{iy}^{+}) \\ \cos(\alpha_{ix}^{o})\cos(\alpha_{iy}^{+}) \end{pmatrix} \quad b_1^{++} = B1 \begin{pmatrix} \sin(\alpha_{ix}^{+})\cos(\alpha_{iy}^{+}) \\ \sin(\alpha_{iy}^{+}) \\ \cos(\alpha_{ix}^{+})\cos(\alpha_{iy}^{+}) \end{pmatrix} \tag{2.22}$$

$$b_2^{o-} = B2 \begin{pmatrix} \sin(\alpha_{ix}^{o})\cos(\alpha_{iy}^{-}) \\ \sin(\alpha_{iy}^{-}) \\ \cos(\alpha_{ix}^{o})\cos(\alpha_{iy}^{-}) \end{pmatrix} \quad b_2^{+-} = B2 \begin{pmatrix} \sin(\alpha_{ix}^{+})\cos(\alpha_{iy}^{-}) \\ \sin(\alpha_{iy}^{-}) \\ \cos(\alpha_{ix}^{+})\cos(\alpha_{iy}^{-}) \end{pmatrix} \quad b_2^{o+} = B2 \begin{pmatrix} \sin(\alpha_{ix}^{o})\cos(\alpha_{iy}^{+}) \\ \sin(\alpha_{iy}^{+}) \\ \cos(\alpha_{ix}^{o})\cos(\alpha_{iy}^{+}) \end{pmatrix} \quad b_2^{++} = B2 \begin{pmatrix} \sin(\alpha_{ix}^{+})\cos(\alpha_{iy}^{+}) \\ \sin(\alpha_{iy}^{+}) \\ \cos(\alpha_{ix}^{+})\cos(\alpha_{iy}^{+}) \end{pmatrix} \tag{2.23}$$

Absorber C:

$$c_1^{--} = C1 \begin{pmatrix} \sin(\alpha_{ix}^{-})\cos(\alpha_{iy}^{-}) \\ \sin(\alpha_{iy}^{-}) \\ \cos(\alpha_{ix}^{-})\cos(\alpha_{iy}^{-}) \end{pmatrix} \quad c_1^{o-} = C1 \begin{pmatrix} \sin(\alpha_{ix}^{o})\cos(\alpha_{iy}^{-}) \\ \sin(\alpha_{iy}^{-}) \\ \cos(\alpha_{ix}^{o})\cos(\alpha_{iy}^{-}) \end{pmatrix} \quad c_1^{-+} = C1 \begin{pmatrix} \sin(\alpha_{ix}^{-})\cos(\alpha_{iy}^{+}) \\ \sin(\alpha_{iy}^{+}) \\ \cos(\alpha_{ix}^{-})\cos(\alpha_{iy}^{+}) \end{pmatrix} \quad c_1^{o+} = C1 \begin{pmatrix} \sin(\alpha_{ix}^{o})\cos(\alpha_{iy}^{+}) \\ \sin(\alpha_{iy}^{+}) \\ \cos(\alpha_{ix}^{o})\cos(\alpha_{iy}^{+}) \end{pmatrix} \tag{2.24}$$

$$c_2^{--} = C2 \begin{pmatrix} \sin(\alpha_{ix}^{-})\cos(\alpha_{iy}^{-}) \\ \sin(\alpha_{iy}^{-}) \\ \cos(\alpha_{ix}^{-})\cos(\alpha_{iy}^{-}) \end{pmatrix} \quad c_2^{o-} = C2 \begin{pmatrix} \sin(\alpha_{ix}^{o})\cos(\alpha_{iy}^{-}) \\ \sin(\alpha_{iy}^{-}) \\ \cos(\alpha_{ix}^{o})\cos(\alpha_{iy}^{-}) \end{pmatrix} \quad c_2^{-+} = C2 \begin{pmatrix} \sin(\alpha_{ix}^{-})\cos(\alpha_{iy}^{+}) \\ \sin(\alpha_{iy}^{+}) \\ \cos(\alpha_{ix}^{-})\cos(\alpha_{iy}^{+}) \end{pmatrix} \quad c_2^{o+} = C2 \begin{pmatrix} \sin(\alpha_{ix}^{o})\cos(\alpha_{iy}^{+}) \\ \sin(\alpha_{iy}^{+}) \\ \cos(\alpha_{ix}^{o})\cos(\alpha_{iy}^{+}) \end{pmatrix} \tag{2.25}$$

2.B.2 Theoretical projection onto the isocentric plane

The theoretical projection of a channel opening onto the isocentric plane can be computed in two steps: First, the vertexes of the channel opening at radius C2, where the radiation exits the channel, are assessed. Secondly, a projection of the vertexes onto the isocentric plane is calculated.

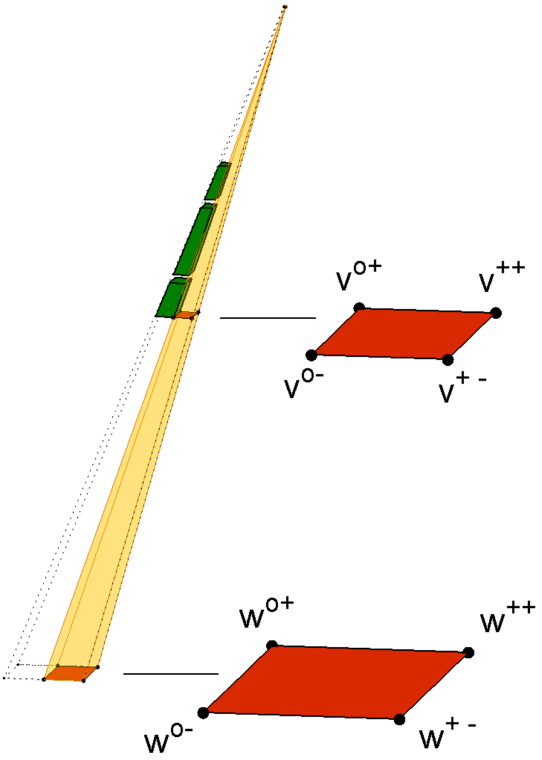

Figure 2.19: Vertexes of the channel opening at the lower edge of the collimator and of the projection of the opening onto the isocentric line.

The vertexes of the opening at C2 as well as those of its theoretical projection onto the isocentric plane are defined in figure 2.19. The vertixes are similar to those of absorber B in figure 2.18 but at radius C2. Together with equations 2.10 to 2.18, the equations for the vertexes of the opening of channel $(ix{,}iy)$ at radius C2 are given by:

$$
\begin{aligned}
v^{o-} &= C2 \begin{pmatrix} \sin(\alpha^{o}_{ix})\cos(\alpha^{-}_{iy}) \\ \sin(\alpha^{-}_{iy}) \\ \cos(\alpha^{o}_{ix})\cos(\alpha^{-}_{iy}) \end{pmatrix} &
v^{+-} &= C2 \begin{pmatrix} \sin(\alpha^{+}_{ix})\cos(\alpha^{-}_{iy}) \\ \sin(\alpha^{-}_{iy}) \\ \cos(\alpha^{+}_{ix})\cos(\alpha^{-}_{iy}) \end{pmatrix} \\
v^{o+} &= C2 \begin{pmatrix} \sin(\alpha^{o}_{ix})\cos(\alpha^{+}_{iy}) \\ \sin(\alpha^{+}_{iy}) \\ \cos(\alpha^{o}_{ix})\cos(\alpha^{+}_{iy}) \end{pmatrix} &
v^{++} &= C2 \begin{pmatrix} \sin(\alpha^{+}_{ix})\cos(\alpha^{+}_{iy}) \\ \sin(\alpha^{+}_{iy}) \\ \cos(\alpha^{+}_{ix})\cos(\alpha^{+}_{iy}) \end{pmatrix}
\end{aligned} \tag{2.26}
$$

The vertexes of the projection of the opening onto the isocentric plane can then be obtained using the intercept theorem. For the first vertex we can calculate:

$$
w^{o-} = \frac{SAD}{v^{o-}_{(z)}} \cdot v^{o-} = \frac{SAD}{\cos(\alpha^{o}_{ix})\cos(\alpha^{-}_{iy})} \cdot \begin{pmatrix} \sin(\alpha^{o}_{ix})\cos(\alpha^{-}_{iy}) \\ \sin(\alpha^{-}_{iy}) \\ \cos(\alpha^{o}_{ix})\cos(\alpha^{-}_{iy}) \end{pmatrix} = SAD \cdot \begin{pmatrix} \tan(\alpha^{o}_{ix}) \\ \tan(\alpha^{-}_{iy})/\cos(\alpha^{o}_{ix}) \\ 1 \end{pmatrix}
$$

with SAD = 800 mm and with the z-coordinate $v^{o-}_{(z)}$ of vertex v^{o-}. For the collimator presented in this work, the rotation angles are all below 11° and the division by the cosine is unproblematic.

Here are the final equations for all four vertexes:

$$
\begin{aligned}
w^{o-} &= SAD \cdot \begin{pmatrix} \tan\left(\alpha^{o}_{ix}\right) \\ \tan\left(\alpha^{-}_{iy}\right) / \cos\left(\alpha^{o}_{ix}\right) \\ 1 \end{pmatrix} &\qquad w^{+-} &= SAD \cdot \begin{pmatrix} \tan\left(\alpha^{+}_{ix}\right) \\ \tan\left(\alpha^{-}_{iy}\right) / \cos\left(\alpha^{+}_{ix}\right) \\ 1 \end{pmatrix} \\
w^{o+} &= SAD \cdot \begin{pmatrix} \tan\left(\alpha^{o}_{ix}\right) \\ \tan\left(\alpha^{+}_{iy}\right) / \cos\left(\alpha^{o}_{ix}\right) \\ 1 \end{pmatrix} &\qquad w^{++} &= SAD \cdot \begin{pmatrix} \tan\left(\alpha^{+}_{ix}\right) \\ \tan\left(\alpha^{+}_{iy}\right) / \cos\left(\alpha^{+}_{ix}\right) \\ 1 \end{pmatrix}
\end{aligned}
\tag{2.27}
$$

The theoretical width of the beam spots and the deviation maps presented in section 2.B.2 were assessed using these equations.

The projection to any plane downstream the collimator and parallel to the isocentric plane can be assessed, if SAD is replaced by the distance of the respective plane to the source along the central axis (Z'-axis in figure 2.17(b)).

2.B.3 2D-bMLC design variations

2.B.3.1 2D-bMLC pattern

In the 2D-bMLC model presented in 2.3.1, the channels arranged side by side in the 2D matrix have all the same alignment concerning the position of the fixed absorber modules. In principle, the mirrored alignment could also be an option. In figure 2.20 the two possible alignments are shown in a channel's cross section in the x-z-plane. If a channel is open, all three blocks are on the same side: on one side for alignment ▶ and on the other side for alignment ◀.

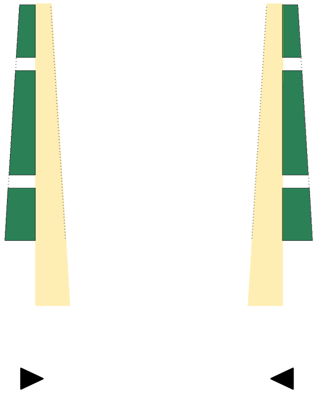

Figure 2.20: The two possible alignments of a 2D-bMLC channel labelled ▶ and ◀ respectively. The cross section of a channel in the x-z-plane is shown (see also figure 2.1 and 2.18).

Variations of our 2D-bMLC pattern with equally aligned channels are imaginable. In figure 2.21(b) and 2.21(c) we propose two possible variations of the pattern, which could also be used in rotational treatments, as they are described in chapter 3. The channel alignment is only shown for one row of elements (see section 2.3.2 for the definition of rows and columns). We assume that all channels of one column are of same alignment. Different channel alignments in one column would not make sense for our treatment concept with only one gantry rotation and fixed collimator angle. The channel openings of one column all abut in our design. A varied alignment of the channels would basically make no difference for the treatments, except a further reduction of primary radiation efficiency and the introduction of additional tongue-and-groove effects, where neighbouring channels would not abut.

Finally, we have chosen the pattern with identically aligned channels, because larger gaps between the channel beams should be avoided, and because it is the most regular pattern. We suppose that a regular design is easier to establish in practise.

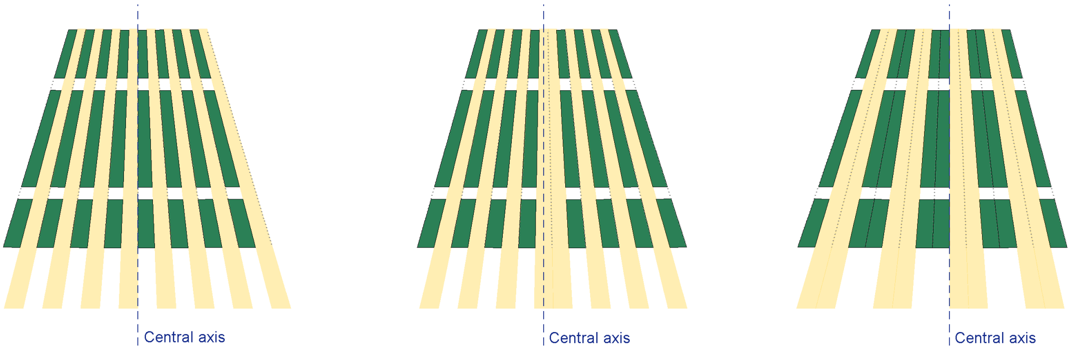

(a) ··· ▶▶▶▶▶▶▶▶ ··· (b) ··· ▶▶▶▶◀◀◀◀ ··· (c) ··· ▶◀▶◀▶◀▶◀ ···

Figure 2.21: (a) Pattern of channel openings of the presented 2D-bMLC model. (b & c) two alternative designs. See figure 2.20 for the definition of the channel alignments ▶ and ◀.

2.B.3.2 Collimator tilts

Another feature that could be implemented in a treatment machine equipped with a 2D-bMLC is a small tilt of the collimator as illustrated in figure 2.22. The tilt corresponds to a rotation of the collimator around the fixed photon source, so that all the absorber channels are still full focusing. As a consequence of a tilt, the 2D-bMLC beams are quasi shifted laterally.

In principle, tilts around both axes, the x- and y-axis in figure 2.5(b), are possible. In figure 2.23, we illustrate two useful shifts around the y-axis. In figure 2.23(a), our untilted 2D-bMLC design is shown. The beam of the most central channel just passes the central axis of the machine. A tilt of half the base angle α_b given in equation 2.13 would assure, that the beam centres the central axis (figure 2.23(b)). A tilt of full α_b would allow for a shift of the striped 2D-bMLC field, so that field stripes and gaps would quasi be exchanged 2.23(c).

Although we did not include collimator tilts in our treatment strategy presented in chapter 3, they could become especially useful in treatments with several rotations. For example, two rotations could be performed with different collimator tilts subsequently. In the study presented in chapter 5.2 a tilt angle of $-\frac{\alpha_b}{2}$ was used for the calculation of the primary radiation efficiency of the 2D-bMLC.

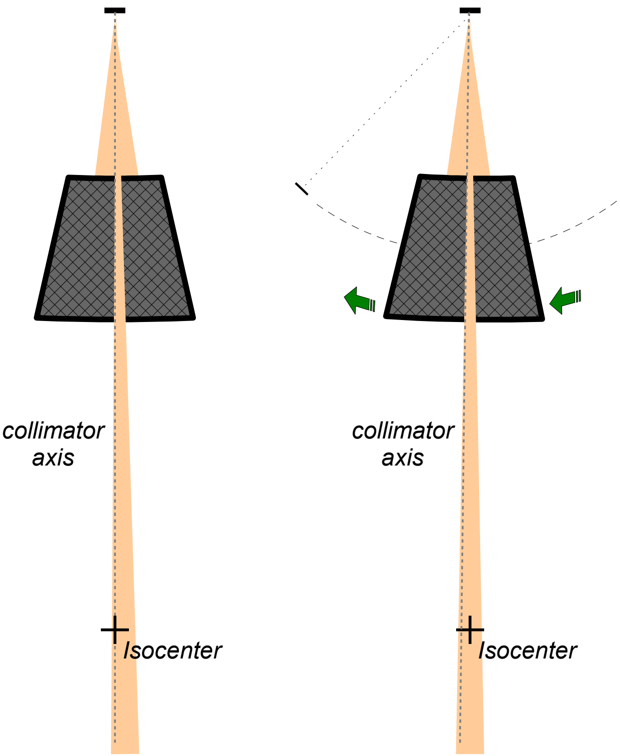

Figure 2.22: Tilt of the collimator around the linac source. The channels remain full focusing. Tilts around both the x- and y-axis in figure 2.5(b) are possible.

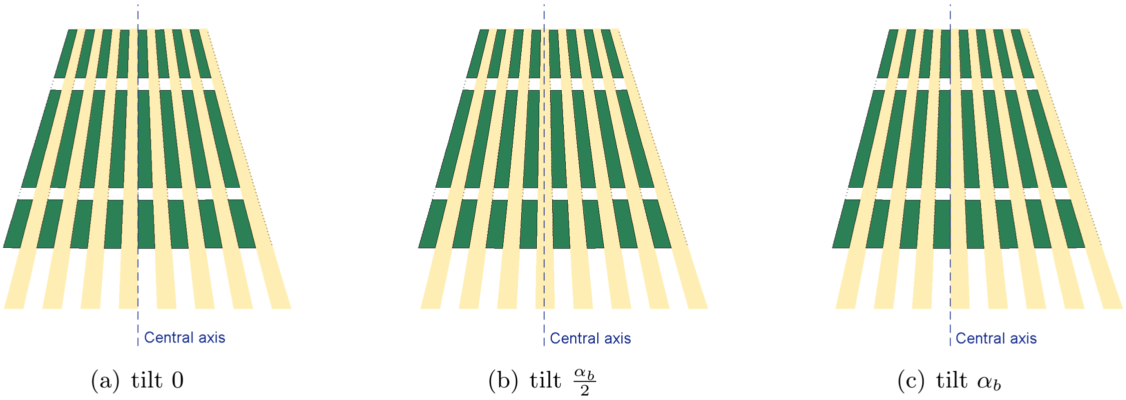

(a) tilt 0 (b) tilt $\frac{\alpha_b}{2}$ (c) tilt α_b

Figure 2.23: Different tilts of the 2D-bMLC around the y-axis in figure 2.5(b). The tilts are specified as fractions of the base angle α_b given in equation 2.13, which spans half a collimator channel. The tilt angle of 0 corresponds to our design as presented in 2.3.1.

Chapter 3

Treatment Planning for Fast Rotational IMRT with the 2D-bMLC

3.1 Overview

We developed a treatment planning system (TPS) for rotational 2D-bMLC treatments with a flattening filter free medical linac, a new optimization method and a Monte Carlo framework for exact calculation of the dose (sections 3.3.2–3.3.3).

A planning comparison was performed for five different clinical indications. The methods of the planning study are described in section 3.3.4, the results are presented in 3.4. With a maximum dose rate of 2000 MU/min delivery times of the 2D-bMLC treatments were estimated between 20 and 25 s. For two cases, additional plans were calculated for a max dose rate of 4000 MU/min and delivery times of 10 and 11 s. Clinically approved dose distribution of a Tomotherapy system were used as Gold Standard. The 2D-bMLC plans fulfilled the clinical goals. Dosimetric parameters were comparable to those of the Tomotherapy plans. The results of the study showed that the 2D-bMLC concept is in principal adequate for rotational radiotherapy treatments with potential delivery times considerably below those of IMRT techniques applied in the clinics today.

Publication

Parts of this chapter have been presented at international conferences, at the *2nd ESTRO Forum* in Geneva, Switzerland, April 2013 (Altenstein et al., 2013a) and at the *AAPM 55th Annual Meeting* in Indianapolis, USA, August 2013 (Altenstein et al., 2013b).

3.2 Introduction

As discussed in detail in chapter 2, the 2D-bMLC radiation fields are characterised by a striped pattern. The spatial fractionation into stripes renders the concept impractical for treatments with only a few beam directions. Dose distributions in the patient would be highly inhomogeneous. However, in rotational treatments limitations due to the field fractionation could eventually be overcome.

The planning framework is composed of two independent tools, a treatment planning system (TPS) for inverse plan optimisation and a tool for plan re-computation with a time-dependent

MC method. The TPS uses a pencil-beam (PB) dose algorithm and the gantry rotation is approximated by fixed beam directions. In contrast, the time-dependent MC simulations include a realistic model of the collimator absorber and gantry dynamic. Also, leakage dose and tongue-and-groove effects are modelled in a more appropriate way. (Shin et al., 2012) proposed a very efficient 'time feature' method for the handling of time-dependent quantities in MC simulations of radiotherapy applications. The method was applied to the 2D-bMLC treatments and implemented in the MC tool.

Typical delivery times for IMRT fractions are today in the range of several minutes. For many cases delivery times of the newer intensity-modulated arc therapy techniques (Otto, 2008b; Ulrich et al., 2007b; Wang et al., 2008; Yu, 1995) are below those of conventional fixed-gantry IMRT (Holt et al., 2013; Van Gestel et al., 2013). Delivery times could potentially be reduced with the FFF mode of medical linacs, which is characterised by significantly increased dose rates. (Georg et al., 2011; Mancosu et al., 2012; Salter et al., 2011; Spruijt et al., 2013). With the possibility to perform very quick 2D aperture changes, the 2D-bMLC should bring new ability to make use of high dose rate beams. In this study, we want to give an estimate of the minimum time needed for the delivery of an acceptable 2D-bMLC plan.

For the retrospective planning comparison, clinically approved dose distribution of a Tomotherapy system were used as Gold Standard. The capabilities of the Tomotherapy system to shape conformal dose distribution has been shown for various oncological situations, including the most challenging cases in terms of size, complex geometry and sparing of organs at risk (Fiorino et al., 2006; Peñgarícano et al., 2005; Sterzing et al., 2008a,b, 2009, 2010a; Wong et al., 2006). Five different clinical indications were selected for the plan comparison, covering a wide variety of target sizes and general planning complexity.

3.3 Methods

3.3.1 Models of the 2D-bMLC and the treatment machine

Within the Treatment planning system (TPS) and the 4D Monte Carlo tool, we modelled a treatment machine, which was similar to that described in section 2.3.3.1. Here, we review shortly the general specifications of the machine: A flattening-filter-free (FFF) 7MV linac source was modelled within the treatment machine. The source-axis distance was set to 800 mm. The modelled 2D-bMLC consisted of 30 by 30 absorber channels, resulting in a maximum field size of 300 by 300 mm^2 in the isocentric plan. The side lengths of the quasi-rectangular beams exiting a 2D-bMLC channel are approximately 5 mm and 10 mm in the isocentric plane. Between the source and the collimator, the radiation can be pre-collimated to rectangular fields of adjustable side lengths.

In figure 3.1, an exemplary 2D-bMLC field is shown to illustrate the characteristics of the radiation fields delivered with the modelled treatment machine. The fields are characterised by a striped pattern. However, the concept allows independent control of each channel. Apart from the time needed to open or close the channels, no leaf constraints restrict the choice of apertures.

Some new features were added to the treatment machine model in order to adapt it to rotational IMRT treatments. The source, the pre-collimator and the 2D-bMLC form together the gantry, which can rotate around the isocenter (see figure 3.2). The direction of movement is thereby perpendicular to the characteristic stripes of the radiation fields. At any gantry angle, the central ray of the radiation is pointing to the isocenter. The dose rate of the machine is tunable between a minimum and a maximum value defined in the planning process described below in

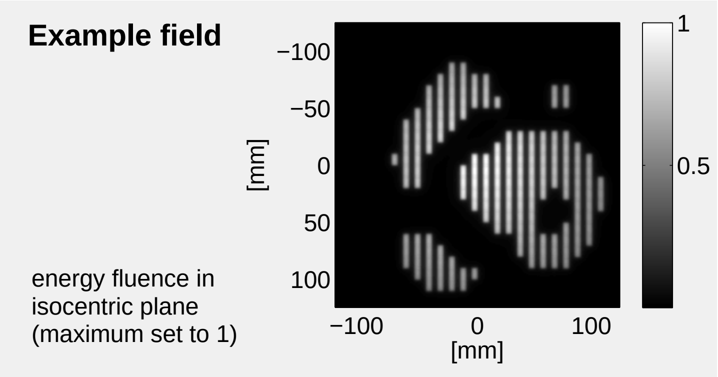

Figure 3.1: The 2D-bMLC fields are characterised by a striped pattern. Therefor, the concept allows independent control of each channel.

section 3.3.2. No constraints are considered for the speed of dose rate changes, i.e. the dose rate can be changed instantaneously between two values within the given range.

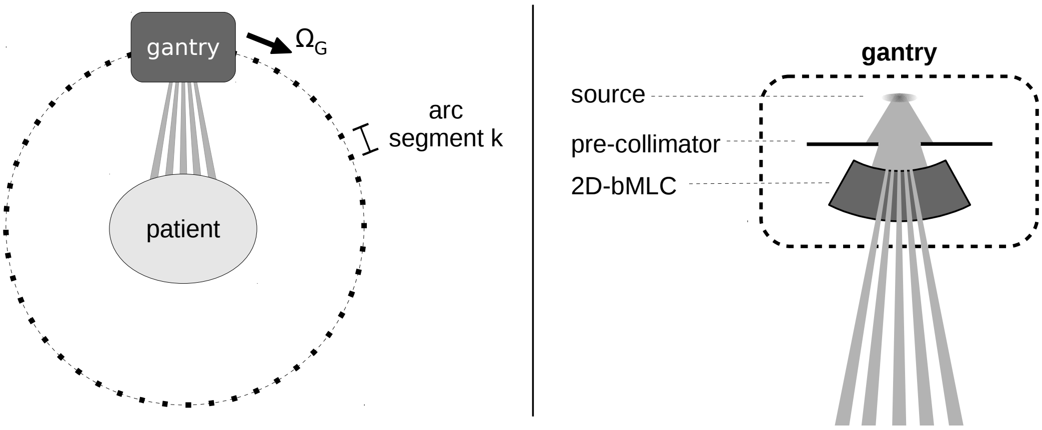

Figure 3.2: Setup for rotational 2D-bMLC treatments. The virtual linac source, the pre-collimator and the 2D-bMLC form together the gantry, which rotates around the isocenter. For treatment planning the gantry rotation is divided into arc segments of equal size with respect to gantry angle.

3.3.2 Treatment planning system (TPS)

3.3.2.1 2D-bMLC treatments and their parameters

A 2D-bMLC treatment fraction is delivered with constant gantry speed within one gantry rotation. The TPS calculates a plan for a user specified fractional treatment time $\mathrm{T_F}$. The rotation has to be finished within this time, and the angular speed of the gantry is given by

$$\dot{\Omega}_G = \frac{2\pi}{T_F} \quad . \tag{3.1}$$

The full rotation is subdivided into $\mathrm{N_{seg}}$ segments of equal size with respect to gantry angle. In the current version three options are available for $\mathrm{N_{seg}}$: 48, 72 or 96. The subdivision of the rotation into arc segments is illustrated in figure 3.2. We denote the set of segments by K and the set of 2D-bMLC channels by J. Further, τ_{jk} is the opening time of bixel jk, which refers to channel j∈J in segment k∈K. τ_{jk} is constrained as follows:

$$\tau_{jk} = 0 \qquad or \qquad \tau_{min} \leq \tau_{jk} \leq \tau_{max} \quad . \tag{3.2}$$

Times between 0 and τ_{min} would not be practical, because a certain time is needed for the mechanics to open and close a channel. The maximum opening time per segment τ_{max} is given by

$$\tau_{max} = \frac{T_F}{N_{seg}} \quad . \tag{3.3}$$

With $\tau_{max} \geq \tau_{min}$ and equation 3.3, we establish the following constraint for $\mathrm{T_F}$:

$$T_F \geq N_{seg} \cdot \tau_{min} \tag{3.4}$$

A dose rate $\dot{D}_k$ is assigned to each segment k. $\dot{D}_k$ is limited by the machine specific minimum dose rate $\dot{D}_{\mathrm{min}}$ and maximum dose rate $\dot{D}_{\mathrm{max}}$:

$$\dot{D}_{min} \leq \dot{D}_k \leq \dot{D}_{max} \tag{3.5}$$

with

$$0 \leq \dot{D}_{min} \leq \dot{D}_{max} \ . \tag{3.6}$$

3.3.2.2 Dose calculation

The patient geometry is discretised into a set of voxels I. The dose deposition coefficient D_{ijk} gives the dose deposited in voxel $i \in I$ by unit intensity of bixel jk. We define the intensity of bixel jk as the the product of opening time τ_{jk} and dose rate $\dot{D}_k$. The total dose in voxel i, denoted as d_i, can then be expressed by

$$d_i = \sum_{k \in K} \sum_{j \in J} D_{ijk} \tau_{jk} \dot{D}_k \quad . \tag{3.7}$$

The coefficients D_{ijk} are calculated with the treatment planning tool KonRadXP (Nill, 2001), which uses a pencil beam dose calculation algorithm and a macro pencil beam based on Monte Carlo calculated input data (more details are given in section 3.A). The arc segments were approximated by fixed beam directions, centrally aligned with the respective segments.

3.3.2.3 Objective function

Within the TPS, a standard least square objective function was used (Bortfeld et al., 1990; Holmes et al., 1991). The voxels $i \in I$ are unequivocally assigned to volumes of interest (VOIs), either to target volumes or to organs at risk (OARs). Let V be a set of VOIs and I_v be the set of voxels in volume $v \in V$. Each target volume is contained once in V. OARs can be represented manifold, each instance treated as an independent VOI. In doing so, the user can specify several (soft) dose constraints for an OAR, e.g. one constraint to minimise the dose to the OAR in general and a second constraint to penalise hot spots. The objective function for volume v is defined as

$$F_v = \frac{1}{N_v} \cdot \sum_{i \in I_v} p_v^+ \cdot \left[d_i - D_v^+\right]_+^2 + p_v^- \cdot \left[D_v^- - d_i\right]_+^2 \tag{3.8}$$

with

$$[\cdot]_+ = \max\{0, \cdot\} \quad . \tag{3.9}$$

N_v is the number of voxels in set I_v. The user specifies the (soft) maximum and minimum dose constraints, D_v^+ and D_v^- respectively, for all VOIs $v \in V$. p_v^+ and p_v^- are the positive penalty values for overdosage and underdosage of VOI v respectively. By definition p_v^- is 0 for all OARs, because minimum dose constraints for OARs are in general not useful. The parameters D_v^+, D_v^-, p_v^+ and p_v^- have to be defined prior to plan optimisation.

The full objective function F is given by the sum over all F_v:

$$F = \sum_{v \in V} F_v \quad . \tag{3.10}$$

3.3.2.4 Optimisation framework

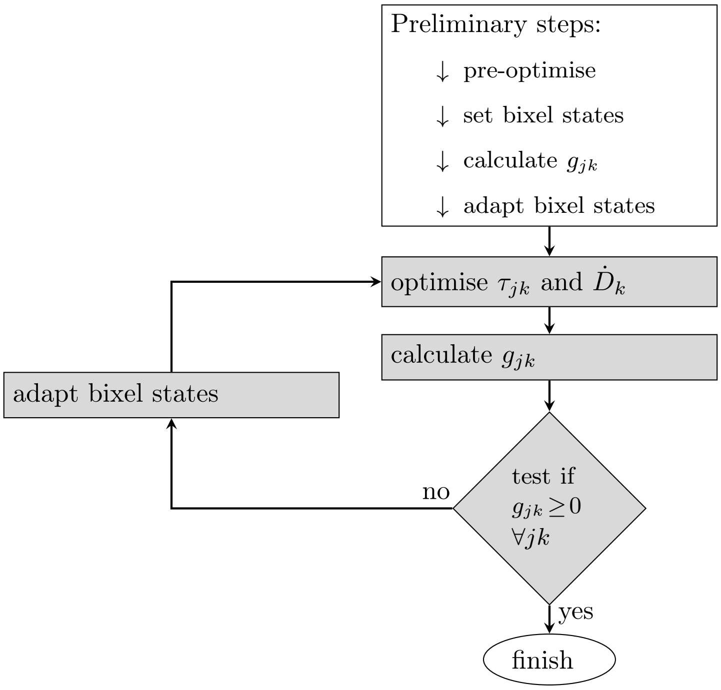

Figure 3.3: Scheme of the optimisation framework. The main optimisation loop is highlighted in grey. A detailed description of the different steps can be found in the text in section 3.3.2.4.

Dose rates $\dot{D}_k$ and channel opening times τ_{jk} are optimised inversely for a 2D-bMLC plan. The optimisation problem is formulated as follows:

$$\textit{minimise } F \quad \textit{subject to } 3.2 \textit{ and } 3.5 \tag{3.11}$$

The optimisation strategy, we use to solve this problem, is shown schematically in figure 3.3. Before going into details, we define the bixel states 'open' and 'closed'. If bixel jk is closed, τ_{jk} is 0, if it is open, τ_{jk} is between τ_{min} and τ_{max}. The following rule is defined to switch a bixel state:

Rule 1. *Bixel state switch: The bixel is set from its current state to the other, that is from open to closed or vice versa.* τ_{jk} *is set to 0 if bixel jk is closed; If its state is switched to open,* τ_{jk} *is set from 0 to* τ_{min}.

We define g_{jk} as the change in the objective function implicated by the state switch of bixel jk, while holding all other parameters fixed:

$$g_{jk} = F(bixel\ jk\ switched) - F \quad . \tag{3.12}$$

We call g_{jk} the price of the state switch of bixel jk. If a price g_{jk} is negative, the state switch of the respective bixel is beneficial in terms of decreasing the objective function F. We define a second rule to select, which bixels should be switched after calculation of g_{jk}. The idea is to pre-select all bixels with a negative price g_{jk}. We then start by switching the bixel, which brings the maximal benefit, hence the one with the lowest switch price (highest negative value). In general, a bixel state switch can change all g_{jk}. Therefore, before the switch of another bixel, the negativity of its switch prize has to be re-approved.

Rule 2. *Adapt bixel states: First, select the bixels with negative prices g_{jk}. Order the bixels according to the values of g_{jk}, starting with the smallest value (highest negativity). Then, loop over the pre-selected bixels following the established order. In each iteration of the loop, re-assess the respective switch price considering all state switches already performed. Switch the bixel state if its switch price remains negative.*

As shown in figure 3.3, the inverse optimisation of a 2D-bMLC treatment plan is composed of preliminary steps and the main optimisation loop.

Preliminary steps Before starting the main loop, the following modified problem is solved with a limited-memory algorithm for bound constrained optimisation (L-BFGS-B) (Byrd et al., 1995; Morales and Nocedal, 2011; Zhu et al., 1997):

$$minimise\ F \quad subject\ to \quad 0 \le \tau_{jk} \le \tau_{max}\ \ and\ \ \dot{D}_k = \dot{D}_{max} \tag{3.13}$$

The optimisation is terminated if changes of the objective function stay below a predefined value. Evaluating the final τ_{jk} of the preliminary optimisation, the bixel states are set as follows:

$$if \quad \tau_{jk} < \tau_{min}/2 \quad : \quad close\ bixel\ jk \tag{3.14}$$

$$if \quad \tau_{jk} \ge \tau_{min}/2 \quad : \quad open\ bixel\ jk \tag{3.15}$$

Subsequently, g_{jk} are calculated and the bixel states are adapted following rule 2.

Main optimisation loop The main optimisation loop is started right after the preliminary optimisation. The loop is divided into four steps:

1. Optimise the variables $\dot{D}_k$ and τ_{jk} with fixed bixel states. Therefore, minimise F subject to 3.5 and to

   $$\tau_{min} \le \tau_{jk} \le \tau_{max} \qquad for\ open\ bixels \tag{3.16}$$

   $$\tau_{jk} = 0 \qquad for\ closed\ bixels \tag{3.17}$$

   Again a L-BFGS-B algorithm is used.
2. Calculate g_{jk}.
3. Test if all g_{jk} are positive. If so, terminate the optimisation.
4. Adapt bixel states following rule 2.

The main loop is repeated until its termination in step 3.

3.3.3 4D Monte Carlo tool

3.3.3.1 Time feature formalism

For the time-dependant MC simulations, we make use of the Time Feature formalism, as it was presented by Shin et al. (2012) and by Perl et al. (2012). A function of time, called 'Time Feature', is associated to a simulation quantity, which varies over time. A Time Feature (TF) assigns a well-specified value to any specific time within the time range of the simulation.

In the Time Feature formalism, a time-dependant MC simulation - also called a 4D MC simulation - can run in two different modes: In the sequential mode, the time is sampled in regular, even intervals, from start time to end time, and one or more histories are simulated for each time step. In random mode, time values are sampled randomly between the start and the end time. For each history, a new random time is sampled. In both modes, TF values are computed, once a new time value has been sampled, and the corresponding time-dependant simulation quantities are updated. If necessary, also the simulation geometry has to be updated.

3.3.3.2 Implementation of the TF formalism

The 4D MC tool was implemented with Geant4.9.5 (Agostinelli et al., 2003). The 2D-bMLC therapy is simulated in random mode. In random mode geometry changes can occur after each simulated history. If the geometry updates are not performed efficiently, this can lead to exhaustively long computation times. Therefore, all moving objects have been implemented as so called parametrised volumes (Geant4 Collaboration, 2011). This volume class available in the Geant4 tool kit allows to define parametrisation functions, which calculate geometrical parameters of the respective volumes such as its position and rotation. There are different methods to implement movements in Geant4, but with parametrised volumes the geometry update during the simulation is managed very efficiently and fast.

Over the course of a 2D-bMLC treatment the dose rate can change multiple times. To account for these changes, we do not sample the time from an uniform distribution but from a probability density distribution $f(t)$, which corresponds to the dose rate over time normalised over the full treatment time.

The 4D MC tool can handle the following quantities as TFs: Channel openings, gantry angle, collimator angle, collimator tilts and target point coordinates. Actually, in the simulations performed for this study, only the gantry angle and the channel openings varied over time and were defined as TFs:

$\Omega_G(t)$: gantry angle

$O_j(t)$: relative opening of channel j (for all $j \in J$)

3.3.3.3 Conversion of a treatment plan into a set of TFs

The TPS calculates the dose rates $\dot{D}_k$ and the bixel opening times τ_{jk}. The conversion from these parameters to a deliverable MC plan, hence to a set of TFs Ω_G and O_j, is explained here. A MATLAB program has been written for the conversion.

As discussed in 3.3.2.1, the gantry speed is constant over the course of the 2D-bMLC treatment. With the angular speed of the gantry, given in 3.1, the TF of the gantry angle can be written as a linear function:

$$\Omega_G\,(t) = \dot{\Omega}_G\,t = \frac{2\pi}{T_F}t \tag{3.18}$$

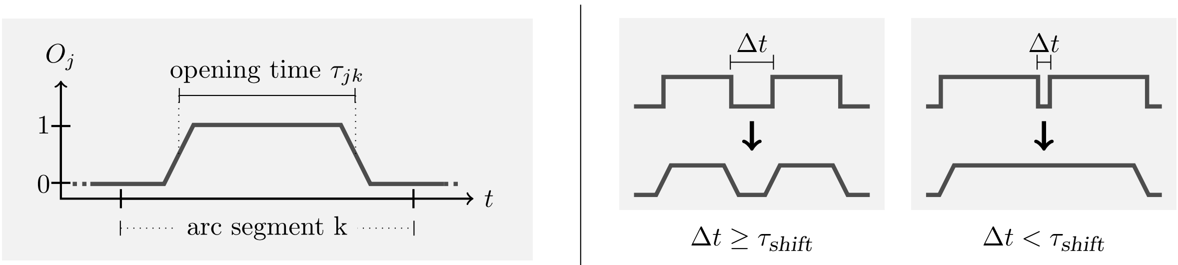

(a) $O_j(t)$ for arc segment k

(b) Rules for the processing of $O_j(t)$

Figure 3.4: The TF $O_j(t)$ describes the relative opening of channel j over time. (a) O_j is generated from the opening times τ_{jk} given by the TPS. Opening and closing of the channel is modelled with constant speed corresponding to linear ramps in O_j. (b) If the opening times of subsequent arc segments are together too long to allow closing and re-opening in between the two segments, the channel stays open.

As shown in figure 2.18, 2D-bMLC channels are opened and closed by the shift of a tungsten block between two positions. For further details we refer to section 2.3.1. In the 4D MC tool, the shift is modelled with constant speed. τ_{shift} is the time needed for the mechanical shift. For the plans presented in this paper, τ_{shift} was fixed to 100 ms.

TF $O_j(t)$ describes the relative opening of channel j. $O_j(t)$ can vary between 0 and one, whereas the values 0 and one correspond to a fully closed and a fully opened channel respectively. O_j is generated from the opening times τ_{jk} given by the TPS for all arc segments $k \in K$. If $\tau_{jk} = 0$, the channel does not open in arc segment k, and consequently O_j remains 0 while the gantry passes this segment. In figure 3.4(a), we show O_j for arc segment k if $\tau_{jk} \geq \tau_{min}$. Linear ramps describe the shift of the central block. The ramps can extend into neighbouring arc segments if τ_{jk} is close to τ_{max}. The time domain, where $O_j \neq 0$, is centred in the angular segment k.

In principal, a channel can open and close in all segments. But if the opening times of subsequent arc segments are together too long to allow the full mechanical shifts in between the two segments, the channel stays open. Figure 3.4(b) illustrates the corresponding rules for the processing of TF O_j.

3.3.3.4 Further details about the MC simulations

A Geant4 standard electromagnetic physics list with best advanced electromagnetic options was used[1].

The MC simulations are split up in two separate parts. In a first part the gantry rotation and the transport of the source photons through the collimator are simulated. All particles exiting the collimator are scored in a phase space file. This simulation is made time-dependant with the TF formalism as described above. In a second simulation the particle transport through the time-independent patient geometry is simulated, and the spatial dose deposition is scored. Thereby, each phase space particle of the first simulation, is reused 10 times, but each time with different random numbers. The patient geometry is modelled as a set of voxels of water with different electron densities (Ma and Li, 2011). The electron densities are acquired through conversion from the Hounsfield units (HU) of computed tomography (CT) scans. CT data sets are imported in DICOM format (Aso et al., 2007). The conversion follows a mapping based on phantom measurements. Below a cut-off value of -920 HU the voxels are modelled as air voxels.

---

[1] The physics list was similar to that which is loaded with the physics list constructor emstandard_opt3. The physics list constructors are developed and maintained by the electromagnetic working group of the Geant4 collaboration. Further information can be found on `http://geant4.web.cern.ch/geant4/collaboration/working_groups/electromagnetic/physlist.shtml`.

Table 3.1: Dose prescriptions and planning parameters for the studied cases. For cases 2 to 5, a multi-focal simultaneous integrated boost concept was applied. (The TPS parameter $\dot{D}_{\mathrm{min}}$ was fixed to 500 MU/min for all plans.)

Case	Dose prescription				TPS param.			MC param.
	PTV	volume [ml]	$D_{50\%}$ [Gy]	Fx	N_{seg}	$\dot{D}_{\mathrm{max}}$ [MU/min]	T_F [s]	pre-coll. field size [mm^2]
1. Prost. only	PT	74	80.0	40	48	2000	20, 40	160x160
					48	4000	10	
2. Prost. boost	boost PT	74	76.5	34	72	2000	20, 40	170x280
	LDP	1040	51.0	34	72	4000	11	
3. Oral cavity	boost PT	314	70.4	32	72	2000	25	300x240
	boost LN	18	70.4	32				
	LDP	1083	57.6	32				
4. Naso-pharynx	boost PT	220	70.4	32	72	2000	25	300x260
	boosts LN	231 & 101	70.4	32				
	LDP	1324	57.6	32				
5. Anal	boost PT	442	58.8	28	96	2000	25	310x310
	boosts LN	122 & 10	58.8	28				
	LDP	3329	50.4	28				

PTV: planning target volume, PT: primary tumour, LN: lymph node, LDP: Lymphatic drainage pathways, $D_{50\%}$: median dose, Fx: number of fractions

The resolution of the voxel grid, in which also the dose scoring is performed, corresponds to the pixel size and the slice thickness of the CT images respectively.

MC simulations were performed in multiple parallel jobs. As a measure for statistical uncertainty of the final MC dose distribution, the fractional uncertainty in the average dose for voxels with dose values greater than 50% of the maximum dose, $\overline{F}_{d>0.5d_{\mathrm{max}}}$, was calculated (Chetty et al., 2007). For all cases presented in this chapter, $\overline{F}_{d>0.5d_{\mathrm{max}}}$ was about 1%.

3.3.4 Plan comparison study

For four patients and five clinical indications, we performed a retrospective planning comparison using clinically approved dose distribution of a Tomotherapy system as Gold Standard.

Patients and radiotherapy planning Tumour sites were prostate (cases 1 and 2), oral cavity (3), nasopharynx (4) and anus (5). No modifications were made to the previously accepted delineation of the target volumes and organs at risk (OAR). Planning target volumes (PTV) and dose prescriptions are specified in the left column of table 3.1. In case 1, dose was prescribed to the primary tumour PTV. For cases 2 to 5, a multi-focal simultaneous integrated boost concept was applied, with boosts to the primary tumour and the involved lymph nodes (Sterzing et al., 2010b). Lower doses were prescribed to the lymphatic drainage pathways (LDP). Case 1 and 2 are prescription variants for the same prostate patient with different hypothetical tumour staging. Planning was based upon CT scans with pixel size 1.95 mm and slice distance 2 mm (cases 1 and 2) or 3 mm (cases 3-5).

Tomotherapy planning Tomotherapy (HT) planning was performed with the Tomotherapy planning station version 4.0. A field width of 2.5 cm in regular mode and a pitch of 0.43 was chosen. For more information about HT treatments and planning, we refer to (Jeraj et al., 2004; Mackie et al., 1999; Welsh et al., 2002).

2D-bMLC plans 2D-bMLC plans were optimised for a given set of TPS parameters $\mathrm{N_{seg}}$, $\dot{D}_{\max}$ and $\mathrm{T_F}$ (see section 3.3.2.1). The penalty values in equation 3.8 were manually adjusted to obtain the best plan. The best plan was defined as the plan, which fulfilled the clinical constraints for the PTVs and minimises the dose to the most critical OARs. The plans presented in this paper are summarised in the middle column of table 3.1. In the following, the plans are named by their $\mathrm{T_F}$ (e.g. plan 20s for case 1). For all cases, plans were generated for a a maximum machine dose rate $\dot{D}_{\max}$ of 2000 MU/min. In addition for case 1 and 2, plans were optimised for $\dot{D}_{\max} = 4000$ MU/min and reduced $\mathrm{T_F}$. (For case 1, the half $\mathrm{T_F}$ of plan 20s was used; for case 2, $\mathrm{T_F}$ was set to the smallest rounded number satisfying inequality 3.4.) For all plans, the minimum dose rate was fixed to 500 MU/min.

The plans were recomputed with the MC tool. In the MC simulations, the pre-collimator field (see figure 3.2) was adapted to enclose all channels, which open during the treatment, plus a margin of one channel width. In the last column of table 3.1, the dimensions of the pre-collimator fields in the isocentric plane are given. The MC calculated plans were finally rescaled, so that the median dose received by the primary tumour PTV matches the dose prescription.[2]

Plan evaluation For plan comparison cumulative dose-volume histograms (DVH) were calculated. Air voxels (HU value below −920) were not considered. For the volumes of interest (VOI), the near-minimum dose $\mathrm{D_{98\%}}$ and the near-maximum dose $\mathrm{D_{2\%}}$ were assessed (ICRU report 83). $\mathrm{D_{50\%}}$ is the median dose to a VOI; $\mathrm{V_{XGy}}$ is the percentage of a VOI receiving more than X Gy. PTV coverage was evaluated using $\mathrm{V_{95\%}}$, i.e. the relative fraction of the PTV covered by the 95% isodose. The uniformity index (UI) is calculated as the ratio between the dose received by 5% of the PTV and the dose received by 95% of the PTV ($UI = \mathrm{D_{5\%}}/\mathrm{D_{95\%}}$). The conformity index (CI) is defined as the ratio between the volume covered by the 95% isodose and the target volume covered by the 95% isodose ($\mathrm{CI} = \mathrm{V_{95\%}}/\mathrm{PTV_{95\%}}$) (Krause et al., 2012; Pirzkall et al., 2000; Sterzing et al., 2010b).

The normal tissue volume was defined as the patient body minus the target volumes. For DVH analysis, the normal tissue volume was restricted to the scanned region covering all target volumes ±5 cm.

3.4 Results

3.4.1 Comparison of TPS and MC calculated plans

In figure 3.6(a), we show DVHs for the plan with $\mathrm{T_F} = 25$ s for case 5 (anal cancer) as calculated by the TPS and by the MC tool. The dose distributions shown as colour maps in figure 3.5 are from the same plans. The comparison illustrates a general trend, that can also be reported for the other cases: The target dose uniformity is reduced in the MC calculated plans compared to the TPS plans. This results in less steeper DVHs for the PTVs. As can be seen in the tables 3.2 and 3.3, maximum doses $\mathrm{D_{2\%}}$ as well as the target dose uniformity indices (UI) are increased relatively by up to 3%. Furthermore, the minimum doses $\mathrm{D_{98\%}}$ are decreased by 1-2% in case 4 and 5. In the tables, we also see, that the mean dose to the normal tissue is increased in the

---

[2] In practise, a plan rescaling of several percent can be implemented as follows: To scale the planned doses down, the dose rates $\dot{D}_k$ are reduced uniformly by the respective factor. To scale the doses up, the channel opening times can be multiplied with the scaling factor. In general, this conditions a reduction of the gantry speed, and $\mathrm{T_F}$ is increased by the scaling factor.

MC calculations, by 0.5 Gy for case 1 and by about 1 Gy for case 2-5. No relevant differences in doses to the OARs can be reported.

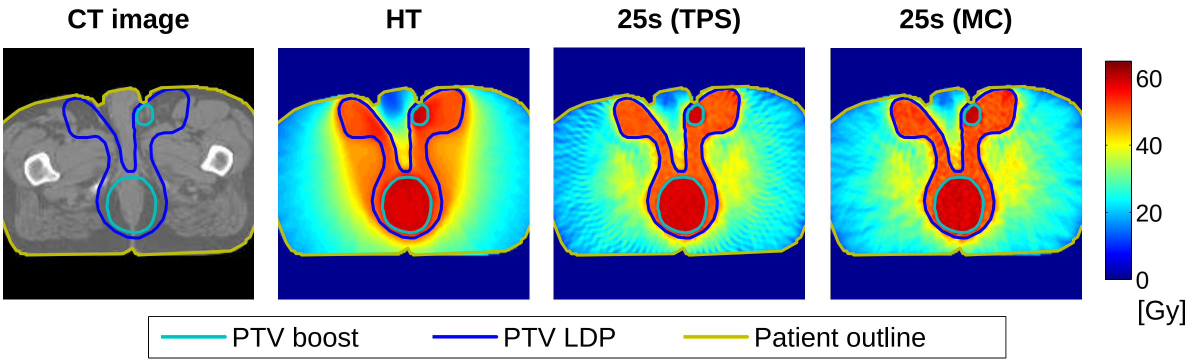

Figure 3.5: Case 5 (anal cancer): Dose colour maps for HT and 25s as calculated by the TPS and the MC tool.

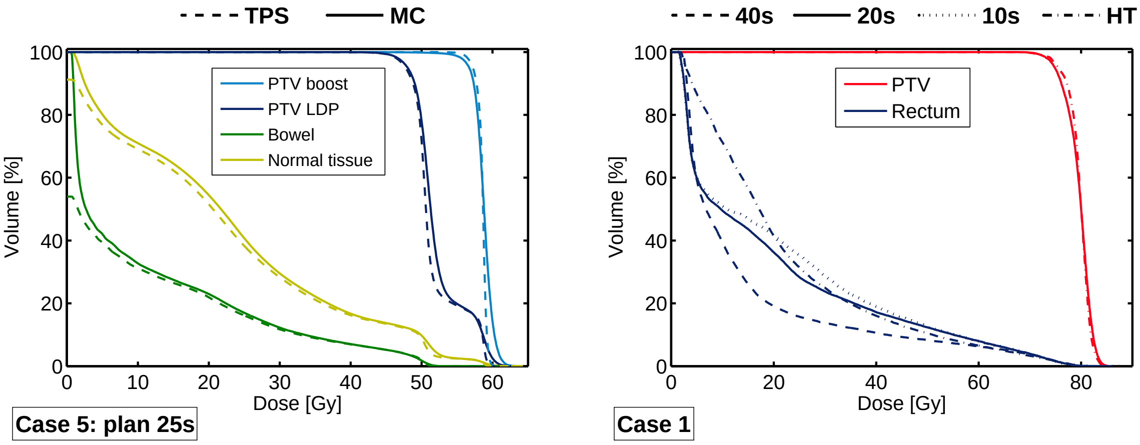

(a) Comparison of TPS and MC plan

(b) Comparison of different 2D-bMLC plans

Figure 3.6: (a) DVHs of 25s for case 5 as calculated by the TPS and the MC tool. (b) Case 1: DVHs for the MC calculated 2D-bMLC plans and for the HT reference plan. For the PTV, the 2D-bMLC plans have very similar DVHs and only 20s is shown in comparison to HT.

3.4.2 Comparison of 2D-bMLC plans with different T_F

In figure 3.6(b), DVHs for case 1 (prostate only) are shown. Comparing the plans optimised for a $\dot{D}_{\max} = 2000\,\mathrm{MU/min}$, it can be seen, that dose to the rectum is spared if T_F is increased from 20 to 40 s. However, concerning V_{50Gy} (8% for 40s, 12% for 20s) and V_{70Gy} (4% for both plans) the differences were seen as not clinically significant. The PTV coverage index $V_{95\%}$ is 0.92 for 40s and 0.91 for 20s. Table 3.2(a)) shows all DVH parameters calculated for plan 20s and 10s. For 10s, i.e. the plan calculated for $\dot{D}_{\max} = 4000\,\mathrm{MU/min}$, $V_{95\%}$ is 0.89 (TPS 0.91). Relative differences in $D_{2\%}$ and $D_{98\%}$ between the two plans are below 1%, and no differences can be observed concerning dose to the OARs and the normal tissue.

Very similar results can be reported for the 2D-bMLC plans calculated for case 2, in which an integrated boost concept was applied. Here, doses to rectum and bladder can be reduced by increasing T_F from 20 to 40 s, but again not in a clinically relevant amount. DVH parameters calculated for plan 20s and 11s are reported in table 3.2(b).

3.4.3 Comparison with HT

In table 3.2 and 3.3, DVH parameters of the 2D-bMLC plans and of the HT reference plans can be compared. Here, we want to summarise major differences, which are highlighted in the tables (relative differences are given in %): For case 1, The HT plan has better PTV coverage ($\Delta V_{95\%} = 2-6\%$). In case 2, Dose coverage of the boost PTVs is better for the 2D-bMLC plans ($\Delta V_{95\%} \sim 4\%$), whereas coverage of the LDP PTV is better for HT ($\Delta V_{95\%}$ $2-4\%$). In some cases, the minimum dose to the PTV was slightly higher with HT compared to the MC calculated 2D-bMLC plans: Maximum differences are observed in case 5 ($\Delta D_{98\%} = 1.2\,Gy$ for the boost PTVs) and in case 1 ($\Delta D_{98\%} = 1.3\,Gy$ between HT and 10s).

For all cases the 2D-bMLC plans have better target dose conformity, with notably large differences of about 20% for the PTV of case 1 and the LDP PTV of case 5 (see also colour maps in figure 3.5). In some cases, dose to the OARs could be decreased with the 2D-bMLC plans (e.g. bladder in case 1 and 2, parotid glands in case 3, femoral heads in case 5). However, the differences in dose to OARs were seen as clinically rather insignificant. In all cases, the mean dose to the normal tissue is reduced by more than 10% in the 2D-bMLC plans compared to HT (Maximum difference ~ 30% in case 1).

3.5 Discussion

2D-bMLC treatment planning

The TPS optimises directly a set of machine parameters, namely the channel opening times and the machine dose rate for each arc segment. The optimisation constraints ensure, that the final parameters are physically achievable. The proposed algorithm could therefore be classified as a direct aperture optimisation (DAO). Overall, the optimisation cannot directly be compared to DAO proposed for IMRT with a conventional MLC, because the two collimator concepts differ fundamentally (Hårdemark et al., 2003; Li et al., 2003; Otto, 2008b; Romeijn et al., 2005; Shepard et al., 2002). However, some principals were adopted, especially the concept to 'price' potential apertures and to make the prices the basis of decision for aperture selection. Of course, the character of an aperture is different in our case: Because of the individual control each 2D-bMLC channel can be seen as an aperture, and for one arc segment all 'channel apertures' can be selected independently. We use the pricing concept, for the iterative switching between the channel states *open* and *closed* (section 3.3.2.4).

In the TPS the arc segments are approximated by fixed beam directions and the channel dynamics are ignored. In contrast, the time-dependent MC simulations include a realistic model of the collimator absorber and gantry dynamic. The MC tool was primarily developed in order to study the influence of the dynamics onto the dose distributions. Furthermore, leakage dose and tongue-and-groove effects are modelled in a more realistic way than in the TPS. In order to avoid additional discrepancies in the dose distributions, the patient geometry is modelled in the MC simulations as a set of voxels of water with different electron densities. (Ma and Li, 2011) showed for fixed beam directions that, using water with different electron densities, MC calculated photon doses are very similar to those calculated with a pencil beam dose algorithm (PB). To make sure that our PB agrees with the MC calculations, we performed a systematic testing in water phantoms for different (time-independent) configurations. Therefore, the differences seen for the patient plans are real effects due to the added dynamics, leakage and or tongue-and-groove. (Altenstein et al., 2012b)

Table 3.2: Dose reports for cases 1 and 2. DVH parameters are defined in 3.3.4. 2D-bMLC plans are identified by their fractional treatment time $\mathrm{T_F}$. Parameters are given for these plans as calculated with the TPS (in black) and with the MC tool (in grey). Most critical OARs were included into the tables. Major differences between HT and 2D-bMLC plans are highlighted with boxes. Units: Doses are given in Gy, $\mathrm{V_{XGy}}$ in percent, $\mathrm{T_F}$ in s, $\dot{D}_{\mathrm{max}}$ in MU/min

(a) Case 1: Prostate ca.

	HT	**20s**	**10s**
$\mathrm{T_F}$	129	20	10
$\dot{D}_{\mathrm{max}}$	880	2000	4000
PTV			
$\mathrm{D_{98\%}}$	74.1	73.2 73.4	73.1 72.8
$\mathrm{D_{50\%}}$	80.0	79.5 80.0	79.5 80.0
$\mathrm{D_{2\%}}$	83.3	81.8 83.6	82.0 84.3
$\mathrm{V_{95\%}}$	94	92 91	91 89
UI	1.09	1.09 1.11	1.09 1.12
CI	1.25	1.07 1.08	1.06 1.08
Rectum			
$\mathrm{D_{2\%}}$	74.1	73.9 74.1	74.0 74.0
$\mathrm{V_{50Gy}}$	10	13 12	13 13
$\mathrm{V_{70Gy}}$	3	4 4	4 4
Bladder			
$\mathrm{D_{2\%}}$	81.8	80.3 81.0	80.3 81.1
$\mathrm{V_{50Gy}}$	35	21 21	21 21
$\mathrm{V_{70Gy}}$	17	12 12	12 12
Normal tissue			
$\mathrm{D_{mean}}$	4.5	2.6 3.1	2.6 3.1

(b) Case 2: Prostate ca. (boost concept)

	HT	**20s**	**11s**
$\mathrm{T_F}$	289	20	11
$\dot{D}_{\mathrm{max}}$	880	2000	4000
PTV boost			
$\mathrm{D_{98\%}}$	70.0	71.5 71.7	71.6 71.3
$\mathrm{D_{50\%}}$	76.5	76.3 76.5	76.2 76.5
$\mathrm{D_{2\%}}$	80.0	78.7 79.8	79.9 81.4
$\mathrm{V_{95\%}}$	0.91	0.95 0.95	0.96 0.94
UI	1.11	1.07 1.09	1.09 1.11
CI	1.08	1.05 1.07	1.06 1.08
PTV LDP			
$\mathrm{D_{98\%}}$	47.2	46.7 47.0	46.4 46.6
$\mathrm{D_{50\%}}$	50.7	50.9 51.2	51.0 51.3
$\mathrm{D_{2\%}}$	77.4	77.1 77.5	77.3 77.8
$\mathrm{V_{95\%}}$	0.97	0.95 0.95	0.94 0.93
UI	1.54	1.56 1.56	1.57 1.57
CI	1.20	1.13 1.15	1.13 1.16
Rectum			
$\mathrm{D_{2\%}}$	73.7	72.4 72.9	72.7 72.7
$\mathrm{V_{50Gy}}$	14	18 18	16 17
$\mathrm{V_{70Gy}}$	4	4 4	4 4
Bladder			
$\mathrm{D_{2\%}}$	77.7	77.8 77.9	78.1 78.4
$\mathrm{V_{50Gy}}$	40	26 26	26 25
$\mathrm{V_{70Gy}}$	14	13 14	13 13
Normal tissue			
$\mathrm{D_{mean}}$	13.1	10.4 11.3	10.3 11.3

Table 3.3: Dose reports for cases 3-5. See table 3.2 for explanations.

(a) Case 3: Oral cavity ca.

	HT	25s	
T_F	410	25	
$\dot{D}_{max}$	880	2000	
PTV boosts*			
$D_{98\%}$	66.2	65.6	65.5
$D_{50\%}$	70.1	70.1	70.4
$D_{2\%}$	73.0	71.9	73.8
$V_{95\%}$	0.96	0.95	0.95
UI	1.08	1.07	1.10
CI	1.10	1.03	1.063
PTV LDP			
$D_{98\%}$	53.9	53.8	53.6
$D_{50\%}$	58.8	58.3	59.3
$D_{2\%}$	72.3	71.4	73.0
$V_{95\%}$	0.97	0.97	0.96
UI	1.29	1.28	1.31
CI	1.29	1.19	1.213
Parotid glands*			
$D_{2\%}$	41.2	35.0	34.3
D_{mean}	17.8	12.9	13.5
Normal tissue			
D_{mean}	10.6	8.6	9.5

* Parameters are given for multiple volumes together.

(b) Case 4: Nasopharynx ca.

	HT	25s	
T_F	490	25	
$\dot{D}_{max}$	880	2000	
PTV boosts*			
$D_{98\%}$	66.9	66.6	66.0
$D_{50\%}$	70.2	70.3	70.4
$D_{2\%}$	72.4	72.1	73.6
$V_{95\%}$	0.98	0.98	0.96
UI	1.06	1.06	1.08
CI	1.12	1.07	1.08
PTV LDP			
$D_{98\%}$	55.8	55.5	54.7
$D_{50\%}$	64.1	62.3	62.1
$D_{2\%}$	72.0	71.7	73.0
$V_{95\%}$	0.99	99	98
UI	1.26	1.26	1.30
CI	1.33	1.21	1.21
Optic chiasm			
D_{max}	45.9	47.6	46.5
D_{mean}	40.2	34.0	32.9
Optic nerves*			
D_{max}	49.1	51.7	51.2
D_{mean}	25.7	17.6	18.3
Inner ears*			
$D_{2\%}$	53.3	55.5	56.7
Parotid glands*			
$D_{2\%}$	71.9	71.4	73.1
D_{mean}	33.1	33.6	34.1
Normal tissue			
D_{mean}	13.9	11.3	12.2

(c) Case 5: Anal ca.

	HT	25s	
T_F	551	25	
$\dot{D}_{max}$	880	2000	
PTV boosts*			
$D_{98\%}$	56.8	56.5	55.6
$D_{50\%}$	58.8	58.7	58.8
$D_{2\%}$	60.0	59.6	61.3
$V_{95\%}$	1.00	0.99	0.98
UI	1.04	1.04	1.07
CI	1.15	1.09	1.12
PTV LDP			
$D_{98\%}$	46.4	46.5	46.7
$D_{50\%}$	50.9	50.6	51.3
$D_{2\%}$	59.4	59.2	60.2
$V_{95\%}$	0.96	0.95	0.96
UI	1.21	1.23	1.24
CI	1.21	1.03	1.04
Bowel			
$D_{2\%}$	49.0	50.2	50.0
D_{mean}	11.2	9.8	10.9
Femoral heads*			
$D_{2\%}$	47.3	35.9	37.3
D_{mean}	34.0	23.7	24.8
Normal tissue			
D_{mean}	12.9	10.3	11.1

Plan comparison study

For the plan comparison study, plans were generated for many different fractional treatment times $\mathrm{T_F}$. For presentation in this paper, we selected for every case the plan with the minimum $\mathrm{T_F}$, which fulfilled the clinical goals (in addition $\mathrm{T_F} = 40\,\mathrm{s}$ for cases 1 and 2).

The presented TPS plans were approved by a radiation oncologist, and the approval was confirmed after MC re-computation. Overall, small differences between TPS and MC plans can be reported: The mean dose to the normal tissue is increased in the MC plans. This is because the leakage dose is underestimated with the TPS but modelled more appropriately in the MC simulations. Furthermore, the target dose inhomogeneity is increased with MC. However, relative difference in UI are below 3% (table 3.2 and 3.3). The opening shift of the absorber channels introduces an additional fluency modulation of the channel beams. This effect is not considered in the TPS calculation and is one reason for these differences. But finally, there is an interplay of several effects (gantry and absorber dynamics, leakage, tongue-and-groove), whose impacts on the dose distributions is hard to distinguish.

For case 1 and 2, the increase in fractional treatment time from 20 to 40 s resulted in better sparing of the rectum and the bladder, but the differences were seen as not clinically significant. Additional calculations showed that dose to the OARs could not noticeably be reduced by further increasing $\mathrm{T_F}$. In general, a longer $\mathrm{T_F}$ always leads to a better result by means of minimisation of the objective function given in equation 3.8, whereas above a certain $\mathrm{T_F}$, differences tend to be minor. (A more detailed study of the influence of $\mathrm{T_F}$ on the dose distributions is presented in section 4.3).

Shorter $\mathrm{T_F}$ are possible, if
Dmax is increased. However, a decrease in $\mathrm{T_F}$ implicates a reduced value domain of permitted opening times τ_{jk}. An increase of
Dmax and a decrease of $\mathrm{T_F}$ by the same factor should therefore implicate worse results by means of minimisation of the objective function. However, the plans 10s and 11s (4000 MU/min) calculated for case 1 and 2 respectively, were acceptable with only minor differences to the plans 20s (2000 MU/min).

In comparison to the HT reference plans, the 2D-bMLC showed comparable plan quality. The mean dose to the normal tissue could be reduced with the 2D-bMLC treatment plans. The differences are comparable to those observed between IMRT treatments and HT (Sterzing et al., 2008b). Dose to the normal tissue can be reduced in HT treatments if the dynamic jaw mode is used (Sterzing et al., 2010b). For our comparison study HT was planned with regular fixed jaw mode.

Hardware limitations

For the current planning study we based all hardware constraints, like gantry speed, channel opening times or dose rates on potentially realistic assumptions. Gantry speed and dose rates up to 2000 MU/min are currently already achieved in modern linear accelerators like HT or flattening filter free devices (Mackie et al., 1999; Salter et al., 2011). For the channel opening time new advanced drive concepts like piezo-electric motors need to be investigated. A detailed discussion on the possible mechanical realisation of the concept is outside the scope of this paper.

For this first study, 2D-bMLC plans were calculated for fixed collimator angle and couch position. The gantry speed was not changed during a treatment. Variations of these parameters could in principal be added to further improve the dose distributions. The 2D-bMLC treatments could also be extended to several gantry rotations, e.g. with multiple target points or helical delivery.

The special design of the 2D-bMLC is notably sensitive to geometrical misalignments of the absorber modules or of the collimator as a whole. MC calculations for static fields showed, that already very small rotational misalignments of the collimator can lead to significant decreases in the energy fluency of the fields (Altenstein et al., 2012c). As one of the next steps, we will investigate the influence of misalignments onto 2D-bMLC patient plans. Furthermore, we will also study, how intrafraction motion would affect the planned doses.

3.6 Conclusion

The 2D binary multileaf collimator is a novel collimator concept aiming at very quick aperture modulations. In order to test, if the 2D-bMLC concept is in principal adequate for radiotherapy treatments, a planning framework for rotational IMRT treatments with a 2D-bMLC was developed. A planning comparison was performed for 5 different clinical indications. The 2D-bMLC plans fulfilled the clinical goals, and dosimetric parameters were comparable to those of clinically approved Tomotherapy plans. With a FFF linac source and a maximum dose rate of 2000 MU/min, scheduled delivery times of the 2D-bMLC treatments were estimated between 20 and 25 s. With an even increased dose rate, potential delivery times down to 10 s become possible.

3.A Details: Finite Parallel Pencil Beam Model for the Treatment Planning Tool KonRadXP

3.A.1 Dose calculation engine of the treatment planning tool KonRadXP

The TPS for 2D-bMLC treatments, described in section 3.3.2, uses the treatment planning tool KonRadXP for calculation of the dose deposition coefficients $\mathrm{D_{ijk}}$. The coefficient $\mathrm{D_{ijk}}$ gives the dose deposited per unit intensity of bixel jk (channel j in arc segment k) to a voxel i of the patient geometry. Hence, before the TPS starts the plan optimisation, for every bixel jk the dose at any voxel i is calculated and stored in the matrix ($\mathrm{D_{ijk}}$).

KonRadXP was developed at the German Cancer Research Center and was originally presented by Nill (2001). A finite pencil beam (PB) dose calculation model is used for computation of the dose deposition matrix. The model relies on pre-calculated dose distributions: For a given source and a given bixel resolution, a 3D water-dose distribution of a finite parallel PB, i.e. a non-divergent PB, must be available. Any dose calculation method can be used to assess these PBs. The advantage of using a non-divergent PB, is that only one PB has to be calculated for any source-surface distance. If the finite PB input data is available, the dose engine of KonRadXP allows to calculate 3d dose distributions in any patient geometry. A detailed descriptions of the PB model and the dose engine can be found in (Nill, 2001, chap. 3) and in (Bortfeld et al., 1993).

3.A.2 Calculation of a finite parallel pencil beam for 2D-bMLC treatments

For the integration of the 2D-bMLC treatments into the dose engine of KonRadXP, a finite parallel photon PB was calculated in two steps. At first, the 3D water-dose distribution of a single divergent 2D-bMLC channel beam was assessed using MC simulations and the collimator model presented in chapter 2. Then, the dose distribution was converted into a non-divergent coordinate (fan-line) system, as required as input data.

3.A.2.1 MC simulation of a divergent 2D-bMLC beam

The setup of the MC simulation is shown schematically in figure 3.7. The setup is similar to that used for the dosimetric evaluation of the 2D-bMLC (see figure 2.5(a)). Also, the virtual photon source model and the 2D-bMLC model were the same as presented in chapter 2.

The pre-collimator was adapted, so that its projected field size at the isocentric plane would be 20×20 $\mathrm{mm^2}$. All absorber channels were closed except one of the most central channels, channel 1515 following the indexing defined in section 2.3.2. The collimator was tilted around the photon source, so that the beam of the open channel targeted the isocenter of the treatment machine, but that the channel remained full focusing at the same time (see also figure 2.22).

The water phantom was modelled as a box of liquid water with the dimensions 500×500×400 $\mathrm{mm^3}$ (400 mm in z-direction). The SAD was 800 mm, and the source surface distance (SSD) was 700 mm. The dose was scored within the phantom with a lateral resolution of 0.5 mm and a z-resolution of 2 mm. Finally, the dose distribution was scaled to 1 monitor unit (MU) and stored. 100 MU correspond to 1 Gray calculated in the isocenter for an open 100×100 $\mathrm{mm^2}$ field, a SAD of 1000 mm and a SSD of 950 mm (same photon source and water phantom).

The simulation was split up in two parts. In a first part the transport of the source photons through the the collimator was simulated, and the phase space was scored downstream the collimator, in the phase space plane shown in green in figure 3.7. In a second part the parti-

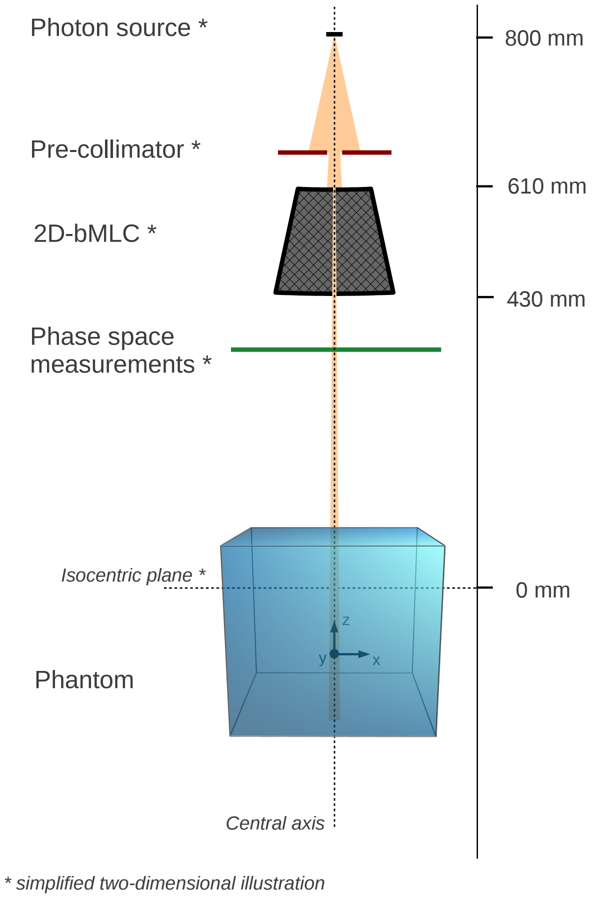

Figure 3.7: Scheme of the simulation setup for the central bixel (simplified two-dimensional illustration)

cle transport through the water phantom was simulated and the dose deposition was scored. Thereby, a common variance reduction method was applied: Each phase space particle was reused 20 times, but each time with an independent serial of random numbers. The simulations were performed in multiple parallel jobs.

The simulations were implemented with Geant4 version9.4p02. A Geant4 standard electromagnetic physics list with best advanced electromagnetic options was used[3]. The electron step size was limited to 0.05 mm.

3.A.2.2 Conversion into a finite parallel PB

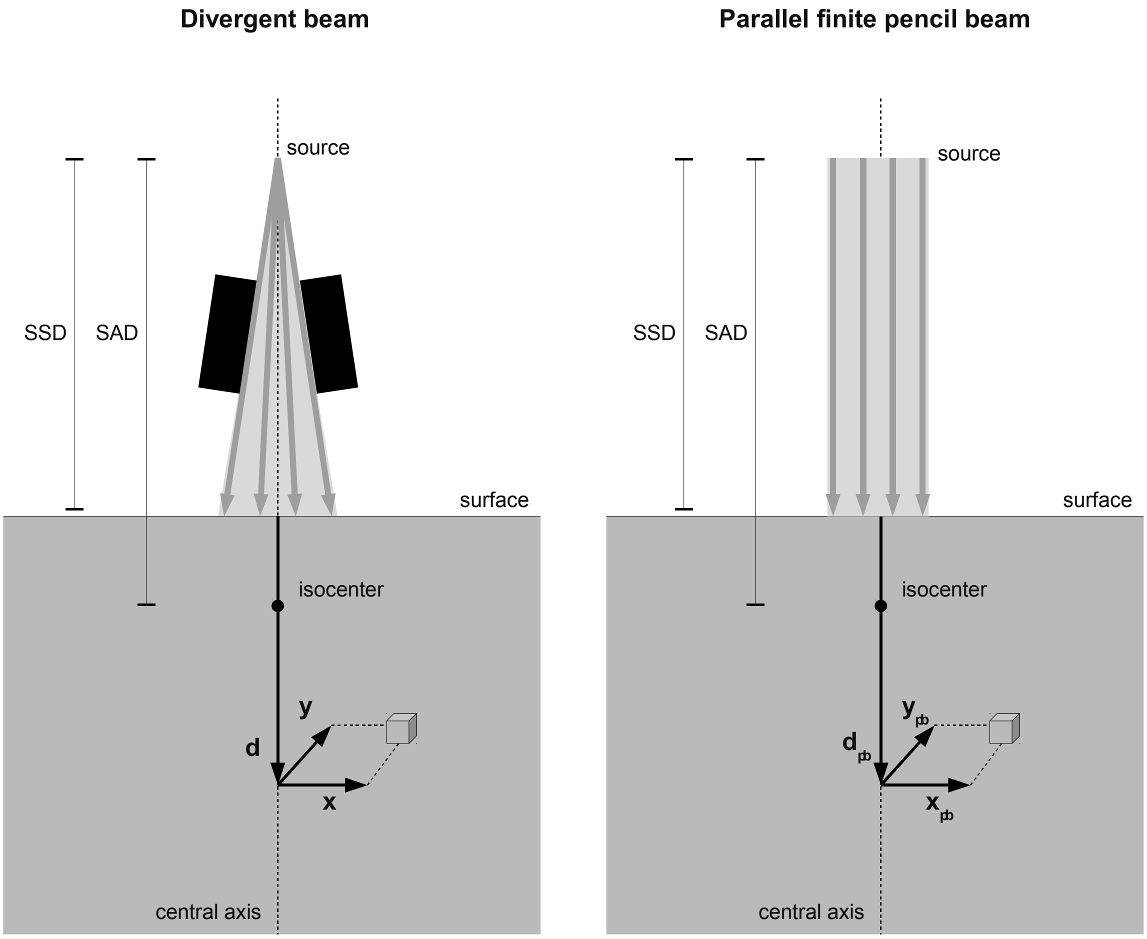

Figure 3.8: Divergent beam coordinate system and non-divergent coordinate system, in which the finite parallel pencil beam is stored.

The coordinate system, in which the MC calculated dose distribution of the divergent channel beam has been calculated and stored, is shown in figure 3.8 on the left side. P_u is the dose to a voxel u with the coordinates x_u, y_u and d_u. We define a second coordinate system for the finite parallel pencil beam (referred to as PB system) shown on the right side of figure 3.8. In principal, both coordinate systems are similar: The lateral coordinate axes are identical to

---

[3] The physics list was similar to that which is loaded with the physics list constructor emstandard_opt3. The physics list constructors are developed and maintained by the electromagnetic working group of the Geant4 collaboration. Further information can be found on `http://geant4.web.cern.ch/geant4/collaboration/working_groups/electromagnetic/physlist.shtml`.

those of the IEC gantry system, and the depth d is defined in the negative z-direction of the IEC gantry system (figure 2.5(b)). The origin is located at the patient's or phantom's surface.

The dose distribution of the finite parallel pencil beam was calculated for a regular grid with the same resolution as the grid used in the MC simulations (voxel size 0.5×0.5×2 mm^3). x_v^{pb}, y_v^{pb} and d_v^{pb} are the coordinates of voxel v in the PB dose cube; P_v^{pb} is the PB dose to voxel v.

The conversion of the MC calculated dose distribution into the PB dose distribution was performed voxel-wise. The following routine was applied for every voxel v of the PB dose cube in order to assess the entry P_v^{pb}:

1. The coordinates x_v^{pb}, y_v^{pb} and d_v^{pb} of the voxel v are converted into the divergent beam system using

$$x_v = x_v^{pb} \cdot \frac{SSD + d_v^{pb}}{SAD} \tag{3.19}$$

$$y_v = y_v^{pb} \cdot \frac{SSD + d_v^{pb}}{SAD} \tag{3.20}$$

$$d_v \simeq -SSD + \sqrt{\left(d_v^{pb} + \xi\right)^2 - {x_v}^2 - {y_v}^2} \tag{3.21}$$

with

$$\xi = \frac{SSD}{SAD} \sqrt{\left(x_v^{pb}\right)^2 + \left(y_v^{pb}\right)^2 + SAD^2} \quad . \tag{3.22}$$

SSD is the source-surface distance, SAD the source-axis distance (see also figure 3.8). The approximation in equation 3.21 is justified by x_v^{pb} and $y_v^{pb} \ll SSD$.

2. $P(d_v, x_v, y_v)$, the dose at point (d_v, x_v, y_v) in the divergent beam system, is assessed from the MC calculated 3D water-dose distribution by tri-linear interpolation.

3. The dose entry P_v^{pb} to voxel v in the PB system is determined by

$$P_v^{pb} = P(d_v, x_v, y_v) \left[\frac{SSD + d_v}{SAD}\right]^2 \quad . \tag{3.23}$$

In figure 3.9, we show dose maps and profiles for the final finite parallel pencil beam, which was used for dose calculation in KonRadXP.

3.A.3 Bixel spot positions for 2D-bMLC treatments

For KonRadXP, a bixel is specified by a set of parameters. Beside gantry angle, collimator angle and patient table angle, also the bixel spot position has to be given. The bixel spot position is defined by the x- and y-coordinates, that the bixel beam spot would have in the isocentric plane for gantry and colli angle 0 (see figure 3.10(a)).

In a 2D-bMLC treatment the bixels correspond to the 2D-bMLC channel beams. Therefor, the center of the theoretical projections of the channel openings onto the isocentric plane, were defined as the possible bixel beam spot positions. The center of a beam spot was calculated as the midpoint of the vertexes given in equation 2.27. In figure 3.10(b), we show all possible bixel spot positions for the 2D-bMLC in a scatter plot.

An adaptation of the dose calculation to other collimator or treatment design variations, as e.g the variations discussed in section 2.B.3, could be realised by adjusting the bixel beam spot positions respectively.

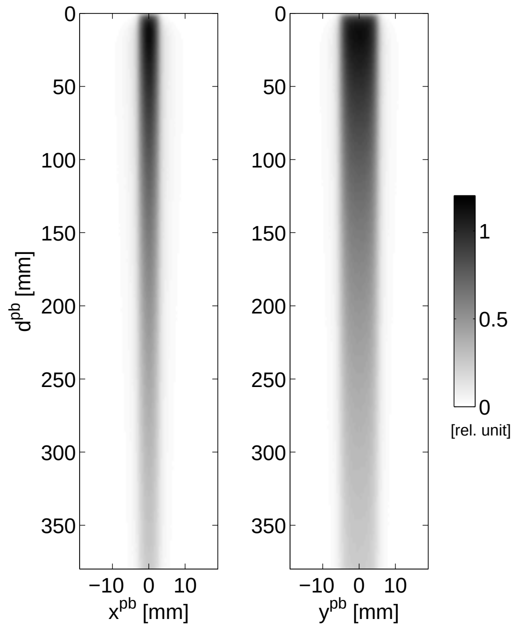

(a) 2D views of the dose distribution through the isocenter

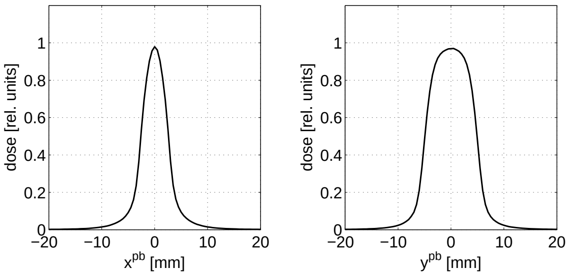

(b) Lateral profiles for a depth of 50 mm

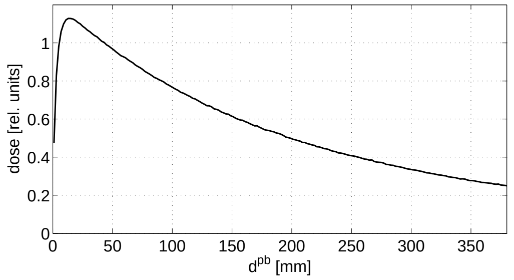

(c) Depth dose curve on central axis

Figure 3.9: Finite parallel PB for the dose calculation engine of KonRadXP.

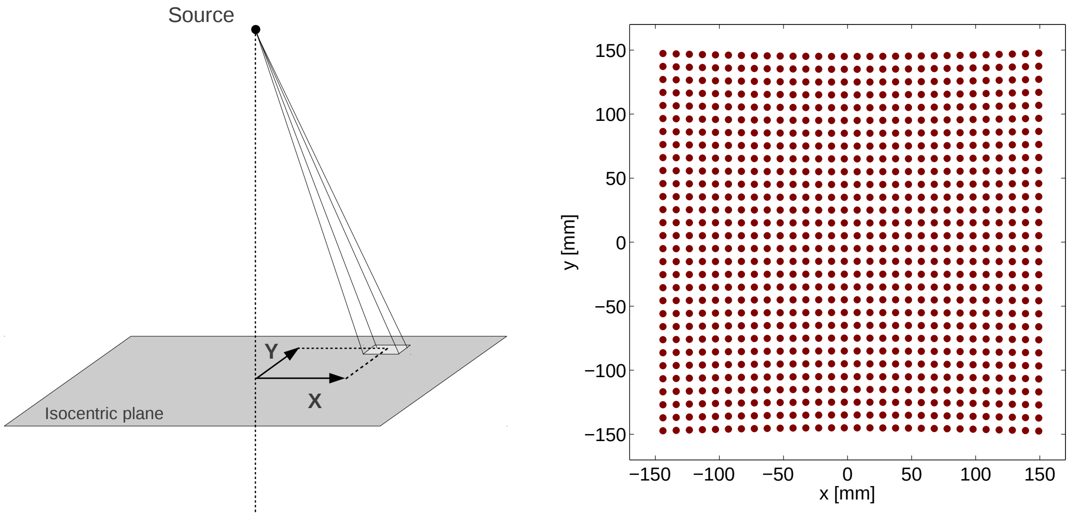

(a)

(b)

Figure 3.10: (a) The bixel spot position is defined by the x- and y-coordinates, that the bixel beam spot would have in the isocentric plane for gantry and colli angle 0. (b) Possible bixel beam spot positions for the 2D-bMLC.

Chapter 4

Sensitivity of treatment plan quality to TPS parameters

4.1 Overview

In this chapter, we present three additional planning comparison studies performed with the treatment planning system (TPS) presented in chapter 3. In the first study (section 4.2), the influence of N_{seg} on the final dose distribution was investigated for six patient cases. Based on the results of the study, we recommend a minimum number N_{seg} of 72. However, for patients with very large and complex target volumes, an increase of N_{seg} might be appropriate.

The goal of the second study (section 4.3) was to better understand the potential influence of T_F on the dose distributions optimized with the TPS. For the same six patient cases, 2D-bMLC plans were computed for different T_F, holding the other planning parameters fixed. Below a critical T_F, e.g. 16 s for a prostate case for which a very detailed analysis was performed, target coverage was insufficient. Above this value doses to the target volumes were rather independent on T_F, but the doses to several organs at risk did show a strong dependence on T_F.

In the third study (section 4.4), prostate plans were calculated for a regular fractionation regimen and for extreme hypofractionation. The plans should be equivalent concerning target coverage and sparing of OARs. It could be shown, that therefore the fractional delivery time T_F could be scaled with the fraction size.

Publication

Results from section 4.4 have been presented at the international *ESTRO 33 Conference* in Vienna, Austria, April 2014 (Altenstein et al., 2014).

4.2 Study of the Influence of N_{seg}

4.2.1 Introduction

The number of arc segments N_{seg} is one of the treatment parameters that have to be defined before plan optimisation (see section 3.3.2.1). In this study, the influence of N_{seg} on the final dose distribution was investigated for 6 cases. The goal was to find the minimum necessary number N_{seg} for each case respectively, and to give a guideline for the choice of N_{seg} for future patient plans.

4.2.2 Methods

The study was performed for cases 1 to 5 described in section 3.3.4 and for an additional prostate case (case 6). Dose prescriptions for cases 1 to 5 are summarised in table 3.1. The dose prescriptions for case 6 were as follows: 76 Gy median dose in 35 fractions were prescribed to the prostate (PTV 1), 70 Gy median dose to the a volume including the prostate and seminal vesicles plus a 7 mm margin (PTV 2). For each case 2D-bMLC plans were optimised with N_{seg} of 48, 72 and 96. For cases 1 and 6, with relatively small target volumes, additional plans were computed with N_{seg} equal to 36. Other planning parameters, including the penalty values for overdosage and underdosage, were hold unchanged for each case respectively. $\dot{D}_{\min}$ and $\dot{D}_{\max}$ were 500 and 2000 MU per minute respectively. T_F was 20 s for case 6, and the values for cases 1-5 are specified in table 3.1. The target point, coincident with the point of rotation of the treatment, was at the center of mass of the primary PTV ± 5 mm.

For this study, the TPS calculated dose distributions were used for plan evaluation. The plans were evaluated by visual inspection and dvh analysis. Finally, for each patient the minimum number N_{seg}, necessary to assure sufficient target dose coverage and uniformity without hotspots in the normal tissue, was identified. For verification the selected plans were recalculated with the 4D MC tool, which considers gantry and collimator dynamics appropriately (see section 3.3.3).

4.2.3 Results and discussion

As an example, we show dose distributions calculated for case 6 in figure 4.1. The dose distributions shown in figure 4.1(a) and 4.1(b), for N_{seg} 36 and 48 resp., show significant dose inhomogeneities close to the PTV 2. Therefor, the plans were rejected. $N_{seg} = 72$ however was sufficient to assure good target dose coverage and uniformity, and no significant improvement could be obtained with $N_{seg} = 96$.

In general, the following characteristics were observed, if N_{seg} was not sufficient: Dose inhomogeneities close to or within the target volumes, insufficient target dose coverage, dose hot spots in the normal tissue and OARs. These characteristics lead to rejection of the plan and the respective number of arc segments.

The minimum necessary number for N_{seg} for the six cases were:

Case	**Volume of largest PTV**	**N_{seg}**
1. Prostate only	74 ml	48
2. Prostate boost	1040 ml	72
3. Oral cavity	1083 ml	72
4. Nasopharynx	1324 ml	72
5. Anal	3329 ml	96
6. Prostate 2	170 ml	72

A number of 48 arc segments was only sufficient for the prostate only case with a relatively small target volume. For all other cases $N_{seg} = 72$ was acceptable, except for the anal carcinoma case with very large and complex PTVs (see also table 3.1 and figure 3.5).

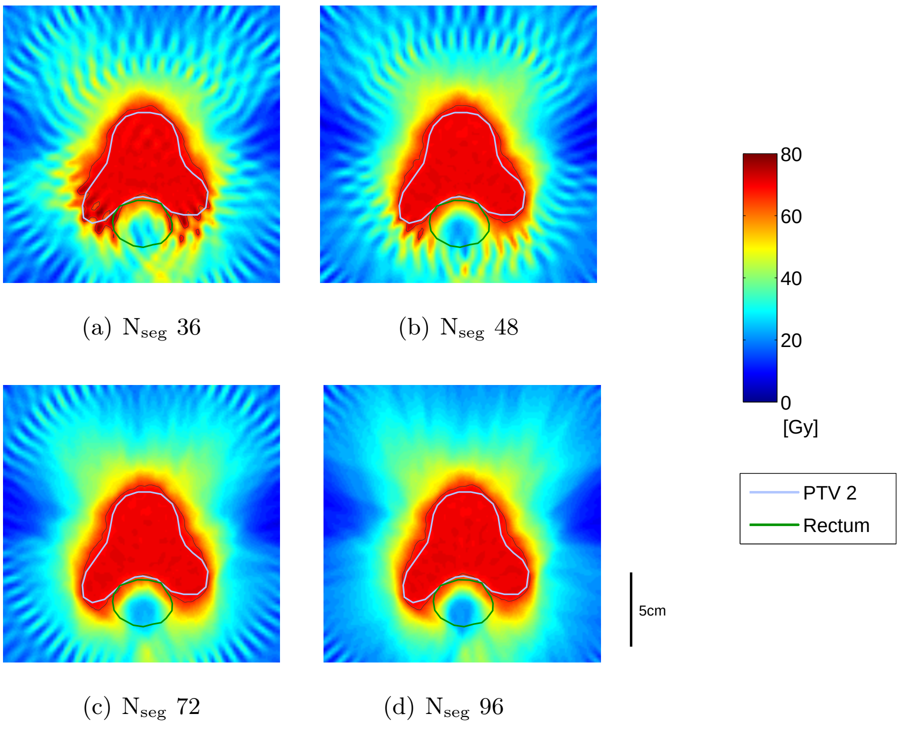

(a) N_{seg} 36 (b) N_{seg} 48

(c) N_{seg} 72 (d) N_{seg} 96

Figure 4.1: Dose maps of 2D-bMLC plans calculated for case 6 for different N_{seg}. Other treatment parameters were the same for all plans. The thin black line corresponds to the 95% isodose of PTV 2.

4.2.4 Conclusion

For the planning of 2D-bMLC treatments, we propose a minimum number of 72 for N_{seg}. This number should ensure sufficient target coverage for a wide range of target volumes. For patients with very large and complex targets, such as for the patient with anal cancer (case 5 → see also sections 3.3–3.4), N_{seg} might be increased to 96 or to an even larger number as necessary. PTV volumes may be used as indicators for the choice of N_{seg}, however, extent and complexity of the target volume should also be considered.

Another option would be to use a larger number of N_{seg}, such as 96 or larger, for all cases. But of course, a larger N_{seg} implies smaller arc segments and can possibly result in more opening and closing shifts per treatment. And finally, because of equation 3.4, an unintended lower bound for T_F can also be the consequence of larger N_{seg}.

4.3 Study of the Influence of T_F and Comparison to a ‘Best Case’ IMRT plan

4.3.1 Introduction

Beside N_{seg}, also the fractional treatment time T_F is a planning parameter, that currently has to be set before plan optimisation (see section 3.3.2.1). In this study, 2D-bMLC treatment plans were calculated for different T_F, whereas N_{seg} was not changed. The goal was to better understand the potential influence of T_F on the optimisation result and hence on the final dose distributions. A very detailed study was performed for a prostate case. In addition, the 2DbMLC plans for this case were compared to a potential 'best case' IMRT plan, optimised for a conventional MLC and for 180 beam directions.

4.3.2 Methods

The study was performed for cases 1 to 5 described in section 3.3.4 and for an additional prostate case (case 6). For case 1 to 5, with the dose prescriptions given in table 3.1, plans were optimised for two different $\mathrm{T_F}$ respesctively: For 20 and 40 s for the prostate cases 1 and 2, and for 25 and 40 s for cases 3 to 5.[1] Other planning parameters than $\mathrm{T_F}$, including the penalty values for overdosage and underdosage, were hold unchanged for each case respectively. $\dot{D}_{\mathrm{min}}$ and $\dot{D}_{\mathrm{max}}$ were set to 500 and 2000 MU per minute respectively.

A more detailed study was performed for case 6. Dose prescription were as follows: 76 Gy median dose in 35 fractions were prescribed to the prostate (PTV 1), 70 Gy median dose to a volume including the prostate and the seminal vesicles plus a 7 mm margin (PTV 2). 2D-bMLC plans were calculated for $\mathrm{T_F}$ of 14, 16, 18, 20, 25, 30, 40 and 60 s. In the following, the plans are labelled by their $\mathrm{T_F}$. Again, other planning parameters were hold fixed. $\mathrm{N_{seg}}$ was 72, $\dot{D}_{\mathrm{min}}$ and $\dot{D}_{\mathrm{max}}$ were 500 and 2000 MU per minute respectively. For comparison, an additional plan (referred to as 2D-bMLC*) was optimised without constraints on $\mathrm{T_F}$, thus without maximum channel opening time per arc segment.

The TPS calculated dose distributions were used for a first plan evaluation. The plans were evaluated by visual inspection and by visual and quantitative dvh analysis. The plans for the cases 1 to 5 were partly recalculated with the 4D MC tool (see section 3.3.4). For these cases, the MC doses were used for a final plan evaluation. The 4D MC tool considers gantry and collimator dynamics appropriately (section 3.3.3).

For case 6, the clinically applied IMRT plan with eight beam directions was used as reference (referred to as IMRT ref.). The plan was made for the Siemens ARTISTE 6 MV 160 MLC$^{\mathrm{TM}}$. Additionally, a hypothetical IMRT plan for the FFF Siemens ARTISTE 7 MV 160 MLC$^{\mathrm{TM}}$ and for 180 beam directions was calculated (IMRT 180). The algorithm used for the inverse optimisation of the latter plan was chosen in such a way, that major discrepancies in the dose distributions to those of the 2D-bMLC plans should only be caused by the differences in the treatment modalities, and especially the constraints used for the 2D-bMLC plans. Discrepancies due to the optimisation algorithm should be relatively small. No constraints were used for the fluency maps of plan IMRT 180, and no post-processing (sequencing) was applied after plan optimisation.

4.3.3 Results and discussion

Here, we particularly focus on case 6. Plan 14s was rejected because of insufficient target dose coverage. The treatment time was simply not long enough to deliver enough dose to the PTVs. However with $\mathrm{T_F} \geq 16$ s, the clinical goals concerning target coverage were fulfilled. Moreover, with $\mathrm{T_F} \geq 18$ s, all 2D-bMLC plans had very similar DVHs for PTV 1 and 2.

Exemplary for the 2D-bMLC plans with $\mathrm{T_F} \geq 18\,\mathrm{s}$, we compare in figure 4.2(a) and 4.2(b) the PTV DVHs of 20s to those calculated for IMRT ref. and IMRT 180. IMRT 180 represents, so to say, a 'best case' reference, which could be achieved with the Siemens 160 MLC$^{\mathrm{TM}}$. Concerning doses to PTV 1, differences between the 2D-bMLC plans ($\mathrm{T_F} \geq 18$ s) and the reference plans were small, also in quantitative DVH analysis. However, larger differences can be reported for

---

[1] The plans have already partly be presented in sections 3.3 and 2.4.

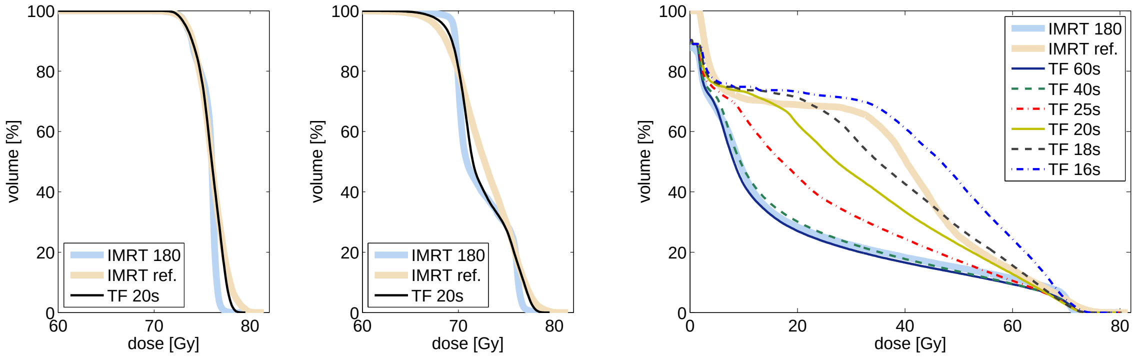

(a) PTV 1

(b) PTV 2

(c) Rectum

Figure 4.2: DVHs for case 6. The 2D-bMLC plans are labelled with the respective T_F. IMRT 180 is the IMRT plan calculated for a conventional MLC and 180 beam directions. IMRT ref. is the clinically applied reference plan. All 2D-bMLC plans with $T_F \geq 18$ s had very similar DVHs for PTV 1 and 2.

the dose conformity. The conformity index[2] was 1.20–1.22 for the 2D-bMLC plans, compared to 1.59 for IMRT ref. and 1.16 for IMRT 180.

The minimum dose $D_{98\%}$ to PTV 2 was 95–97% of the prescription dose for 2D-bMLC, 94% for IMRT ref. and 99% for IMRT 180. Also concerning 95%-coverage, the 2D-bMLC plans ($V_{95\%}$ = 99%) performed better than IMRT ref. (97%) but slightly worse than IMRT 180 (100%). Dose uniformity and conformity for PTV 2 were similar for all plans.

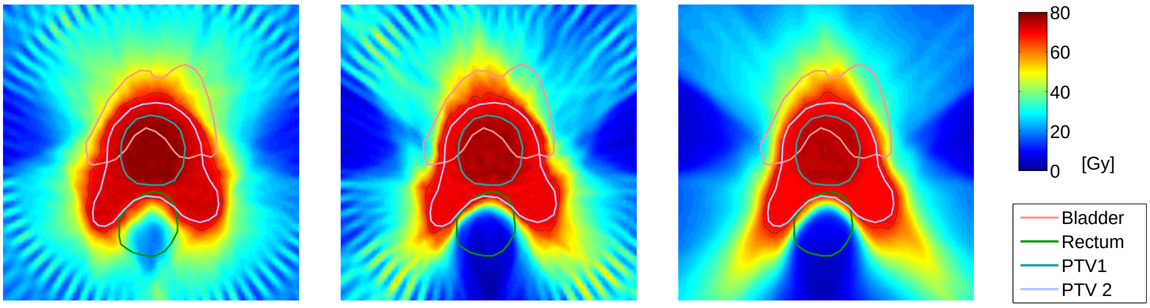

(a) T_F 20s

(b) T_F 60s

(c) IMRT 180

Figure 4.3: Dose maps of 2D-bMLC plans with different T_F and of plan IMRT 180 calculated for case 6. The thin black line corresponds to the 95% isodose of the PTV 2.

The doses to the OARs were partly strongly dependent on T_F, also for $T_F \geq 18$ s. Here, we want to refer to figure 4.3(a) and 4.3(b), were dose maps are shown for the plans 20s and 60s respectively. The differences in the two dose maps can be explained as follows: The maximum opening time per arc segment is directly proportional to T_F. Thus, if T_F is longer, the constraints on the optimisation parameters, namely the opening times per channel and arc segment, are relaxed; the potential to attach more weight to individual bixels, in order to better conform the dose to the target, is increased. One can clearly see in the figures, that especially the rectum dose is reduced if T_F is increased from 20 to 60 s. In figure 4.3(c), the dose map for the 'best case' reference plan IMRT 180 for the same slice is shown.

---

[2] See section 3.3

The penalty values for the optimisation were chosen in that way, that target coverage was prioritised. Therefor, a reduced potential for beam modulation pre-dominantly affects the doses to the OARs, especially to the rectum which is partly enclosed by the PTV 2. Consequently, the DVH of the rectum largely depend on $\mathrm{T_F}$, as can be seen in figure 4.2(c). The DVH of 60 is very similar to that of IMRT 180. With increasing $\mathrm{T_F}$, the DVH lines are quasi shifted to higher doses.

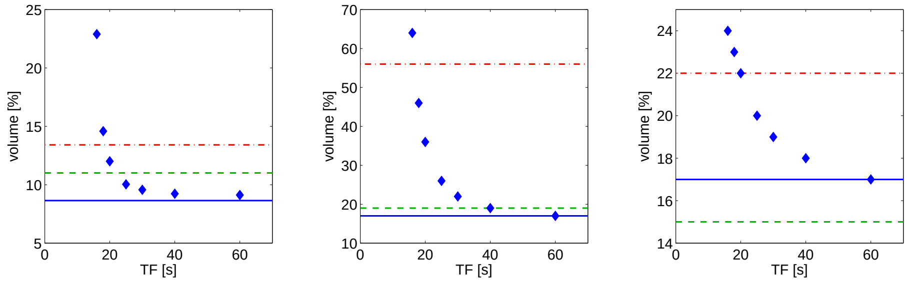

(a) Rectum $\mathrm{V_{80\%}}$ (b) Rectum $\mathrm{V_{50\%}}$ (c) Bladder $\mathrm{V_{50\%}}$

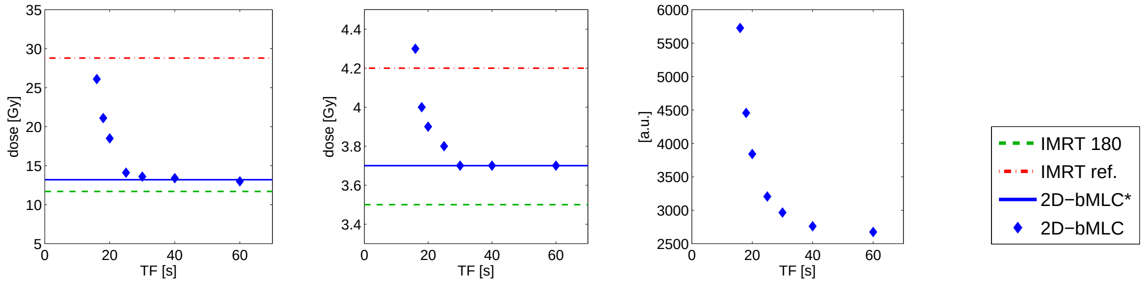

(d) Right femoral head $\mathrm{D_{2\%}}$ (e) Normal tissue $\mathrm{D_{mean}}$ (f) Obj. funct. value

Figure 4.4: DVH analysis for case 6. The parameters assessed for the 2D-bMLC plans are plotted against TF. 2D-bMLC* is a 'step-and-shoot' 2D-bMLC plans without constraints for the delivery time per arc segment. IMRT 180 is the IMRT plan calculated for a conventional MLC and 180 beam directions. IMRT ref. is the clinically applied reference plan.

In figure 4.4, DVH parameters assessed for the rectum, the bladder, the right femoral head and the normal tissue VOI (body without PTV 2) are plotted against $\mathrm{T_F}$. For these OARs the DVHs were clearly dependent on $\mathrm{T_F}$, including the other femoral head. The dependence is also reflected in the final value of the objective function, which is minimised in the optimisation process (figure 4.4(f)).

For all shown DVH parameters, a smaller value is preferable. The parameters decrease with $\mathrm{T_F}$ approaching the level of the unconstrained 2D-bMLC plan denoted 2D-bMLC* (blue line). For all OARs, this level, which clearly fulfils the clinical goals, is approximately reached with $\mathrm{T_F}$ 60 s. The parameters calculated for the 'best case' reference (dashed green line) are comparable to those of 2D-bMLC*. IMRT 180 performs slightly better concerning doses to the bladder and the normal tissue VOI, but slightly worse concerning $\mathrm{V_{50\%}}$ and $\mathrm{V_{80\%}}$ for the rectum. As discussed before, IMRT 180 should in principle represent the best possible plan. However, due to the differences in the optimization strategies and the employed stopping criteria, it is also possible, that a 2D-bMLC plan somewhat better fulfils certain optimization goals. Overall, the differences between 2D-bMLC* and IMRT 180, thus between the dashed green and the blue lines in figure 4.4, were estimated as clinically not relevant. The parameters assessed for the clinical reference plan IMRT ref. are added to the plots as dash dotted red lines. Only for $\mathrm{T_F}$ below 20 s, the 2D-bMLC plans exceed this level.

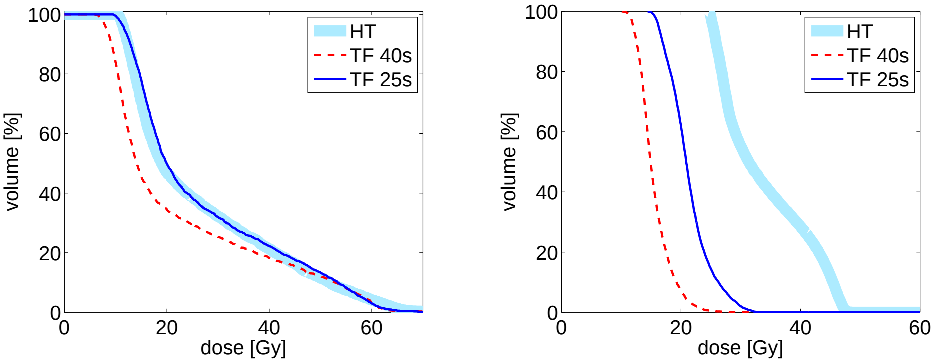

(a) Case 4. DVH for the left parotid.

(b) Case 5. DVH for right femoral head.

Figure 4.5: DVH comparison of 2D-bMLC plans calculated with different T_F (thin lines). HT is the helical Tomotherapy reference plan, which had be applied clinically.

The femoral heads were the only OARs for which the maximum doses $D_{2\%}$ had a considerable dependence on T_F. For both femoral heads the dependence was very similar, and for all 2D-bMLC plans $D_{2\%}$ to the femoral heads was smaller than for IMRT ref..

For the other cases, similar results can be reported. In section 3.4 the plans 20s respectively 25s were already discussed in detail and compared to the HT reference plan. Overall, target coverage did not change considerably if T_F was increased to 40 s. However, doses to several OARs did show a dependence on T_F, especially the parotid glands for the head-and-neck cases 3 and 4 and the femoral heads in the anal carcinoma case 5 (see figure 4.5). But finally, the differences were seen as clinically rather insignificant.

For the prostate cases 1 and 2, the differences between 20s and 40s were already reported in section 3.4.2. Consistently with the results for case 6, the increase in fractional treatment time from 20 to 40 s resulted in better sparing of the rectum and the bladder (see also figure 3.6(b)). However, also for case 1 and 2, the differences were seen as not clinically significant.

4.3.4 Conclusion

Below a critical T_F, e.g. 16 s for case 6, target coverage was insufficient. Above this value PTV doses were rather independent on T_F, but the doses to several OARs did show a strong dependence on T_F. Concerning PTV coverage and doses to the OARs, the plans calculated for T_F of 20 or 25 s were comparable to the clinical reference plans. The potential to spare the OARs was further increased with T_F until saturation was reach at about 40–60 s.

It needs to be noted that a shorter delivery time can lead to inferior optimisation results. Finally, a careful weighing up of shorter delivery time and better plan quality might be necessary for each clinical indication or even each patient geometry.[3]

---

[3] As a side node, we want to add, that for cases with breathing induced motions, one could also think about a modified treatment mode with delivery in several fast rotations in a repeated manner. Such a technique could be combined with a breath holding technique to reduce motion during each rotation.

4.4 Hypofractionated Prostate Plans

4.4.1 Introduction

Hypofractionated treatments are delivered in fewer fractions with larger fraction doses. It has been hypothesised, that hypofractionated treatments are favourable for some tumours with low α/β ratio. Several clinical studies have been performed or are still ongoing to clarify the role of hypofractionation for prostate cancer treatments.(Brenner and Hall, 1999; Cabrera and Lee, 2013; Lee, 2013; Oliveira et al., 2012; RTOG, 2013)

For this study, 2D-bMLC prostate plans were calculated for three different fractionation regimina. The plans should be equivalent concerning target coverage and sparing of OARs. We wanted to show, that therefor the fractional delivery time $\mathrm{T_F}$ can be scaled with the fraction size. Furthermore, the same plans were also used in the study about the impact of intrafraction motion presented in section 5.3.

4.4.2 Methods

The clinical target volume (CTV) was the same as the Gross Tumour Volume (GTV) and consisted of the prostate only. The PTV was defined as the CTV plus a 3 mm margin posteriorly and a 5 mm margin in all other dimensions. Plans were calculated for the following fractionation schemes:

Plan	**Prescription dose**
F35	$D_{95\%} \geq 35 \times 2.1\,\mathrm{Gy}$ (Total dose 73.5 Gy)
F12	$D_{95\%} \geq 12 \times 4.3\,\mathrm{Gy}$ (Total dose 51.6 Gy)
F5	$D_{95\%} \geq 5 \times 7.25\,\mathrm{Gy}$ (Total dose 36.25 Gy)

The isodose line used for the prescription dose should cover a minimum of 95% of the PTV. Target delineation as well as the prescriptions for the two hypofractionated treatments F5 and F12 followed the RTOG 0938 protocol (RTOG, 2013). A corresponding standard fractionation scheme was used for F35.

All plans were optimised for 72 arc segments. $\dot{D}_{\min}$ and $\dot{D}_{\max}$ were 500 and 2000 MU per minute respectively. $\mathrm{T_F}$ was 65 s for F5, 40 s for F12 and 20 s for F35. $\mathrm{T_F}$ was approximately scaled with the fraction size. For MC recalculation the dimensions of the pre-collimator field were set to 120×80 mm^2 (in the isocentric plane). The resolution of the voxel grid was 1×1×2 mm^2 (same as CT data set). $\overline{F}_{d>0.5d_{\max}}$ of the final MC dose distributions was about 1%. The MC calculated plans were rescaled to match the dose prescriptions for the PTV. The Plans were evaluated by visual inspection of the dose distributions and by visual and quantitative dvh analysis.

4.4.3 Results and discussion

Comparing the results of the calculation methods separately (TPS or MC), F5, F12 and F5 have very similar dose distributions - of course relatively seen to the respective prescription dose. Small differences can only be reported for the MC calculated plans, and that only for $\mathrm{D}_{2\%}$, UI and CI for the PTV (see table 4.1). Differences in the doses to the OARs are insignificant.

These differences can be explained as follows: As already discussed in section 3.5, the MC plans generally show increased target dose inhomogeneity compared to the TPS plans. The opening and closing shift of the absorber channels, neglected in the TPS calculations but modelled in the

Table 4.1: PTV report for prostate plans with different fractionation regimina. TPS results are given in black, MC results in grey. All dose values are given as percentage of the respective prescription dose. DVH parameters are defined in section 3.3.4.

	F35		**F12**		**F5**	
Prescr. [Gy]	73.5 (35×2.1)		51.6 (12×4.3)		36.25 (5×7.25)	
T_F [s]	20		40		65	
PTV						
$D_{98\%}$ [%]	98.7	98.8	98.8	98.8	98.8	98.8
$D_{50\%}$ [%]	102.1	104.1	102.0	103.6	102.0	103.4
$D_{02\%}$ [%]	104.6	108.6	104.5	107.5	104.6	107.0
$V_{100\%}$ [%]	95	95	95	95	95	95
CI	1.16	1.27	1.15	1.25	1.15	1.24
UI	1.04	1.08	1.04	1.07	1.04	1.06

MC simulations, is the main reason. The more shifts are modelled, the more the effect should carry weight. And as a matter of fact, this effect is less pronounced for the hypofractionated treatments with larger fraction sizes and overall less required opening/closing shifts. This trend can be seen in figure 4.6, where PTV DVHs are shown for F5 and F35. In table 4.1, the increase in target dose inhomogeneity is reflected in larger values of the uniformity index UI and the maximum dose $D_{2\%}$. Due to the rescaling also the conformity index CI is slightly increased, but the dose coverage ($V_{100\%}$) and the minimum dose $D_{98\%}$ are not affected.

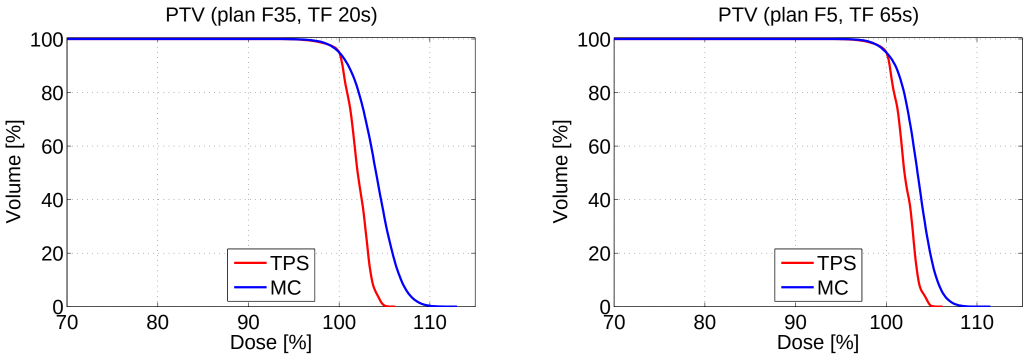

(a) plan F35: 35×2.1 Gy

(b) plan F5: 5×7.25 Gy

Figure 4.6: Prostate plans with standard fractionation and extreme hypofractionation: DVHs of the PTV for the TPS plan and the MC recalculated and rescaled plan. The dose is given as percentage of the prescription dose, 73.5 and 36.25 Gy respectively.

Overall, the results confirm the hypothesis, that for calculating 2D-bMLC plans for different fractionation schemes, the fractional delivery time T_F can be scaled with the fraction size. As discussed in the previous paragraph, the small discrepancies in the relative dose distributions are rather due to the different fraction numbers and not influenced by T_F.

For the three fractionation schemes, T_F was below delivery times typical for the treatment techniques applied in the clinics today. With volumetric modulated arc therapy (VMAT) (Otto, 2008a; Ulrich et al., 2007a; Wang et al., 2008; Yu, 1995), delivery times of about 1 minute are possible for standard fractionation (fraction size 2 Gy) (Thomas et al., 2013). In comparison, the scheduled T_F of the 2D-bMLC treatment was 25 s. In general, delivery times of VMAT are below or in the same range of those of other clinical techniques (Bedford, 2009; Palma et al., 2008; Wolff et al., 2009).

For extreme hypofractionation with only 5 fractions and a fraction dose of 7.25 Gy, $\mathrm{T_F}$ of the 2D-bMLC plan was 65 s. For a similar fractionation regimen (35 Gy minimum dose in 5 fractions), MacDougall et al. (2014) reported delivery times of about 3 minutes for VMAT with a flattened linac beam. With a flattening filter free 10 MV linac and a maximum dose rate of 2400 MU/min, delivery times of about 2 minutes can be achieved, as reported by Alongi et al. (2013).

4.4.4 Conclusion

For calculating 2D-bMLC plans for different fractionation schemes, the fractional delivery time $\mathrm{T_F}$ can be scaled with the fraction size. Target dose inhomogeneity of the MC calculated plans is affected by the number of modelled opening and closing shifts. Therefore, target dose inhomogeneity was slightly reduced in the hypofractionated treatment regimina with fewer fraction numbers and overall less required opening/closing shifts. The delivery times of the 2D-bMLC treatments were below typical delivery times of clinically applied treatment techniques.

Chapter 5

Impact of Geometrical Misalignment and of Intrafraction Motion on 2D-bMLC doses

5.1 Overview

The design of the 2D-bMLC differs substantially from the design of conventional MLCs. Firstly, the radiation fields are spatially fractionated into stripes. The fractionation is inherent to the system. Secondly, the fields are formed by long and thin absorber channels. Because of these two special characteristics, the 2D-bMLC treatments might be notably sensitive to geometrical misalignments of the collimator on the one hand, and to patient motion during treatment delivery, also referred to as intrafraction motion, on the other hand. Both aspects have been investigated in MC studies that we present in this chapter.

In the first study, we analysed in detail the influence of collimator misalignments on the primary radiation efficiency (section 5.2). The possible impact of variations of the linac source size were also examined. The goal of the second study was to estimate the dosimetric effects of intrafraction motion for 2D-bMLC treatments (section 5.3). The 4d MC tool was extended, so that rigid patient motion could be modelled continuously during radiotherapy delivery. The new feature was used for the motion-encoded recalculation of standard and of hypofractionated prostate plans.

Publication

Results from section 5.2 have been presented at the *43th Annual Meeting of the German Society of Medical Physics* in Jena, Germany, September 2012 (Altenstein et al., 2012c). Results from section 5.3 have been presented at the international *ESTRO 33 Conference* in Vienna, Austria, April 2014 (Altenstein et al., 2014).

5.2 Study of the Influence of Geometrical Misalignment on the Primary Radiation Efficiency

5.2.1 Introduction

With its especially thin absorber channels, the design of the 2D-bMLC (see figure 2.3.1) might be notably sensitive to geometrical misalignments of the collimator as well as to variations of the linac source size. Misalignments or variations of the source size can be caused by tolerances in system installation and calibration.

In chapter 2, we presented the dosimetric properties of the perfectly aligned 2D-bMLC assessed in MC simulations. The aim of this study was to investigated in detail, how 2D-bMLC fields are influenced by possible geometrical misalignments and by variations of the source size. A quantitative analysis was performed for the primary radiation efficiency.

5.2.2 Methods

5.2.2.1 MC setup

The MC setup is shown in figure 5.1. The setup is similar to that used for the dosimetric characterisation of the 2D-bMLC presented in chapter 2. The 2D-bMLC model with 30 by 30 absorber channels, the pre-collimator and the source model are described in sections 2.3 and 2.A.

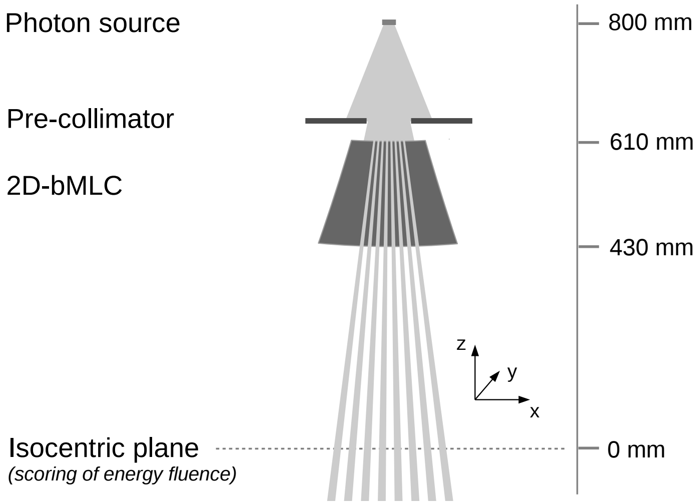

Figure 5.1: MC setup used to calculate the energy fluency of 2D-bMLC fields in the isocentric plane.

.

In all MC simulations performed for this study, the central 10 by 10 elements of the collimator were open. The corresponding pattern of open channels is shown in figure 2.7(a). Different to the simulations presented in chapter 2, the 2D-bMLC was tilted around the linac source as described in section 2.B.3.2 by an angle of -$\frac{\alpha_b}{2}$.[1]

Downstream the 2D-bMLC in the isocentric plane, the 2D distribution of the absolute energy

---

[1] The -$\frac{\alpha_b}{2}$-tilt was applied in this study in order to reduce the interference of the pre-collimator (see dicussion in section 2.4.3.1). Additional testing has shown, that relative differences in the primary radiation efficiency factors calculated with and without the tilt are below 1%.

fluency was scored in a regular mesh. The scoring resolution was 0.5 mm in both directions. For a quantitative analysis, primary radiation efficiency factors (EF) of the 2D-bMLC were calculated by dividing the integral energy fluency in the isocentric plane by the integral energy fluency calculated for a reference field, an open non 2D-bMLC 100mm-square field, in the same plane. Additional calculations have shown, that values of EF estimated that way were very similar to values calculated with the method described in 2.3.3.3, but that calculation times were reduced significantly.

The MC simulations were performed with Geant4 release 9.5. A Geant4 standard electromagnetic physics list with best advanced electromagnetic options was used[2].

5.2.2.2 Variations of the MC setup

Six series of MC simulations have been computed. The series are referred to by the lower case characters a to f. In series a to e, different misalignments of the 2D-bMLC were studied separately. In series f, 2D-bMLC fields were calculated for different source sizes. The pictograms in figure 5.2 visualize the geometrical changes of the simulation setup performed in each series respectively.

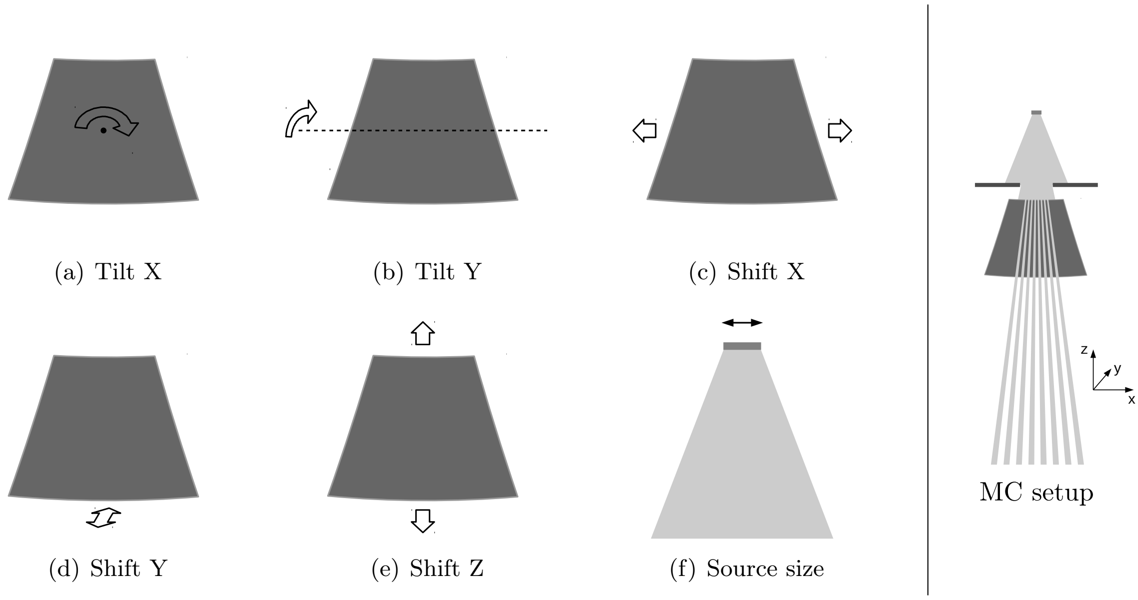

(a) Tilt X (b) Tilt Y (c) Shift X

(d) Shift Y (e) Shift Z (f) Source size

MC setup

Figure 5.2: Pictograms of the geometrical variations of the MC setup. The variations were studied separately in series of simulations. See figure 5.1 for a detailed description of the basic setup.

In the following, we itemize short explanations of the studied geometrical variations. A simulation parameter is related to each variation respectively, and in the MC series, only one of these parameters was changed respectively. Following to the descriptions, we give lists of values for the parameters under examination. For each value a separate MC simulation was performed:

(a) Tilt X → Tilt of the collimator perpendicular to the field stripes
Values tilt angle: 0.0 0.1 0.2 0.3 0.4 0.5 0.7 0.9 deg

---

[2] The physics list was similar to that which is loaded with the physics list constructor emstandard_opt3. The physics list constructors are developed and maintained by the electromagnetic working group of the Geant4 collaboration. Further information can be found on `http://geant4.web.cern.ch/geant4/collaboration/working_groups/electromagnetic/physlist.shtml`.

(b) Tilt Y → Tilt of the collimator in parallel to the field stripes
Values tilt angle: 0.0 0.4 0.8 deg

(c) Shift X → Lateral shift of the collimator perpendicular to the field stripes
Values shift: 0.0 0.4 0.8 1.2 mm

(d) Shift Y → Lateral shift of the collimator in parallel to the field stripes
Values shift: 0.0 0.4 0.8 1.2 mm

(e) Shift Z → Vertical shift of the collimator
Values shift: -1.2 -0.6 0.0 0.6 1.2 mm

(f) Source size → Variation of the std of the Gaussian shaped photon source
Values std: 0.15 0.30 0.45 0.60 0.75 0.90 1.20 1.50 mm

The parameters which were not varied in a series respectively, were set to their basic values: 0 deg for tilt angles, 0 mm for displacement shifts and 0.45 mm for the source std. The basic values correspond to the perfectly aligned 2D-bMLC and to the source size assessed from experimental data (see section 2.A).

The tilts performed in the series a and b are small rotations performed around axes through the geometrical center of the 2D-bMLC (and should not be confused with the tilts around the source). The axes of rotation were parallel to the y and the x axis of the GANTRY system (figure 2.5(b)) respectively. The displacement shifts in c, d and e were in parallel to the axes of the GANTRY system respectively.

Small tilts (up to several degrees) of the collimator around the z-axis should implicate a corresponding rotation of the radiation field, but should not lead to an essential reduction of primary radiation efficiency. Tilts around the z-axis were therefore not included into the study.

5.2.3 Results

In Figure 5.3, EF is plotted against the different geometrical parameters which have been under examination. Additionally, we show colour maps and central lateral profiles of the energy fluency for selected series in figure 5.4 to 5.7. For the profiles in x-direction (perpendicular to the 2D-bMLC field stripes), the energy fluency was averaged in y-direction from -25 mm to +25 mm. All values of energy fluency are given relative to the energy fluency calculated in the center of the reference field.

The following observations can be summarized:

(a) Tilt X: EF falls from approximately 0.44 for tilt angle 0.0 to 0.02 for tilt angle 0.7 degrees or greater. This corresponds to a relative reduction of 95%. Figure 5.4 shows energy fluency maps, and lateral profiles of the energy fluency are shown in figure 5.5. For tilt angles greater than 0.5 degree, cross leakage peaks appear outside the originally collimated field.

(b) Tilt Y: EF decreases relatively slightly with increasing tilt angle in parallel to the field stripes. Variations in EF are below 2% for the range under examination.

(c) Shift X: Displacement shifts of 0.4, 0.8 and 1.2 mm lead to relative decreases in EF of 5%, 18% and 33% respectively. The shifts perpendicular to the field stripes also result in a shifts of the radiation field as can be seen in figure 5.6.

(d) Shift Y: EF decreases relatively slightly with the shift in parallel to the field stripes. Variations in EF are below 1% for the range under examination.

(e) Shift Z: EF is increased if the collimator is moved towards the source and decreased if the

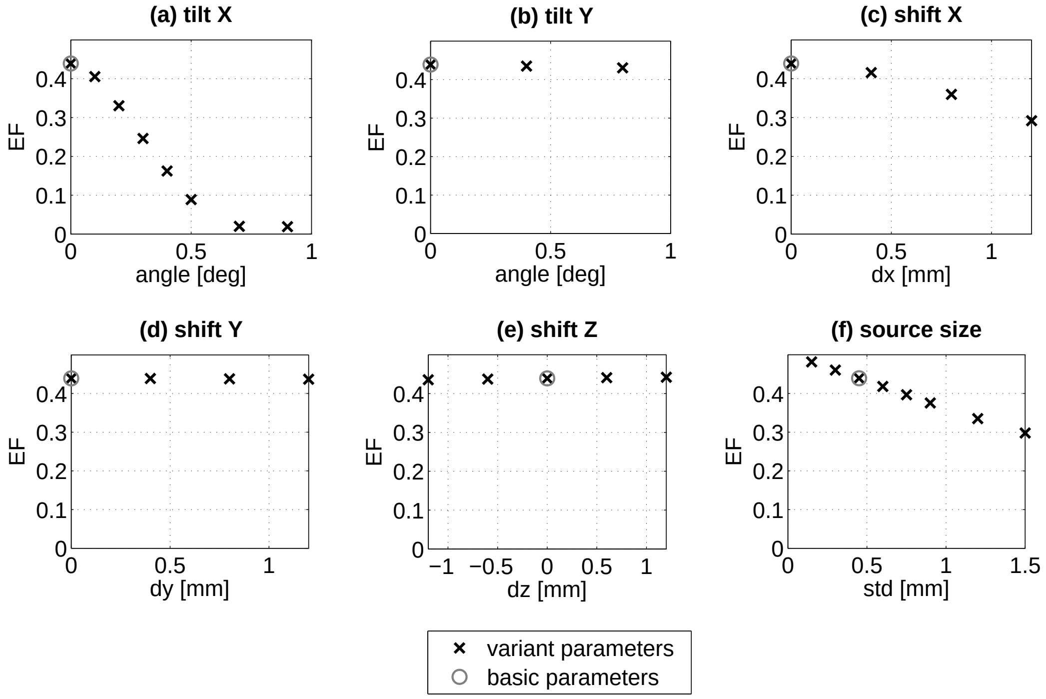

Figure 5.3: EF plotted against the varied simulation parameters. In each MC series, only one parameter was varied, and the other parameters were set to the basic values respectively.

collimator is moved away from the source. However, variations in EF are below 1% for the range under examination.

(f) Source size: EF decreases with increasing width of the Gaussian shaped source. For a std of 0.15 mm, we calculated an EF of 0.48, which corresponds to a relative increase of almost 10% in comparison to our basic std of 0.45 mm. For a std of 1.5 mm - the highest value under examination - we calculated an EF of 0.30, which corresponds to a relative decrease of approximately 32%. Figure 5.7 shows central lateral profiles of the energy fluency scored for different source sizes.

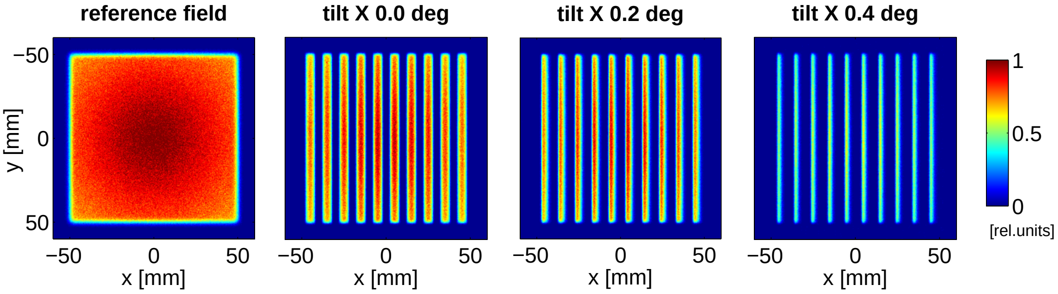

Figure 5.4: Energy fluency maps of MC series a (tilt X) and of the reference field.

5.2.4 Discussion

The primary radiation efficiency of the 2D-bMLC field is especially sensitive to a tilt of the collimator perpendicular to the characteristic stripes of the field (tilt X). Already relatively

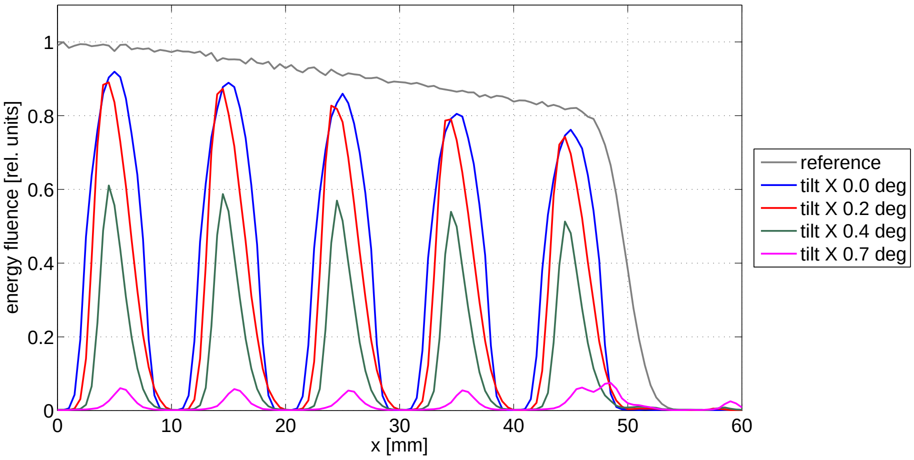

Figure 5.5: Results for MC series a (tilt X). The averaged central lateral profiles of the energy fluency in the isocentric plane is shown. For tilt angles greater than 0.5 degree, cross leakage peaks appear outside the originally collimated field - at x approx. 47.5 and 57.5 mm.

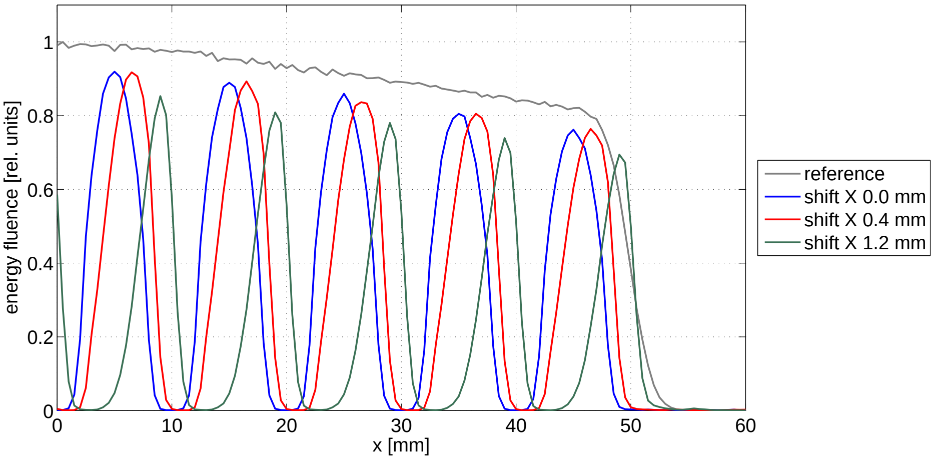

Figure 5.6: Results for MC series c (shift X). The averaged central lateral profiles of the energy fluency in the isocentric plane is shown.

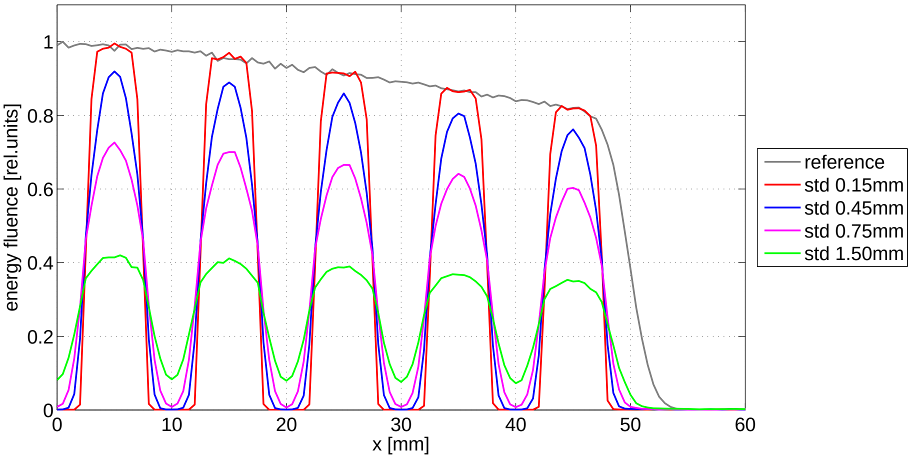

Figure 5.7: Results for MC series f (source size). The averaged central lateral profiles of the energy fluency in the isocentric plane is shown.

small tilt angles lead to a significant decrease in EF, e.g. tilts of 0.1, 0.2 and 0.3 degrees leads to relative decreases in EF of approximately 8%, 25% and 44% respectively. For angles greater than 0.5 degree, the EF was merely about 5% of the EF of the un-tilted 2D-bMLC. Furthermore, at these tilt angles unwanted energy fluency peaks appeared outside the actual field dimensions. These peaks are a result of increased cross leakage through closed absorber channels. Also lateral shifts perpendicular to the collimator slits (shift X) can lead to a significant reduction in the primary radiation efficiency and, in addition, to an unwanted shift of the 2D-bMLC field. EF is much less sensitive to tilts and shifts in parallel to the field stripes as well as to vertical shifts towards the source or away from the source. Finally, in summary, the results show that correct geometrical alignment of the 2D-bMLC is crucial and has to be performed with special care.

Based on geometrical considerations, one could also propose to change the design of the collimator in order to make it at least a bit less sensitive to misalignments. For example the absorber channels could be shortened and or the the source-collimator distance could be increased. However, these changes would also imply undesired consequences, such as increased leakage dose or an increased minimum SAD.

EF also depends on the geometrical width of the photon source that is to say on the electron beam spot on the target of the linear accelerator. To avoid losses in primary efficiency the electron spot size should be as small as possible. Finally, for treatment planning a correct model of the linac source is crucial.

5.2.5 Conclusion

Correct geometrical alignment of the 2D-bMLC is crucial and has to be performed with special care. The primary radiation efficiency is especially sensitive to tilts and shifts perpendicular to the 2D-bMLC-field stripes. Both can cause severe under-dosage. Furthermore, the primary radiation efficiency decreases with increasing source size. A change of the source size can lead to over- or under-dosage.

5.3 Intrafraction Motion

5.3.1 Introduction

Patient motion during delivery of a radiotherapy (RT) fraction, called intrafraction motion, can lead to degradations of the initial treatment plan. Any movements of the patient as well as of the inner organs may cause discrepancies between the planned and the actually delivered doses. First of all, motion typically results in a blurring of the dose distribution. A possible consequence of the blurring is an underdosage at the borders of the target volume. Conventionally, this problem is tackled by adjusting the margins of the planning target volume (PTV) appropriately. However in IMRT, interplay between patient motions and the succesively applied or continuously changing radiation fields may lead to hot and cold spots everywhere within the PTV, and consequently also within the clinical target volume (CTV). These interplay effects depend on the treatment technique and can be very compex. (Bortfeld et al., 2002, 2004; Yu et al., 1998).

2D-bMLC treatment might be notably sensitive to interplay effects, first because the treatments are highly dynamic and secondly because of the striped pattern of the 2D-bMLC fields (see sections 2.3.1 and 3.3.2). In figure 5.8 we give an example for an interplay effect, which may occur because of the spatial fractionation of the radiation fields. The figure should illustrates, why 2D-bMLC treatments might be especially prone to plan degradations induced by intrafraction target motion. Of course, the example is over-simplistic in view of the fact that in practice the 2D-bMLC beams are divergent and the radiation is delivered quasi continuously meanwhile the gantry rotates.

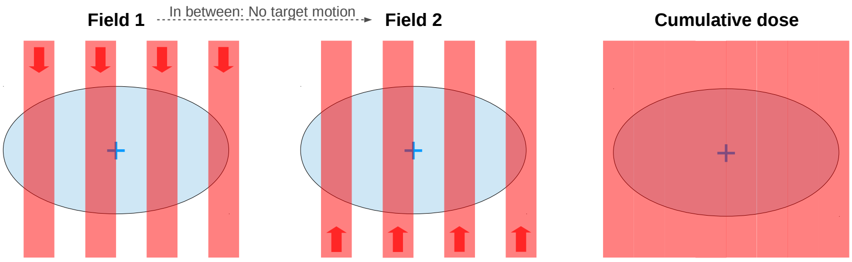

(a) No target motion supposed (initial treatment plan)

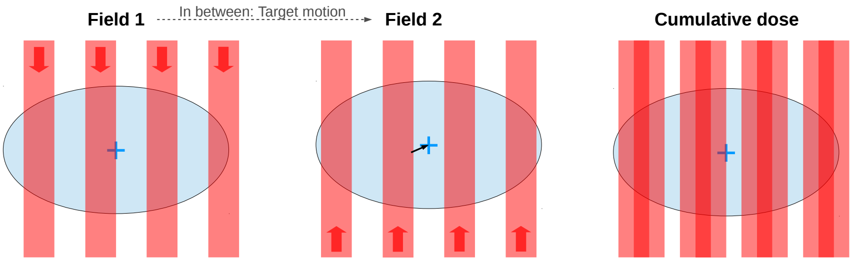

(b) The target has been displaced in between delivery of the fields.

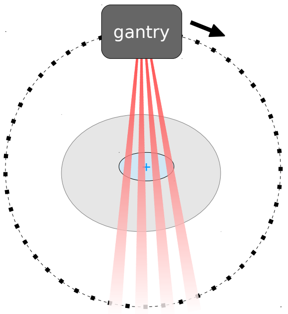

Treatment design

Figure 5.8: Superposition of the dose deposited subsequently by opposing 2D-bMLC fields. Interplay effects can arise, if the target volume is displaced in between the delivery of the two fields. In practice, interplay effects occurring in a 2D-bMLC treatment should be highly complex in view of the fact that radiation is delivered quasi continuously meanwhile the gantry rotates.

This study represents a first investigation of dosimetric consequences of intrafraction motion for 2D-bMLC prostate treatments. Therefore, the 4d MC tool (see section 3.3.3) was extended to continuously modelled body displacements. Such as many other authors, we assumed that the patient moved as a rigid body (Adamson et al., 2011; Bortfeld et al., 2004; Langen et al., 2008a; Li et al., 2008a).

In general, the dosimetric impact of interplay effects is reduced if doses are accumulated over multiple fractions: The interplay effect is averaged out through fractionation[3] (Bortfeld et al., 2002). Dosimetric consequences of intrafraction motion for prostate IMRT, including interplay effects, has been studied by several authors (Adamson et al., 2011; Langen et al., 2008a, 2012; Li et al., 2008b). Consistently, the conclusion was, that significant motions could be observed during individual fractions, but that the cumulative effect for a full treatment course is negligible small.

In this study, we recalculated 2D-bMLC prostate plans with intrafraction motion for both standard fractionation and for extreme hypofractionation. The assessed dose distributions were compared to static reference plans. The applied motion patterns were assessed from data recorded during prostate RT with the Calypso tumor tracking system (Varian Medical Systems, Inc., Palo Alto, CA, USA). The Calypso system uses electromagnetic transponders that are implanted into a tissue of interest. The positions of the transponders are localized and continuously monitored with an antenna that is placed over the patient. If multiple transponders (generally three) are implanted into the prostate, the Calypso system allows the observation of real-time prostate movements during the course of RT (Balter et al., 2005; Kupelian et al., 2007; Langen et al., 2008b; Lin et al., 2013; Schmitt et al., 2010; Willoughby et al., 2006). Calypso localisation data has also already been used for motion-encoded dose reconstruction for prostate treatments (Langen et al., 2012; Li et al., 2008a).

5.3.2 Methods

5.3.2.1 Motion data sets

The tumour motion data sets were assessed from data recorded with the Calypso system during prostate IMRT treatments (the Calypso traces were not recorded for the same patient CTs, that were finally used in the planning study). Three electromagnetic transponders implanted into the prostate were tracked during each treatment fraction respectively. Data acquisition was started after positioning of the patient and several minutes before first beam on. The relevant quantity for our purposes was the mean 3d position of the transponders, from now on referred to as the Calypso position. The acquisition rate of the Calypso position was 10 Hz. For this study the Calypso data sets of two full treatment courses, both with 35 fractions, were used. The recorded IMRT treatments were daily, without treating on weekends.

The Calypso position was used to model the displacement of the prostate during the delivery of 2D-bMLC treatment fractions. We assumed patient setup with the Calypso system and preprocessed the Calypso position fractionwise as follows: For each fraction a delivery start time t_0 was defined as the time of first beam on. Furthermore, a start position was defined as the Calypso position averaged over the 30 s before first beam on. Finally, the 3d displacement from the starting position over time was calculated, starting at t_0.

In this way two motion data sets, each one consisting of the 3d displacement or motion pattern for 35 fractions, were generated. In the following, the data sets are referred to as M1 and M2. The motion patterns associated to a data set are labelled with the letter P and consecutive numbers (e.g. M1 P12 is the pattern number 12 of data set M1). The numbers correspond

---

[3] Strictly speaking this is only true for the physical dose deposition but not for the biologically effective dose. A non-even fractionation can lead to an additional biological effect. However, Bortfeld et al. (2002) showed that this effect is generally negligible.

to the treatment days of the originally recorded IMRT treatment. Two example for motion patterns generated from the Calypso measurements are shown in figure 5.9.

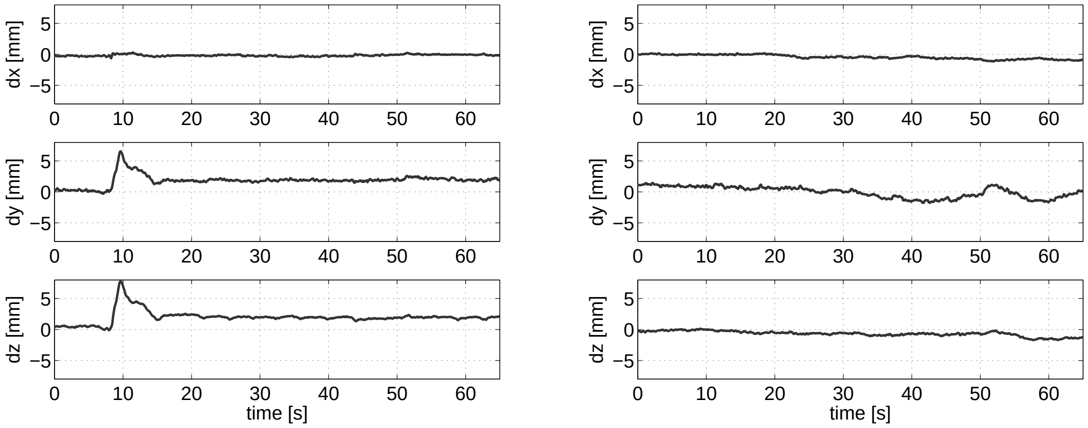

(a) Motion pattern M1 P12

(b) Motion pattern M2 P10

Figure 5.9: Motion patterns generated from measurements with the Calypso tumour tracking system. Two patterns with relatively pronounced intrafraction motion are shown. The displacement components dx, dy and dz are given in the IEC patient system. In anatomical terms of location, dx corresponds to the left/right axis, dy to the inferior/superior axis and dz to the posterior/anterior axis.

5.3.2.2 2D-bMLC plans

The 2D-bMLC plans used for this study, and summarised in table 5.1, have already been presented in chapter 3. For plan Boost (presented in section 3.3.4 as case 2), a multi-focal simultaneous integrated boost concept was applied. The plans F35, F12 and F5 (section 4.4) were all calculated for the same prostate patient but for different fractionation regimens, namely for standard fractionation (F35) and for hypofractionation (F12 and F5). The fractional delivery times $\mathrm{T_F}$ were 20 s for Boost and F35, 40 s for F12 and 65 s for F5.

5.3.2.3 MC dose calculation with intrafraction motion

Each 2D-bMLC plan has been recalculated with the 4d MC tool without motion and with different target motion patterns. In the MC simulations, target motion was modelled by displacement of the treatment target point (TP). In section 3.3.3, the 4d MC dose calculation method, has been described. For this study, the method was extended to time dependent TPs. Therefore, the coordinates of the TP were also described as Time Features. As discussed in detail in section 3.3.3, a function of time, called 'Time Feature', is associated to a simulation quantity, which varies over time. A Time Feature assigns a well-specified value to any specific time within the time range of the simulation.[4]

All MC plan recalculations are listed in table 5.1 in the last column. In the same column we also specify the respectively applied motion patterns. (s) refers to static MC recalculation without motion. (m1) and (m2) refer to full 2D-bMLC treatment courses computed with motion

---

[4] The 4d MC method was also extended to rotations of the patient geometry, although this freature was not used for this study. TP displacements and arbitrary rotations of the patient geometry in the treatment room can both be modelled continuously during the delivery of the 2D-bMLC treatment.

Table 5.1: Plan Boost was presented in section 3.3.4 as case 2. The plans F35, F12 and F5 were presented in section 4.4. Each plan has been recalculated with the 4d MC tool without motion (s) and with different motion pattern. (m1) and (m2) refer to treatment courses computed with patterns of the data sets M1 and M2 respectively. (m1*) is a treatment fraction calculated with M1 P12, the pattern with the highest std of the absolute target point displacement for $\mathrm{T_F}$ 20 s. (d1) and (d2) refer to constant drifts of 5 mm in inferior/superior (IS) and posterior/anterior (PA) direction respectively.

Plan	**Prescription**	$\mathbf{T_F}$	**Series of motion patterns for MC**
Boost	$D_{50\%} \geq$ 34×2.25 Gy (PTV boost) 34×1.50 Gy (PTV LDP)	20 s	(s) static reference (m1) M1 P1–P34 (m2) M2 P1–P34 **Single fractions:** (d1) drift PA (d2) drift IS (m1*) M1 P12 ('worst case' fraction)
F35	$D_{95\%} \geq 35 \times 2.1\,\mathrm{Gy}$	20 s	(s) static reference (m1) M1 P1–P35 (m2) M2 P1–P35
F12	$D_{95\%} \geq 12 \times 4.3\,\mathrm{Gy}$	40 s	(s) static reference (m1) M1 P1–P12 (m2) M2 P1–P12
F5	$D_{95\%} \geq 5 \times 7.25\,\mathrm{Gy}$	65 s	(s) static reference (m1-a) M1 P1, P4, P6, P9, P11 * (m1-b) M1 P2, P5, P7, P10, P12 * (m2-a) M2 P1, P4, P6, P9, P11 * (m2-b) M2 P2, P5, P7, P10, P12 * *Comment: The series correspond to potential treatment schedules with two treatments per week resp.*

patterns of the data sets M1 and M2 respectively. The 2D-bMLC fractions were simulated with the specified patterns separately, and finally, the fraction doses were summed up. Plan F5 is delivered in only five fractions. This plan was recalculated twice for each motion data set, but respectively with different combinations of motion patterns. Overall, the selected pattern numbers correspond to realistic treatment schedules. As mentioned in section 5.3.2.1, the patterns were recorded for daily RT (without weekend). Plans Boost, F35 and F12 would also be delivered daily. Plan F5 would be delivered in two fractions a week following (RTOG, 2013).

For plan Boost, the dose distribution for pattern M1 P12, thus for a single treatment faction, was evaluated separately (m1* in table 5.1). This is the motion pattern with the overall highest std of the absolute TP displacement (see section 5.3.2.4) for $\mathrm{T_F}$ 20 s. Additionally, treatments fractions with constant drifts of the TP were simulated for the same plan (d1 and d2 in table 5.1). Within the delivery time of 20 s, the TP was shifted with constant speed by 5 mm in superior/inferior (IS) or in posterior/anterior (PA) direction respectively. The shift was performed from -2.5 mm to +2.5 mm in the respective direction and relative to the initially planned TP.

$\overline{F}_{d>0.5d_{\max}}$ of all evaluated MC dose distributions was about 1%, whereas $\overline{F}_{d>0.5d_{\max}}$ is the fractional uncertainty in the average dose for voxels with dose values greater than 50% of the maximum dose (Chetty et al., 2007). The dose distributions were evaluated by means of visual inspection and qualitative and quantitative DVH analysis. In this study, both PTV and CTV doses were evaluated. Of course, the critical evaluation is that for the CTVs. The CTV to PTV margin is the current management technique for interfraction and intrafraction motion. Hence, degradations of the CTV doses should be prevented, but degradations of the PTV doses might be allowed and are even expected.

5.3.2.4 Measure of motion

As measure of TP motion, the standard deviation of the absolute TP displacement was assessed for each simulated treatment fraction and for each full treatment course. The displacement pattern, which have been assessed from experimental data, are available as discrete data series: displacement vectors (dx_i, dy_i, dz_i) are assigned to the time points t_i, which are sampled in steps of 0.1 s starting at 0 s. The absolute displacement at time t_i is given by

$$d_i = \left(dx_i^2 + dy_i^2 + dz_i^2\right)^{\frac{1}{2}} \quad . \tag{5.1}$$

The following textbook definition was used to calculate the std of a sample of absolute displacements d_i:

$$std = \left(\frac{1}{n-1}\sum_{i=1}^{n}(d_i - \bar{d})^2\right)^{\frac{1}{2}} \tag{5.2}$$

where

$$\bar{d} = \frac{1}{n}\sum_{i=1}^{n} d_i \tag{5.3}$$

and n is the number of elements in the sample. With equation 5.2, the standard deviation can be assessed for all displacements modelled either in a single treatment fraction or in a full treatment course, thus in a series of fractions. From now on, the standard deviation for a single fraction is simply referred to as *std*, whereas the standard deviation for a full treatment course is referred to as *STD*.

We want to emphasize, that the values of *std* or *STD* depend on the selected motion patterns as well as on the delivery time T_F, and *STD* is furthermore directly affected by the number of evaluated fractions. *std* and *STD* are proposed as metrics for the modelled motion. However, these quantities cannot directly be correlated with physical properties. In this study, we will only make comparisons between values of *std* or *STD*, which were assessed for well defined T_F and the same number of fractions.

std was also assessed for the constant drifts (d1) and (d2). Therefore, the drifts were described by a series of displacement vectors sampled in steps of 0.1 s between 0 s and T_F.

5.3.3 Results

5.3.3.1 Measure of motion

In figure 5.10, a bar plot is shown for each motion-encoded calculated treatment course. The plots illustrate the distributions of *std* respectively. The values of *STD* are given in grey boxes, which are added to each plot. As mentioned in section 5.3.2.4, we only make comparisons between values assessed for the same T_F and the same number of fractions.

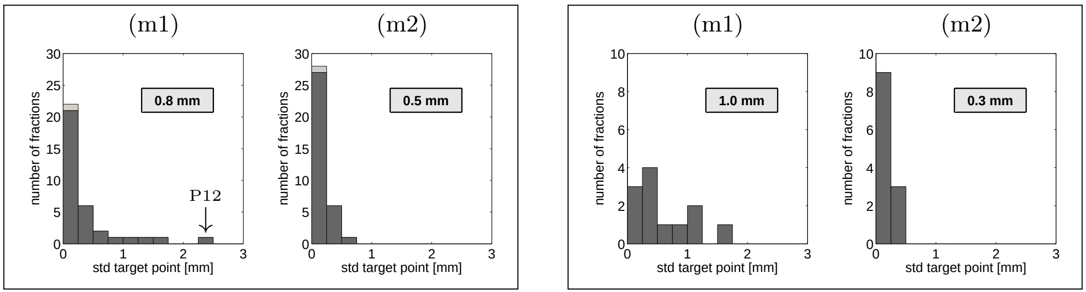

(a) Boost & F35 - F35 has one additional count in the first bin.

(b) F12

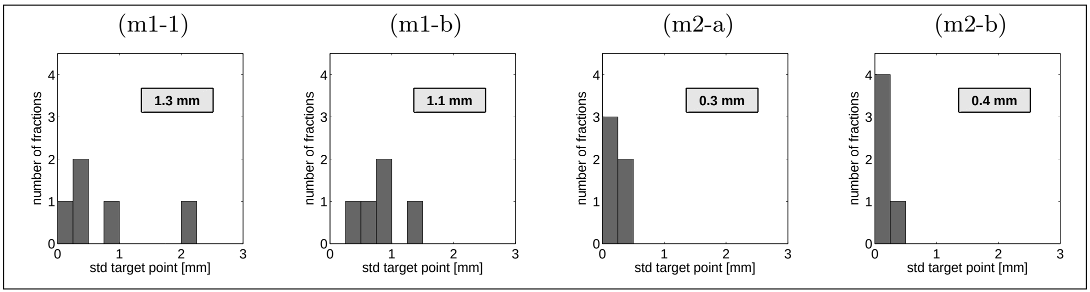

(c) F05

Figure 5.10: Standard deviation of the TP displacement. The values in the grey boxes are *STD* assessed for full treatment courses. The bar plots show the distributions of *std* assessed for individual treatment fractions. Boost and F35 are delivered in 35 fractions with T_F 20 s, F12 in 12 fractions with T_F 45 s and F5 in 5 fractions with T_F 60 s. More details about the treatment plans and the applied motion patterns are given in table 5.1. The arrow in (a) points at the 'worst case' pattern M1 P12.

The plans Boost and F35 were both calculated for $T_F = 20$ s. The same two series of motion patterns (m1 and m2) were used for MC recalculation, whereas Boost was delivered in 34 and F35 in 35 fractions. Finally, the bar plots (figure 5.10(a)) are very similar for both plans with the sole difference of one count in the first bin. Comparing the to series, overall more higher values of *std* have been assessed for series (m1). The highest value for (m2) is 0.6 mm, all other 35 values are below 0.5 mm. In comparison, for series (m1) seven values are above 0.5 mm and 4 values above 1.0 mm. The by far highest value of 2.5 mm was assessed for fraction 12 of (m1), respectively for motion pattern M1 P12. This fraction is also referred to as the 'worst case' fraction related to intrafraction motion for $T_F = 20\,s$. As already mentioned in section 5.3.2.3, this is also the fraction, for which the dose distribution was evaluated separately in the case of plan Boost.

In figure 5.10(a) and 5.10(b), we show the bar plots for the plans F12 and F5 with T_F of 40 and 65 s respectively. Again, overall higher values of *std* and *STD* were assessed for the series of motion patterns (m1), respectively (m1-a) and (m1-b) for F5.

5.3.3.2 Plan Boost

The quantitative DVH analysis for plan BOOST is shown in table 5.2. All dose values are given relative to the prescription dose 76.5 Gy for the primary PTV (PTV boost). In the first column of the table, the parameters assessed for the static reference plan (s) are given. In the other columns of table 5.2, we report the DVH parameters for the MC calculations with intrafraction motion. Differences to the static reference plan (s), which were seen as relevant, are encircled.

The DVH parameters assessed for the cumulative dose distributions are very similar to those for the static reference. Overall, no relevant differences between the dose distribution calculated with and without intrafraction motion can be reported, neither from DVH analysis nor from visual inspection.

On the contrary, the distribution calculated for the so called 'worst case' fraction (m1*) show relatively large deviations from the static reference plan (s), especially for the primary target (boost): The coverage of CTV boost was reduced to 88% compared to 100% as calculated for the static plan. The minimum dose $D_{98\%}$ was reduced by 6% and the maximum dose $D_{2\%}$ was increased by 8%. The target dose uniformity index was increased from 1.06 to 1.16. For the considerably larger CTV LDP (the PTV volumes are given in table 3.1) the dose coverage was reduced by 7%. Finally, $D_{2\%}$ to the rectum was relatively increased by about 4%. In figure 5.11(a), we show plots of the DVHs for the CTVs and the PTVs.

In table 5.2, we also give the results for the treatment fractions calculated with constant TP drifts. The drift in PA direction (d1) lead to expansive dosimetric consequences in the range of those reported for (m1*). Again, in the first instance the CTV doses were affected, as can also be seen in the DVH plot in figure 5.11(b). The drift in IS direction (d2) did not lead to relevant plan degradations. In fact, the coverage of PTV boost was reduced by 3%. However, the DVH parameters assessed for the CTVs and the OARs were very similar to those of the reference plan.

In figure 5.12, we compare dose distributions for the reference (s), the drift in PA direction (d1) and the 'worst case' fraction (m1*). Two slices with contours of PTV boost are shown: Slice 40 represents a centrally located cut through the volume; slice 47 is located at the superior edge of PTV boost. On both slices, one can clearly see the dose inhomogeneities within PTV boost introduced by the modelled motions: The dose distributions of (d1) and (m1*) are characterised by a ring-like pattern. For (m1*), we noticed an additional overall reduction in the doses to PTV boost on slice 47. However, CTV boost did not extend into slice 47 and was not considerably affected by this dose reduction at the PTV edge.

5.3.3.3 Plans F35, F12 and F5

In table 5.3(a) to (c) we show the DVH parameters assessed for the treatment plans F35, F12 and F5 respectively. Differences to the static reference plan (s), which were seen as relevant, are encircled. For F35 with 35 fractions and T_F 20 s, no relevant differences could be observed

Table 5.2: DVH analysis for plan Boost. The plan has been calculated with the 4d MC tool without motion (s) and with motion patterns as described in table 5.1. Dose values are given relative to the prescription dose for PTV boost (76.5 Gy resp. 2.25 Gy fraction dose). DVH parameters are defined in section 3.3.4.

		cumulative		*single fractions*		
	(s)	**(m1)**	**(m2)**	**(m1*)**	**(d1)**	**(d2)**
std [mm]	0.0	0.8	0.5	2.5	1.5	1.5
PTV boost						
$D_{98\%}$ [%]	94	93	94	79	89	93
$D_{98\%}$ [%]	104	104	104	110	111	104
$V_{95\%}$ [%]	95	95	95	75	80	92
UI	1.09	1.09	1.09	1.29	1.20	1.10
CTV boost						
$D_{98\%}$ [%]	97	97	97	91	89	96
$D_{2\%}$ [%]	104	104	104	112	113	104
$V_{95\%}$ [%]	100	100	100	88	84	100
UI	1.06	1.06	1.06	1.18	1.21	1.07
PTV LDP						
$D_{98\%}$ [%]	61	61	61	59	60	61
$D_{2\%}$ [%]	101	101	101	103	103	101
$V_{95\%}$ [%]	95	95	95	87	90	94
UI	1.56	1.55	1.56	1.58	1.57	1.56
CTV LDP						
$D_{98\%}$ [%]	64	64	64	62	62	63
$D_{2\%}$ [%]	102	102	102	104	104	102
$V_{95\%}$ [%]	99	99	99	92	94	98
UI	1.55	1.55	1.55	1.59	1.58	1.56
Rectum						
$D_{2\%}$ [%]	95	95	95	99	96	95
D_{mean} [%]	43	43	43	45	43	43
Bladder						
$D_{2\%}$ [%]	102	102	102	100	105	101
D_{mean} [%]	51	52	52	47	51	51

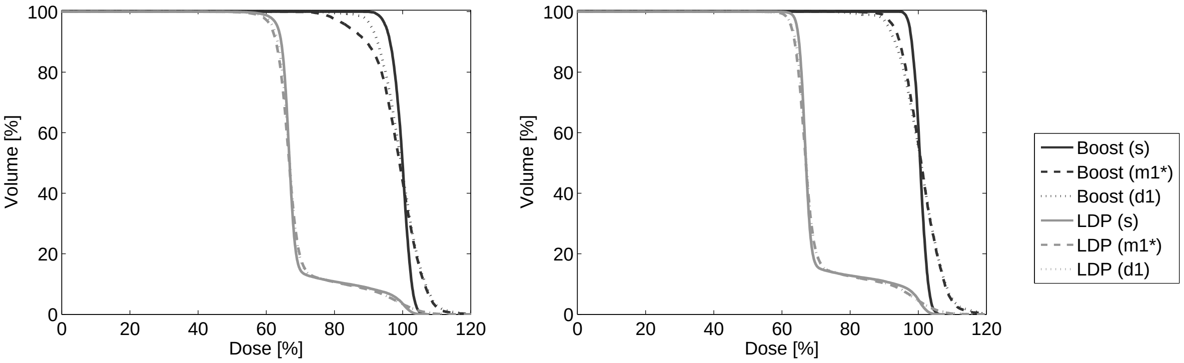

(a) Planning target volume (PTV)

(b) Clinical target volume (CTV)

Figure 5.11: DVHs for fractions of plan Boost. The DVHs for (m1*) and (d1) are shown in comparison to the static plan (s). Dose values are given relative to the prescription dose for PTV boost.

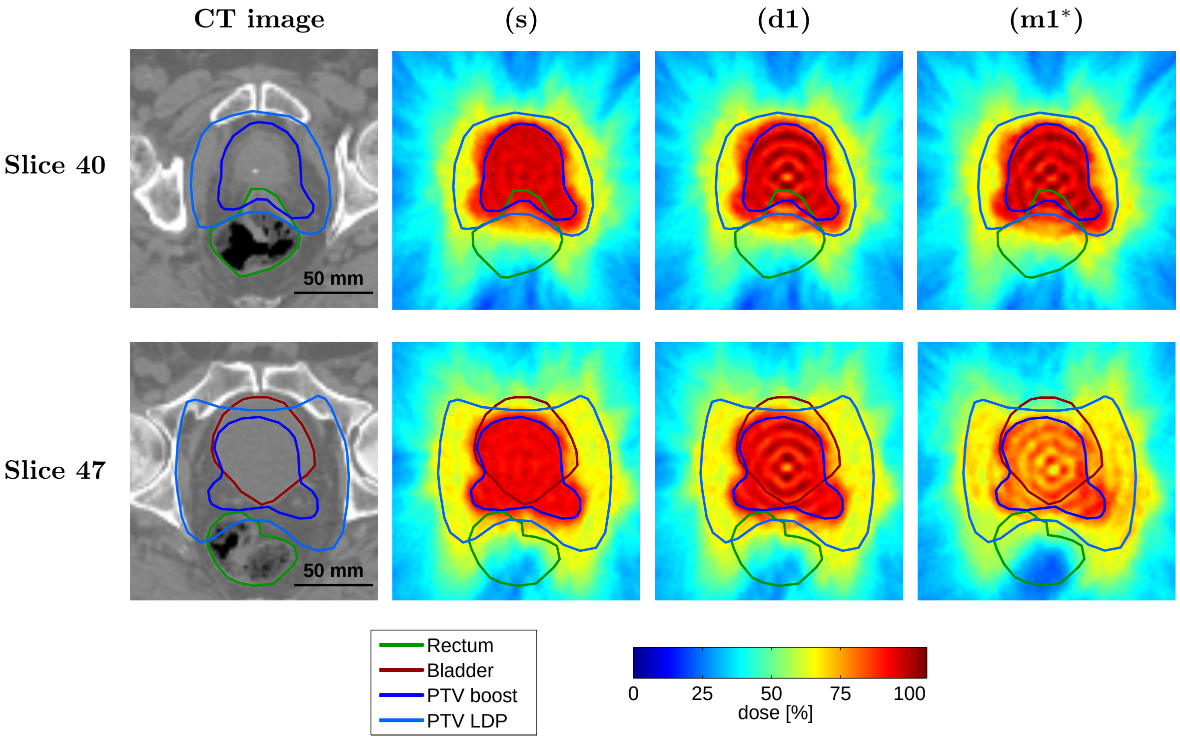

Figure 5.12: Dose maps for treatment fractions of Boost calculated without motion (s) with a constant drift in PA direction (d1) and with motion pattern M1 P12 (m1*). The superior edge of PTV boost is shown on slice 47. The slice thickness is 2 mm. Dose values are shown relative to the prescription for PTV boost. More details about the treatment plans and the applied motion patterns are given in table 5.1.

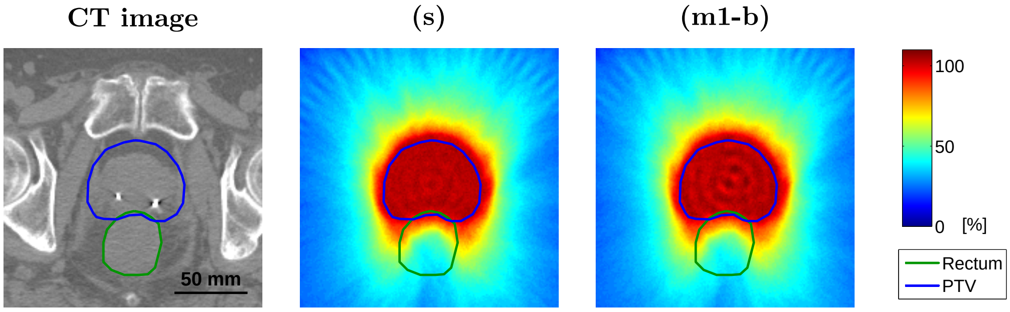

(a) Full treatment course: Accumulated dose maps for F5(m1-b) and for the static reference F5(s).

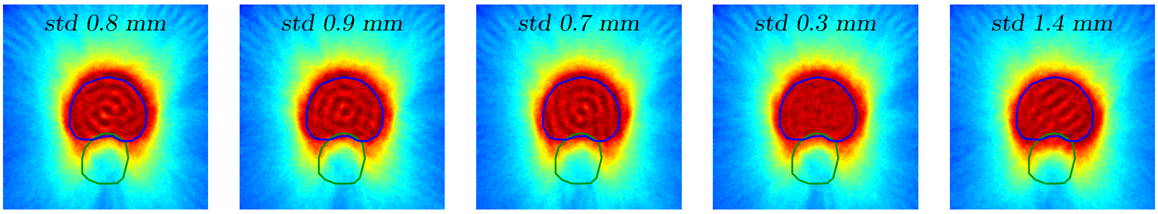

(b) Fractions 1–5 of plan F5 (m1-b). Each fraction was calculated with a different motion pattern.

Figure 5.13: MC calculated dose maps for plan F5. All doses are shown relative to the prescription dose, 7.25 Gy per fraction or 36.25 Gy for the full treatment course respectively. More details about the treatment plans and the applied motion patterns are given in table 5.1.

between the treatment courses calculated with intrafraction motion, (m1) and (m2), and the reference (s). This is true for DVH analysis and visual inspection of the dose distributions. In the case of plan F12 with 12 fractions and T_F 40 s, variations in the DVH parameters reported for the CTV and the OARs are below 1%.

Treatment plan F5 was delivered in only 5 fractions and with a T_F of 65 s. With intrafraction motion considered CTV coverage was between 94% for (m1-b) and 98% for (m2-a), compared to 99% for (s). The target dose uniformity index - 1.05 for (s) - was slightly increased by the motion, with the highest value of 1.08 for (m1-b). Overall for plan F5, (m1-b) was the recalculation with the most critical deviations from the static reference. In figure 5.13 we show dose distributions for F5(m1-b) and (s). The respective DVHs for the PTV and the CTV are shown in figure 5.14.

Relevant differences concerning doses to the OARs between the references (s) and the respective recalculations with motion could not be found, neither for F35, nor for the hypofractionated plans F12 and F5.

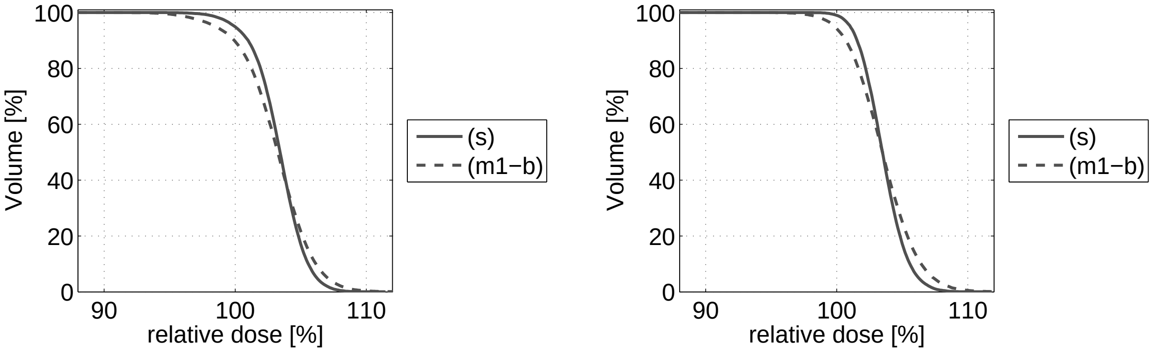

(a) Planning target volume (PTV)

(b) Clinical target volume (CTV)

Figure 5.14: DVHs for plan F05: (m1-b) vs. (s). All doses are shown relative to the prescription dose 36.25 Gy. More details about the treatment plans and the applied motion patterns are given in table 5.1.

5.3.4 Discussion

Selection of motion patterns

Before going into the discussion of the results, we add a comment about the selection of the motion patterns. As explained in detail in section 5.3.2.1, the patterns were generated from real patient data recorded with the Calypso tumour tracking system during radiotherapy treatments. Overall, Calypso data of more than 30 patient cases was available. For this study we selected two data sets with relatively pronounced intrafraction motions within the first several minutes after first beam on. The selection was based on visual inspection of the displacement curves and not on a quantitative analysis. Certainly, only a limited number of cases was investigated in this study. However, the results should provide a first insight into possible problems with intrafraction motion for 2D-bMLC treatments.

Individual treatment fractions (and occurring interplay effects)

The MC dose distribution of individual treatment fractions calculated with intrafraction motion can deviate significantly from the planned doses. This has been shown by the example of the

Table 5.3: DVH analysis for prostate plan F35, F12 and F5. Doses are shown relative to the prescription doses 73.5 Gy, 51.0 Gy and 36.25 Gy resp. The plans have been calculated with the 4d MC tool without motion (s) and with motion patterns as described in table 5.1. DVH parameters are defined in section 3.3.4.

(a) Plan F35: 35 fractions, T_F 20 s

	(s)	**(m1)**	**(m2)**
std [mm]	0.0	0.8	0.5
PTV			
$D_{98\%}$ [%]	99	98	99
$D_{2\%}$ [%]	109	108	109
$V_{100\%}$ [%]	95	95	95
UI	1.08	1.08	1.08
CTV			
$D_{98\%}$ [%]	100	100	100
$D_{2\%}$ [%]	109	109	109
$V_{100\%}$ [%]	98	98	98
UI	1.07	1.07	1.07
Rectum			
$D_{2\%}$ [%]	97	97	97
D_{mean} [%]	33	33	33
Bladder			
$D_{2\%}$ [%]	103	103	103
D_{mean} [%]	14	14	14

(b) Plan F35: 35 fractions, T_F 20 s

	(s)	**(m1)**	**(m2)**
std [mm]	0.0	1.0	0.3
PTV			
$D_{98\%}$ [%]	99	98	98
$D_{2\%}$ [%]	107	107	108
$V_{100\%}$ [%]	95	94	94
UI	1.07	1.07	1.07
CTV			
$D_{98\%}$ [%]	100	100	99
$D_{2\%}$ [%]	108	107	108
$V_{100\%}$ [%]	98	99	97
UI	1.06	1.05	1.07
Rectum			
$D_{2\%}$ [%]	97	96	97
D_{mean} [%]	34	34	34
Bladder			
$D_{2\%}$ [%]	103	103	103
D_{mean} [%]	13	14	14

(c) Plan F5: 5 fractions, T_F 65 s

	(s)	**(m1-a)**	**(m1-b)**	**(m2-a)**	**(m2-b)**
std [mm]	0.0	1.3	1.1	0.3	0.4
PTV					
$D_{98\%}$ [%]	99	98	97	98	98
$D_{2\%}$ [%]	107	108	108	107	108
$V_{100\%}$ [%]	95	91	90	94	93
UI	1.06	1.08	1.09	1.07	1.07
CTV					
$D_{98\%}$ [%]	100	99	99	100	99
$D_{2\%}$ [%]	107	108	109	107	108
$V_{100\%}$ [%]	99	95	94	98	96
UI	1.05	1.07	1.08	1.06	1.07
Rectum					
$D_{2\%}$ [%]	97	97	97	97	97
D_{mean} [%]	36	35	36	35	35
Bladder					
$D_{2\%}$ [%]	103	102	102	103	103
D_{mean} [%]	13	14	13	13	14

’worst case’ fraction (m1*) for plan Boost. As can be seen in figure 5.12, the motion lead to undesired dose inhomogeneities within the target volumes, most notably within the primary target volume (PTV resp. CTV boost). The dosimetric consequences can be observed in the DVHs shown in figure 5.11(a) and in the DVH parameters presented in table 5.2.

The reference dose distributions shown in figure 5.12 are rather flat within PTV boost. On the contrary, the dose distributions of (m1*) are characterized by a distinctive ringlike pattern in the same region. The pattern araised around the axis of rotation of the 2D-bMLC treatment, which is directed according to the normal of the shown slices and goes through the initially planned TP (The TP was set close to the 3d center of PTV boost). We suppose that the ring-shaped inhomogeneities are caused by interplay effects such as those which were mentioned in the introduction in section 5.3.1 and for which an over-simplistic example was illustrated in figure 5.8.

We further suppose that these inhomogeneities are primarily induced by displacements perpendicular to the axis of rotation, thus in PA or LR direction. This latter supposition is based on the principal geometry of the 2D-bMLC treatments, in particular on the orientation of the collimator according to the direction of gantry rotation (see section 3.3.1). The MC recalculations (d1) and (d2) of plan Boost were performed to confirm the supposition. In simulation (d1), a constant drift of the TP in PA direction was modelled during delivery. Consequently, this was an example of displacement perpendicular to the axis of rotation. Dose distributions of (d1) are also shown in figure 5.12. The drift lead to inhomogeneities in the dose distributions similar to those observed for (m1*). In simulation (d2), we modelled a constant drift in IS direction, thus in parallel to the axis of rotation. The drift did not cause distinctive dose inhomogeneities.

Although displacements in IS direction might not lead to severe interplay effects, it is obvious that they may cause insufficient target coverage at the superior and or the inferior extremity of the PTV. Again, case (m1*) gives an example for this effect. On slice 47, at the superior edge of PTV boost, we observe an overall unintentional reduction of the dose. This reduction has also considerably contributed to the divergence of the PTV boost DVHs of (m1*) and (s), which can be seen in figure 5.11(a). Finally, this dose reduction at the PTV edge did not considerably affect the CTV doses.

A detailed analysis of individual treatment fractions was only performed for plan Boost and for the discussed cases. However, here we also refer to figure 5.13(b). In the figure, we show MC dose distributions calculated with intrafraction motion for the 5 treatment fractions of plan F5 (T_F 65 s). The statistical uncertainty of the MC simulations did not allow fractionwise quantitative evaluation. However, we can observe further examples for dose inhomogeneities within the target caused by intrafraction motion. Again ring-shaped textures are visible, in three of the five shown dose maps.

Full treatment courses

The discussed inhomogeneities induced by intrafraction motion might appear dramatic, if dose distributions of individual treatment fractions are analysed alone. Therefore, it is interesting to take a closer look to the dose distributions accumulated over the full treatment courses. They were assessed by summing up the ‘fractional’ dose distributions. This simple method of dose accumulation was justified, because the MC calculations for one treatment course were all performed with the same rigid patient geometry respectively. Only the patterns of (rigid) body motion changed from fraction to fraction.

The plans Boost and F35 were both calculated for standard fractionation regimens and were delivered in 34 and 35 fractions respectively. T_F was 20 s in both cases. Based on the analysis of the accumulated doses for these two plans, we could not observe any plan degradations induced by intrafraction motion. The motion in the ‘worst case’ fraction discussed above was exceptionally pronounced. The value of *std* for this fraction was by far the highest value assessed for $T_F = 20\,s$. Most of the other values were considerably smaller as can be seen in figure 5.10(a). Therefore, the dose inhomogeneities induced during the other fractions were certainly less critical. In any case the inhomogeneities, including those of the ‘worst case’ fraction, were finally averaged out in the accumulation over 34 respectively 35 treatment fractions. Overall, in the case of standard fractionation the dosimetric consequences in the accumulated dose distributions seem to be as small as those reported for other IMRT techniques by Langen et al. (2008a, 2012) or Li et al. (2008b).

F12 and F5 were both hypofractionated treatment plans. The treatments were delivered in less fractions (12 and 5 resp.) but with higher doses per fraction (4.3 and 7.25 Gy resp.). We therefore expected that dose inhomogeneities, induced in single treatment fractions, should carry more weight in the dose distribution for the full treatment course. The lower the number of fractions, the more unlikely it should be that the inhomogeneities are averaged out. The differences were still comparatively small for F12. Variations in the DVH parameters reported for the CTV and the OARs were below 1%. However, in the case of plan F5, the dose distributions calculated with intrafraction motion did indeed show significant differences from the respective reference distributions. The CTV coverage was reduced by 1-4%. Moreover, the PTV uniformity index UI was increased in all calculations with motion, albeit the increase was relatively moderate. An increase in UI is evidence of enhanced dose inhomogeneity within a target volume.

5.3.5 Conclusion

A model for rigid patient motion was successfully added to the time-dependent MC method used for recalculation of 2D-bMLC treatments. The motion was modelled continuously during treatment delivery. The method was used for the recalculation of prostate plans with clinically recorded intrafraction motion patterns. Doses calculated for individual treatment fractions did show distinctive deviations from the planned doses if intrafraction motion was considered. However, in the case of standard fractionation and hypofractionation with 12 fractions, no significant deviations could be observed for the doses accumulated over all fractions. Moderate plan degradation was induced in the case of extreme hypofractionation with only 5 fractions.

Chapter 6

Summary and Conclusion

In this thesis, a novel collimator concept called the 2D-binary multileaf collimator (2D-bMLC) was presented. The principal idea of the concept, which is specially dedicated to fast rotational radiotherapy treatments, was to arrange absorber channels side by side in a 2D matrix to form a radiation collimator. Individual control of each channel should allow for especially quick aperture changes. To explore the capabilities of the concept a medical linac equipped with a 2D-bMLC was modelled and a treatment planning framework for 2D-bMLC treatments was developed.

A detailed description of the 2D-bMLC design and the modelled treatment machine can be found in chapter 2. The X-ray source of a modern flattening filter free medical linac was modelled as well as an exemplary 2D-bMLC with 30 by 30 channels and a maximum field-size of 30 by 30 cm^2 in the isocentric plane. Because half of the radiation is always blocked in each channel, the 2D-bMLC fields are inherently characterised by a striped pattern. In chapter 2, we also presented the dosimetric model of the treatment machine that was successfully established with a Monte-Carlo (MC) method. The primary radiation efficiency of the open 2D-bMLC was 43%, the leakage of the closed one below 0.5%. Abutting bixel exhibited a slight tongue-and-groove effect if opened sequentially. However, the effect was less pronounced than similar tongue-and-groove effects exhibited by conventional MLCs. The equations presented in section 2.B.2 can be used to calculate theoretical projections of individual channel beams.

The planning framework for fast rotational 2D-bMLC treatments (chapter 3) is composed of two individual tools. The optimization tool uses a newly developed method for inverse plan optimization. The second tool is a MC framework for exact calculation of the dose. For the latter, a time-dependent MC method was implemented and a realistic model of the collimator and gantry dynamic was included in the dose calculation. In order to test, if the 2D-bMLC concept is in principal adequate for radiotherapy treatments a planning comparison was performed for 5 different clinical indications. The 2D-bMLC plans fulfilled the clinical goals, and dosimetric parameters were comparable to those of clinically approved Tomotherapy plans. With a maximum dose rate of 2000 MU/min the scheduled delivery times of the 2D-bMLC treatments were between 20 and 25 s.

The planning framework optimizes 2D-bMLC plans for one gantry rotation and for a pre-defined fractional delivery time ($\mathrm{T_F}$). In order to examine in depth the influence of the delivery time onto the final dose distribution, an additional planning study was performed. The study showed that, below a critical $\mathrm{T_F}$, the target dose coverage drops down to a not clinical acceptable level. However, above this value coverage was rather independent on $\mathrm{T_F}$. Furthermore, the potential to spare the organs at risk was partly increased with accepting longer $\mathrm{T_F}$. Finally, a shorter delivery time can lead to inferior optimisation results, and we concluded that a careful weighing up of shorter delivery time and better plan quality might be necessary for each clinical indication or even each patient geometry.

The 2D-bMLC radiation fields are spatially fractionated into stripes and are formed by long and thin absorber channels. Because of this special design, it could be speculated that 2D-bMLC treatments might be notably sensitive to geometrical misalignments of the collimator on the one hand, and to intrafraction motion on the other hand. Both aspects have been investigated in the MC studies presented in the last chapter of this thesis. The first study showed that the misalignment of the 2D-bMLC can in fact cause severe under-dosage. The results suggest, that especially high demands on manufacture tolerances as well as on quality assurance will be necessary, if a 2D-bMLC should be produced for clinical use. For the second study, the MC tool was extended, so that rigid patient motion could be modelled continuously during radiotherapy delivery. The new feature was used for the motion-encoded recalculation of standard and of hypofractionated prostate plans. In the case of standard fractionation and hypofractionation with 12 fractions, no significant plan degradation due to the motion could be observed. Moderate plan degradation was induced in the case of extreme hypofractionation with only 5 fractions.

Outlook

The work presented in this thesis showed that in principal the 2D-bMLC concept could be used for fast rotational radiotherapy treatments with photons. In our opinion the most essential questions that need to be answered next are, if the concept can be translated into the practice, and if the high requirements on geometrical and mechanical precision can be fulfilled. The future of the concept now depends on the answer to these questions.

Bibliography

J. Adamson, Q. Wu, and D. Yan. Dosimetric effect of intrafraction motion and residual setup error for hypofractionated prostate intensity-modulated radiotherapy with online cone beam computed tomography image guidance. *International Journal of Radiation Oncology*Biology*Physics*, 80(2):453–461, June 2011.

S. Agostinelli et al. Geant4 - simulation toolkit. *Nuclear Instruments and Methods in Physics Research Section A: Accelerators, Spectrometers, Detectors and Associated Equipment*, 506 (3):250–303, July 2003.

F. Alongi, L. Cozzi, S. Arcangeli, C. Iftode, T. Comito, E. Villa, F. Lobefalo, P. Navarria, G. Reggiori, P. Mancosu, E. Clerici, A. Fogliata, S. Tomatis, G. Taverna, P. Graziotti, and M. Scorsetti. Linac based SBRT for prostate cancer in 5 fractions with VMAT and flattening filter free beams: preliminary report of a phase II study. *Radiation Oncology*, 8(1):171, 2013.

G. Altenstein, S. Nill, J. Heller, O. Heid, and U. Oelfke. Concept and monte carlo evaluation of a novel 2D binary collimator for fast rotational IMRT. *Radiotherapy and Oncology*, 103: S95–S96, May 2012a.

G. Altenstein, S. Nill, J. Heller, O. Heid, and U. Oelfke. A novel 2D binary collimator for IMRT dose delivery: dosimetric characterization using monte carlo simulations. *Physics in Medicine and Biology*, 57(19):N345–N364, Oct. 2012b.

G. Altenstein, S. Nill, and U. Oelfke. Monte carlo study of the influence of geometrical misalignment of a novel 2d binary collimator on the primary radiation efficiency. In *Abstractband der 43. Jahrestagung der Deutschen Gesellschaft für Medizinische Physik*, pages 595–598. Deutsche Gesellschaft für Medizinische Physik, DGMP, 2012c.

G. Altenstein, S. Nill, and U. Oelfke. Ultra-fast rotational IMRT with a 2d binary collimator: A treatment plan comparison study. *Radiotherapy and Oncology*, In Press, 2013a.

G. Altenstein, S. Nill, F. Sterzing, and U. Oelfke. Comparison of fast rotational IMRT with a 2d binary multileaf collimator (2D-BMLC) with helical tomotherapy (HT). *Medical Physics*, 40(6):86, 2013b.

G. Altenstein, S. Nill, D. Schmitt, F. Sterzin, and U. Oelfke. Fast rotational IMRT with a 2d binary mlc (2D-bMLC): Dosimetric consequences of intrafraction prostate motion. *Radiotherapy and Oncology*, In Press, 2014.

T. Aso, A. Kimura, S. Kameoka, K. Murakami, T. Sasaki, and T. Yamashita. GEANT4 based simulation framework for particle therapy system. pages 2564–2567. IEEE, 2007.

J. M. Balter, J. N. Wright, L. J. Newell, B. Friemel, S. Dimmer, Y. Cheng, J. Wong, E. Vertatschitsch, and T. P. Mate. Accuracy of a wireless localization system for radiotherapy. *International Journal of Radiation Oncology*Biology*Physics*, 61(3):933–937, Mar. 2005.

J. L. Bedford. Treatment planning for volumetric modulated arc therapy (VMAT). In R. Magjarevic, O. Dössel, and W. C. Schlegel, editors, *World Congress on Medical Physics and Biomedical Engineering, September 7 - 12, 2009, Munich, Germany*, volume 25/1, pages 45–48. Springer Berlin Heidelberg, Berlin, Heidelberg, 2009.

T. Bortfeld. IMRT: a review and preview. *Physics in Medicine and Biology*, 51(13):R363–R379, July 2006.

T. Bortfeld, J. Bürkelbach, R. Boesecke, and W. Schlegel. Methods of image reconstruction from projections applied to conformation radiotherapy. *Physics in Medicine and Biology*, 35 (10):1423–1434, Oct. 1990.

T. Bortfeld, W. Schlegel, and B. Rhein. Decomposition of pencil beam kernels for fast dose calculations in three-dimensional treatment planning. *Medical Physics*, 20(2):311–318, 1993.

T. Bortfeld, K. Jokivarsi, M. Goitein, J. Kung, and S. B. Jiang. Effects of intra-fraction motion on IMRT dose delivery: statistical analysis and simulation. *Physics in Medicine and Biology*, 47(13):2203–2220, July 2002.

T. Bortfeld, S. Jiang, and E. Rietzel. Effects of motion on the total dose distribution. *Seminars in Radiation Oncology*, 14(1):41–51, Jan. 2004.

A. Brahme. Optimization of stationary and moving beam radiation therapy techniques. *Radiotherapy and Oncology*, 12(2):129–140, June 1988. ISSN 01678140.

D. J. Brenner and E. J. Hall. Fractionation and protraction for radiotherapy of prostate carcinoma. *International Journal of Radiation Oncology*Biology*Physics*, 43(5):1095–1101, Mar. 1999.

R. H. Byrd, P. Lu, J. Nocedal, and C. Zhu. A limited memory algorithm for bound constrained optimization. *SIAM Journal on Scientific Computing*, 16(5):1190–1208, Sept. 1995.

A. R. Cabrera and W. R. Lee. Hypofractionation for clinically localized prostate cancer. *Seminars in Radiation Oncology*, 23(3):191–197, July 2013.

J. Cashmore. The characterization of unflattened photon beams from a 6 MV linear accelerator. *Physics in Medicine and Biology*, 53(7):1933–1946, Apr. 2008.

I. J. Chetty, B. Curran, J. E. Cygler, J. J. DeMarco, G. Ezzell, B. A. Faddegon, I. Kawrakow, P. J. Keall, H. Liu, C.-M. C. Ma, D. W. O. Rogers, J. Seuntjens, D. Sheikh-Bagheri, and J. V. Siebers. Report of the AAPM task group no. 105: Issues associated with clinical implementation of monte carlo-based photon and electron external beam treatment planning. *Medical Physics*, 34(12):4818, 2007.

M. Dalaryd, G. Kragl, C. Ceberg, D. Georg, B. McClean, S. af Wetterstedt, E. Wieslander, and T. Knöös. A monte carlo study of a flattening filter-free linear accelerator verified with measurements. *Physics in Medicine and Biology*, 55(23):7333–7344, Dec. 2010. PMID: 21081829.

Y. Dzierma, N. Licht, F. Nuesken, and C. Ruebe. Beam properties and stability of a flattening-filter free 7 MV beamâAn overview. *Medical Physics*, 39(5):2595, 2012.

C. Fiorino, I. Dell'Oca, A. Pierelli, S. Broggi, E. D. Martin, N. D. Muzio, B. Longobardi, F. Fazio, and R. Calandrino. Significant improvement in normal tissue sparing and target coverage for head and neck cancer by means of helical tomotherapy. *Radiotherapy and Oncology*, 78(3):276–282, Mar. 2006.

M. Fippel, F. Haryanto, O. Dohm, F. Nüsslin, and S. Kriesen. A virtual photon energy fluence model for monte carlo dose calculation. *Medical Physics*, 30(3):301–311, Mar. 2003. PMID: 12674229.

Geant4 Collaboration. Geant4 user's guide for application developers (version: geant4 9.5.0), Dec. 2011. URL `http://geant4.web.cern.ch/geant4/UserDocumentation/UsersGuides/ForApplicationDeveloper/BackupVersions/V9.5/fo/BookForAppliDev.pdf`.

D. Georg, T. Knöös, and B. McClean. Current status and future perspective of flattening filter free photon beams. *Medical Physics*, 38(3):1280–1293, Mar. 2011. PMID: 21520840.

O. Heid. Modulierbarer strahlenkollimator (German patent 102008055921.0), June 2010.

T. Holmes, T. Mackie, D. Simpkin, and P. Reckwerdt. A unified approach to the optimization of brachytherapy and external beam dosimetry. *International Journal of Radiation Oncology*Biology*Physics*, 20(4):859–873, Apr. 1991.

A. Holt, D. Van Gestel, M. P. Arends, E. W. Korevaar, D. Schuring, M. C. Kunze-Busch, R. J. Louwe, and C. van Vliet-Vroegindeweij. Multi-institutional comparison of volumetric modulated arc therapy vs. intensity-modulated radiation therapy for head-and-neck cancer: a planning study. *Radiation Oncology*, 8(1):26, 2013.

A. Hårdemark, H. Liander, H. Rehbinder, and J. Löf. Direct machine parameter optimization with RayMachine® in pinnacle3® white paper raysearch laboratories. 2003.

M. S. Huq, I. J. Das, T. Steinberg, and J. M. Galvin. A dosimetric comparison of various multileaf collimators. *Physics in Medicine and Biology*, 47:N159–N170, June 2002.

ICRU. International commission on radiation units and measurements. prescribing, recording and reporting photon beam therapy. ICRU report 50. *Bethesda: International Commission on Radiation Units and Measurements*, 1993.

ICRU. International commission on radiation units and measurements. prescribing, recording and reporting photon beam therapy (supplement to report 50). ICRU report 62. *Bethesda: International Commission on Radiation Units and Measurements*, 1999.

ICRU. International commission on radiation units and measurements. prescribing, recording, and reporting photon-beam intensity-modulated radiation therapy (IMRT). ICRU report 83. *Bethesda: International Commission on Radiation Units and Measurements*, 2010.

IEC. IEC 61217. radiotherapy equipment - coordinates, movements and scales. edition 1.2. *International Electrotechnical Commision*, 2008.

J. Izewska. Shaping of photon beams from electron linear accelerators in radiation therapy. *Medical Physics*, 20(1):171, 1993.

R. Jeraj, T. R. Mackie, J. Balog, G. Olivera, D. Pearson, J. Kapatoes, K. Ruchala, and P. Reckwerdt. Radiation characteristics of helical tomotherapy. *Medical Physics*, 31:396, 2004.

G. Kragl, S. af Wetterstedt, B. Knäusl, M. Lind, P. McCavana, T. Knöös, B. McClean, and D. Georg. Dosimetric characteristics of 6 and 10MV unflattened photon beams. *Radiotherapy and Oncology: Journal of the European Society for Therapeutic Radiology and Oncology*, 93 (1):141–146, Oct. 2009. PMID: 19592123.

S. Krause, S. Beck, K. Schubert, S. Lissner, S. Hui, K. Herfarth, J. Debus, and F. Sterzing. Accelerated large volume irradiation with dynamic Jaw/Dynamic couch helical tomotherapy. *Radiation Oncology*, 7(1):191, 2012.

P. Kupelian, T. Willoughby, A. Mahadevan, T. Djemil, G. Weinstein, S. Jani, C. Enke, T. Solberg, N. Flores, D. Liu, D. Beyer, and L. Levine. Multi-institutional clinical experience with the calypso system in localization and continuous, real-time monitoring of the prostate gland during external radiotherapy. *International Journal of Radiation Oncology*Biology*Physics*, 67(4):1088–1098, Mar. 2007.

K. M. Langen, W. Lu, W. Ngwa, T. R. Willoughby, B. Chauhan, S. L. Meeks, P. A. Kupelian, and G. Olivera. Correlation between dosimetric effect and intrafraction motion during prostate treatments delivered with helical tomotherapy. *Physics in Medicine and Biology*, 53 (24):7073–7086, Dec. 2008a.

K. M. Langen, T. R. Willoughby, S. L. Meeks, A. Santhanam, A. Cunningham, L. Levine, and P. A. Kupelian. Observations on real-time prostate gland motion using electromagnetic tracking. *International Journal of Radiation Oncology*Biology*Physics*, 71(4):1084–1090, July 2008b.

K. M. Langen, B. Chauhan, J. V. Siebers, J. Moore, and P. A. Kupelian. The dosimetric effect of intrafraction prostate motion on step-and-shoot intensity-modulated radiation therapy plans: Magnitude, correlation with motion parameters, and comparison with helical tomotherapy plans. *International Journal of Radiation Oncology*Biology*Physics*, 84(5):1220–1225, Dec. 2012.

W. R. Lee. Prostate cancer and the hypofractionation hypothesis. *Journal of Clinical Oncology*, Oct. 2013.

H. S. Li, I. J. Chetty, C. A. Enke, R. D. Foster, T. R. Willoughby, P. A. Kupellian, and T. D. Solberg. Dosimetric consequences of intrafraction prostate motion. *International Journal of Radiation Oncology*Biology*Physics*, 71(3):801–812, July 2008a.

H. S. Li, I. J. Chetty, and T. D. Solberg. Quantifying the interplay effect in prostate IMRT delivery using a convolution-based method. *Medical Physics*, 35(5):1703, 2008b.

Y. Li, J. Yao, and D. Yao. Genetic algorithm based deliverable segments optimization for static intensity-modulated radiotherapy. *Physics in Medicine and Biology*, 48(20):3353–3374, Oct. 2003.

Y. Lin, T. Liu, W. Yang, X. Yang, and M. K. Khan. The non-gaussian nature of prostate motion based on real-time intrafraction tracking. *International Journal of Radiation Oncology*Biology*Physics*, 87(2):363–369, Oct. 2013.

C.-M. Ma and J. Li. Dose specification for radiation therapy: dose to water or dose to medium? *Physics in Medicine and Biology*, 56(10):3073–3089, May 2011.

N. MacDougall, C. Dean, and R. Muirhead. Stereotactic body radiotherapy in prostate cancer: Is rapidarc a better solution than cyberknife? *Clinical Oncology*, 26(1):4–9, Jan. 2014.

T. R. Mackie, J. Balog, K. Ruchala, D. Shepard, S. Aldridge, E. Fitchard, P. Reckwerdt, G. Olivera, T. McNutt, and M. Mehta. Tomotherapy. *Seminars in Radiation Oncology*, 9(1): 108–117, Jan. 1999.

P. Mancosu, S. Castiglioni, G. Reggiori, M. Catalano, F. Alongi, C. Pellegrini, S. Arcangeli, A. Tozzi, F. Lobefalo, A. Fogliata, P. Navarria, L. Cozzi, and M. Scorsetti. Stereotactic body radiation therapy for liver tumours using flattening filter free beam: dosimetric and technical considerations. *Radiation Oncology*, 7(1):16, 2012.

P. Metcalfe, T. Kron, P. Hoban, and P. Metcalfe. *The physics of radiotherapy x-rays and electrons*. Medical Physics Pub., Madison, Wis., 2007. ISBN 9781930524354 1930524358 9781930524361 1930524366.

J. L. Morales and J. Nocedal. Remark on "algorithm 778: L-BFGS-B: fortran subroutines for large-scale bound constrained optimization". *ACM Transactions on Mathematical Software*, 38(1):1–4, Nov. 2011.

S. Nill. *Development and application of a multi-modality inverse treatment planning system*. PhD thesis, Ruprecht-Karls-Universität Heidelberg, Heidelberg, Germany, 2001.

S. M. Oliveira, N. J. Teixeira, and L. Fernandes. What do we know about the α/β for prostate cancer? *Medical Physics*, 39(6):3189, 2012.

K. Otto. Volumetric modulated arc therapy: IMRT in a single gantry arc. *Medical Physics*, 35: 310, 2008a.

K. Otto. Volumetric modulated arc therapy: IMRT in a single gantry arc. *Medical Physics*, 35: 310, 2008b.

D. Palma, E. Vollans, K. James, S. Nakano, V. Moiseenko, R. Shaffer, M. McKenzie, J. Morris, and K. Otto. Volumetric modulated arc therapy for delivery of prostate radiotherapy: Comparison with intensity-modulated radiotherapy and three-dimensional conformal radiotherapy. *International Journal of Radiation Oncology*Biology*Physics*, 72(4):996–1001, Nov. 2008.

J. A. Peñgarícano, N. Papanikolaou, Y. Yan, E. Youssef, and V. Ratanatharathorn. Feasibility of cranio-spinal axis radiation with the hi-art tomotherapy system. *Radiotherapy and Oncology*, 76(1):72–78, July 2005.

J. Perl, J. Shin, J. Schuümann, B. Faddegon, and H. Paganetti. TOPAS: an innovative proton monte carlo platform for research and clinical applications. *Medical Physics*, 39(11):6818, 2012.

A. Pirzkall, F. Lohr, A. Höss, M. Wannenmacher, J. Debus, and M. Carol. Comparison of intensity-modulated radiotherapy with conventional conformal radiotherapy for complex-shaped tumors. *International Journal of Radiation Oncology*Biology*Physics*, 48(5):1371–1380, Dec. 2000.

E. B. Podgorsak. *Radiation Physics for Medical Physicists*. Springer-Verlag Berlin Heidelberg, Berlin, Heidelberg, 2010. ISBN 9783642008740 3642008747 9783642008757 3642008755. URL `http://dx.doi.org/10.1007/978-3-642-00875-7`.

F. Pönisch, U. Titt, O. N. Vassiliev, S. F. Kry, and R. Mohan. Properties of unflattened photon beams shaped by a multileaf collimator. *Medical Physics*, 33(6):1738, 2006.

H. E. Romeijn, R. K. Ahuja, J. F. Dempsey, and A. Kumar. A column generation approach to radiation therapy treatment planning using aperture modulation. *SIAM Journal on Optimization*, 15(3):838–862, Jan. 2005.

RTOG. RTOG 0938 protocol: A randomized phase II trial of hypofractionated radiotherapy for favorable risk prostate cancer (version date 2013-07-24). *Radiation Therapy Oncology Group, Philadelphia*, 2013.

B. J. Salter, V. Sarkar, B. Wang, H. Shukla, M. Szegedi, and P. Rassiah-Szegedi. Rotational IMRT delivery using a digital linear accelerator in very high dose rate 'burst mode'. *Physics in Medicine and Biology*, 56(7):1931–1946, Apr. 2011.

D. Schmitt, S. Nill, K. Herfarth, M. Müter, J. Pfitzenmaier, A. Zabel-du Bois, F. Röer, P. Huber, and U. Oelfke. Intrafraction organ motion during prostate radiotherapy: Quantitative correlation of treatment time and margin size. *International Journal of Radiation Oncology*Biology*Physics*, 78(3):S752, Nov. 2010.

D. M. Shepard, M. A. Earl, X. A. Li, S. Naqvi, and C. Yu. Direct aperture optimization: A turnkey solution for step-and-shoot IMRT. *Medical Physics*, 29(6):1007, 2002.

J. Shin, J. Perl, J. Schümann, H. Paganetti, and B. A. Faddegon. A modular method to handle multiple time-dependent quantities in monte carlo simulations. *Physics in Medicine and Biology*, 57(11):3295–3308, June 2012.

K. H. Spruijt, M. Dahele, J. P. Cuijpers, M. Jeulink, D. Rietveld, B. J. Slotman, and W. F. Verbakel. Flattening filter free vs flattened beams for breast irradiation. *International Journal of Radiation Oncology*Biology*Physics*, 85(2):506–513, Feb. 2013.

F. Sterzing, K. Schubert, G. Sroka-Perez, J. Kalz, J. Debus, and K. Herfarth. Helical tomotherapy: Experiences of the first 150 patients in heidelberg. *Strahlentherapie und Onkologie*, 184 (1):8–14, Jan. 2008a.

F. Sterzing, G. Sroka-Perez, K. Schubert, M. W. Münter, C. Thieke, P. Huber, J. Debus, and K. K. Herfarth. Evaluating target coverage and normal tissue sparing in the adjuvant radiotherapy of malignant pleural mesothelioma: Helical tomotherapy compared with step-and-shoot IMRT. *Radiotherapy and Oncology*, 86(2):251–257, Feb. 2008b.

F. Sterzing, T. Welzel, G. Sroka-Perez, K. Schubert, J. Debus, and K. K. Herfarth. Reirradiation of multiple brain metastases with helical tomotherapy: A multifocal simultaneous integrated boost for eight or more lesions. *Strahlentherapie und Onkologie*, 185(2):89–93, Feb. 2009.

F. Sterzing, H. Hauswald, M. Uhl, H. Herm, A. Wiener, K. Herfarth, J. Debus, and R. Krempien. Spinal cord sparing reirradiation with helical tomotherapy. *Cancer*, 116(16):3961–3968, May 2010a.

F. Sterzing, M. Uhl, H. Hauswald, K. Schubert, G. Sroka-Perez, Y. Chen, W. Lu, R. Mackie, J. Debus, K. Herfarth, and G. Oliveira. Dynamic jaws and dynamic couch in helical tomotherapy. *International Journal of Radiation Oncology*Biology*Physics*, 76(4):1266–1273, Mar. 2010b.

M. B. Tacke, H. Szymanowski, U. Oelfke, C. Schulze, S. Nuss, E. Wehrwein, and S. Leidenberger. Assessment of a new multileaf collimator concept using GEANT4 monte carlo simulations. *Medical Physics*, 33(4):1125–1132, Apr. 2006. PMID: 16696490.

M. B. Tacke, S. Nill, P. Häring, and U. Oelfke. 6 MV dosimetric characterization of the 160 MLC, the new siemens multileaf collimator. *Medical Physics*, 35(5):1634–1642, May 2008. PMID: 18561638.

E. M. Thomas, R. A. Popple, B. M. Prendergast, G. M. Clark, M. C. Dobelbower, and J. B. Fiveash. Effects of flattening filter-free and volumetric-modulated arc therapy delivery on treatment efficiency. *Journal of applied clinical medical physics / American College of Medical Physics*, 14(6):4328, 2013. PMID: 24257275.

S. Ulrich, S. Nill, and U. Oelfke. Development of an optimization concept for arc-modulated cone beam therapy. *Physics in Medicine and Biology*, 52:4099–4119, July 2007a.

S. Ulrich, S. Nill, and U. Oelfke. Development of an optimization concept for arc-modulated cone beam therapy. *Physics in Medicine and Biology*, 52(14):4099–4119, July 2007b.

D. Van Gestel, C. van Vliet-Vroegindeweij, F. Van den Heuvel, W. Crijns, A. Coelmont, B. De Ost, A. Holt, E. Lamers, Y. Geussens, S. Nuyts, D. Van den Weyngaert, T. Van den Wyngaert, J. B. Vermorken, and V. Gregoire. RapidArc, SmartArc and TomoHD compared with classical step and shoot and sliding window intensity modulated radiotherapy in an oropharyngeal cancer treatment plan comparison. *Radiation Oncology*, 8(1):37, 2013.

O. N. Vassiliev, U. Titt, F. Pönisch, S. F. Kry, R. Mohan, and M. T. Gillin. Dosimetric properties of photon beams from a flattening filter free clinical accelerator. *Physics in Medicine and Biology*, 51(7):1907–1917, Apr. 2006.

C. Wang, S. Luan, G. Tang, D. Z. Chen, M. A. Earl, and C. X. Yu. Arc-modulated radiation therapy (AMRT): a single-arc form of intensity-modulated arc therapy. *Physics in Medicine and Biology*, 53(22):6291–6303, Nov. 2008.

S. Webb. *The physics of conformal radiotherapy: advances in technology.* Medical science series. Institute of Physics Pub, Bristol ; Philadelphia, 1997.

S. Webb. *Intensity-modulated radiation therapy.* Institute of Physics Pub., Bristol; Philadelphia, 2001.

S. Webb. The physical basis of IMRT and inverse planning. *British Journal of Radiology*, 76 (910):678–689, Oct. 2003.

S. Webb. *Contemporary IMRT: developing physics and clinical implementation.* Series in medical physics and biomedical engineering. Institute of Physics, Bristol ; Philadelphia, 2005.

J. S. Welsh, R. R. Patel, M. A. Ritter, P. M. Harari, T. R. Mackie, and M. P. Mehta. Helical tomotherapy: an innovative technology and approach to radiation therapy. *Technology in Cancer Research & Treatment*, 1(4):311–316, Aug. 2002. PMID: 12625791.

T. R. Willoughby, P. A. Kupelian, J. Pouliot, K. Shinohara, M. Aubin, M. Roach, L. L. Skrumeda, J. M. Balter, D. W. Litzenberg, S. W. Hadley, J. T. Wei, and H. M. Sandler. Target localization and real-time tracking using the calypso 4D localization system in patients with localized prostate cancer. *International Journal of Radiation Oncology*Biology*Physics*, 65(2):528–534, June 2006.

D. Wolff, F. Stieler, G. Welzel, F. Lorenz, Y. Abo-Madyan, S. Mai, C. Herskind, M. Polednik, V. Steil, F. Wenz, and F. Lohr. Volumetric modulated arc therapy (VMAT) vs. serial tomotherapy, step-and-shoot IMRT and 3D-conformal RT for treatment of prostate cancer. *Radiotherapy and Oncology*, 93(2):226–233, Nov. 2009.

J. Y. Wong, A. Liu, T. Schultheiss, L. Popplewell, A. Stein, J. Rosenthal, M. Essensten, S. Forman, and G. Somlo. Targeted total marrow irradiation using three-dimensional image-guided tomographic intensity-modulated radiation therapy: An alternative to standard total body irradiation. *Biology of Blood and Marrow Transplantation*, 12(3):306–315, Mar. 2006.

C. X. Yu. Intensity-modulated arc therapy with dynamic multileaf collimation: an alternative to tomotherapy. *Physics in Medicine and Biology*, 40(9):1435–1449, Sept. 1995.

C. X. Yu and G. Tang. Intensity-modulated arc therapy: principles, technologies and clinical implementation. *Physics in Medicine and Biology*, 56(5):R31–R54, Mar. 2011.

C. X. Yu, D. A. Jaffray, and J. W. Wong. The effects of intra-fraction organ motion on the delivery of dynamic intensity modulation. *Physics in Medicine and Biology*, 43(1):91–104, Jan. 1998.

C. Zhu, R. H. Byrd, P. Lu, and J. Nocedal. Algorithm 778: L-BFGS-B: fortran subroutines for large-scale bound-constrained optimization. *ACM Transactions on Mathematical Software*, 23(4):550–560, Dec. 1997.

Acknowledgements

I wish to express a very special thank you to the following people:

- Uwe Oelfke for being a great thesis advisor and a very humorous and cordial group leader
- Simeon Nill for a more than excellent day-to-day supervision
- All members of my research group *Physical Models* at the German Cancer Research Center for many fruitful advises and discussions, and above all for creating a friendly and warm-hearted working atmosphere
- Wolfgang Schlegel for accepting me into the department of *Medical Physics in Radiation Oncology* and for acting as a second thesis advisor
- Florian Sterzing from the Heidelberg University Hospital for a productive research collaboration
- Oliver Heid, Jürgen Heller and Michael Kleemann from Siemens Coorporate Research for their support and critical feedback
- Makoto Asai from the Geant4 collaboration for his advice concerning time-dependent MC simulations
- The PTSIM project collaboration for providing us with their Geant4 dicom reader